Universidad Autónoma de Querétaro

Facultad de Ingeniería

Maestría en Instrumentación y
Control Automático

IDENTIFICATION, STATE ESTIMATION, AND CONTROL OF A PHYSICAL BISTABLE DUFFING OSCILLATOR

TESIS

Que como parte de los requisitos para obtener el grado de
Maestro en Ciencias en Instrumentación y Control Automático

Presenta:

Ulises Mondragón Cárdenas

Dirigido por:

Dr. Suresh Thenozhi

Dr. Antonio Concha Sánchez

Centro Universitario
Querétaro, QRO
México.
September 2023

Identification, state estimation, and control of a physical bistable duffing oscillator

por

Ulises Monodragón Cárdenas

Universidad Autónoma de Querétaro

Facultad de Ingeniería

Maestría en Instrumentación y
Control Automático

IDENTIFICATION, STATE ESTIMATION, AND CONTROL OF A PHYSICAL BISTABLE DUFFING OSCILLATOR

TESIS

Que como parte de los requisitos para obtener el grado de
Maestro en Ciencias en Instrumentación y Control Automático

Presenta:

Ulises Mondragón Cárdenas

Dirigido por:

Dr. Suresh Thenozhi

Dr. Antonio Concha Sánchez

SINODALES

Dr. Suresh Thenozhi	Presidente	Firma
Dr. Antonio Concha Sánchez	Secretario	Firma
Dr. Juvenal Rodríguez Reséndiz	Vocal	Firma
Dr. Mariano Garduño Aparicio	Suplente	Firma
Dr. José Román García Martínez	Suplente	Firma

Dr. Manuel Toledano Ayala	Dra. Ma. Guadalupe Flavia Loarca Piña
Director de la Facultad	Director de Investigación y Postgrado

Centro Universitario
Querétaro, QRO
México.
September 2023

This thesis is dedicated to my parents. Esta tesis está dedicada a mis padres.

Acknowledgments

A mis padres Pedro y Patricia por su apoyo y amor incondicional, son la base de mi educación y valores, quienes me han apoyado y guiado en todas mis desiciones.

A mi familia por siempre recibirme con los brazos abiertos y deseando lo mejor para mi.

A Karina mi mejor amiga por su amistad incondicional y por siempre estar para mí.

A mis amigos que los valoro por su amistad y ayuda en todo momento y sistuación.

A los miembros del sinodo por sus conseos y enseñanzas, en especial al Dr. Suresh Thenozhi y al Dr. Antonio Concha Sánchez, cuya ayuda esto no hubiera sido posible.

Al profesorado y personal adminitrativo de la Universidad Autónoma de Querétaro.

A CONAHCYT y a la Universidad Autónoma de Querétaro por el apoyo otorgado para realizar estos estudios.

Abstract

This thesis studies the identification, state estimation, and control of a nonlinear mechanical system. The system used corresponds to a forced bistable Duffing oscillator. The work developed is composed of four main sections: first, the design, construction, and validation of an experimental prototype; second, the estimation of the model parameters through the use of an identification algorithm; third, through the use of an observer, the unknown states of the oscillator are estimated; and fourth, the control of the tracking of a desired trajectory obtained from a reference model.

The state-of-the-art design of other experimental devices served as the basis for the design of the prototype used in this project. In this case, it was decided to use an elastic aluminum beam, and to achieve the attraction effect, magnets were placed at its tip. To validate the prototype, experiments were carried out on the three characteristic behaviors—inter-well, intra-well, and chaotic of the bistable Duffing oscillator. The prototype was able to successfully maintain the aforementioned behaviors.

The identification process was performed using the discrete recursive least squares method (LSM) with forgetting factor. To obtain the parameterization, necessary to apply the LSM, three types of filters were applied, in continuous time, discrete time, and integrals. The results could be repeated in several experiments, and show a correct estimation of the system parameters. The validation of the obtained results was performed by testing the persistent excitation of the input signal during identification, and experimentation where simulations of the estimated parameters converged to the same type of behavior as the one presented by the prototype with the same excitation signal.

The state of the art design of other experimental devices served as the basis for the design of the prototype used in this project. In this case, it was decided to use an elastic aluminum beam, and to achieve the attraction effect, magnets were placed at its tip. To validate the prototype, experiments were carried out on the three characteristic behaviors—inter-well, intra-well, and chaotic of the bistable Duffing oscillator. The prototype was able to successfully maintain the aforementioned behaviors.

The controller was designed using the back-stepping strategy; the control law uses the states estimated by the observer. The performance of the controller in simulations is good; it achieves adequate tracking of the reference model. Due to the control signal, only adequate results were achieved experimentally in the behavior between wells. The details of the causes are presented in the chapter concerning the controller. Finally, there are the final conclusions of the thesis, as well as improvements and future work on the reported project.

Resumen

En esta tesis se estudia la identificación, estimación de estados y control de un sistema mecánico no lineal, el sistema utilizado corresponde a un oscilador Duffing biestale forzado. El trabajo desarrollado se compone de cuatro secciones principales, primero, el diseño, construcción y validación de un prototipo experimental, segundo, la estimación de los parámetros del modelo mediante el uso de un algoritmo de identificación, tercero, por medio del uso de un observador se estiman los estados no conocidos del oscilador, cuarto, el control del seguimiento de una trayectoria deseada obtenida de un modelo de referencia.

El estado del arte de otros aparatos experimentales sirvió como base para el diseño del prototipo utilizado en este proyecto. En este caso se optó por utilizar una viga elástica de aluminio, y para lograr el efecto de atracción se colocaron imanes en su punta. Para validar el prototipo se realizaron experimentos de los tres comportamientos característicos; entre pozos, intrapozo, y caótico; del oscilador Duffing biestable. Se logró que el prototipo mantuviera los comportamientos mencionados de forma exitosa.

El proceso de identificación se realizó utilizando el método de mínimos cuadrados (LSM) recursivo discreto con factor de olvido. Para obtener la parametrización, necesaria para aplicar el LSM, se aplicaron tres tipos de filtros, en tiempo continuo, tiempo discreto, e integrales. Los resultados se pudieron repetir en varios experimentos, y muestran una correcta estimación de los parámetros del sistema. La validación de los resultados obtenidos se realizó por medio comprobar la excitación persistente de la señal de entrada durante la identificación, y de experimentación donde simulaciones de los parámetros estimados convergieron al mismo tipo de comportamiento que el que presentaba el prototipo con la misma señal de excitación.

Se diseñó e implementó un Observador No lineal Integral Extendido de Estados (NIESO) para estimar la velocidad e incertidumbre del sistema. Se probó teóricamente su estabilidad y las simulaciones mostraron un desempeño adecuado para la experimentación. Los resultados del observador aplicado se compararon con otro observador extendido similar, el error cuadrático medio fue menor al usar el observador NIESO.

El controlador se diseñó mediante la estrategia de back-stepping, la ley de control utiliza los estados estimados por el observador. El desempeño del controlador en simulaciones es bueno, logra un adecuado seguimiento del modelo de referencia. Debido a la señal de control, se logró que experimentalmente, únicamente se consiguieran resultados adecuados en el comportamiento entre pozos, los detalles de las causas se presentan en el capítulo que concierne al controlador. Finalmente, se tienen las conclusiones finales de la tesis, así como de mejoras y trabajo futuro del proyecto reportado.

Contents

List of Figures

List of Tables

Nomenclature

Controller

$\ddot{x}_d$	Desired beam acceleration
$\dot{x}_d$	Desired beam speed
ν	Controller virtual control input
F_{dfi}	Drift-free integrator filter
F_{ii}	Ideal integrator filter
x_d	Desired beam position
z_1	Controller state variable, tracking error
z_2	Controller state variable

Duffing Oscillator

$\ddot{q}$	Acceleration of the elastic beam
$\dot{q}$	Velocity of the elastic beam
$\mathbf{q}^*$	Duffing Oscillator Balance Point Vector
ω_n	Natural frequency of elastic beam
b_b	Beam rectangular shape base
c	Viscous damping coefficient
E	Modulus of Young
h_b	Beam rectangular shape height
I_b	Second moment of inertia of the beam
k_l	Linear stiffness of the elastic beam
k_n	Nonlinear stiffness of elastic beam

l_b Length of the beam

m Effective mass of the elastic beam

m_b Total mass of the beam

m_m Mass of the magnets

m_{eq} Equivalent mass of the beam

P_l Punctual load due to mass of the beam

q Position of the elastic beam

$q(l_x)$ Static deflection

q_n^* Duffing Oscillator Balance Point

q_{max} Maximum deflection of the beam

T_{max} Maximum kinetic energy

$U(q)$ Potential energy of the Duffing Oscillator

Identification

δ_i Integral operator filter gain

$\mathcal{I}_n$ Integrator operator filter

$\rho_i(t)$ An arbitrary continuous function

F Filter

F_c Continuous time filter

F_{i_n} Integral time n-th filter

F_{z_n} Discrete time n-th filter

g_i Integral operator filter gain

r Length factor of the integral filter

T_s Sampling period

Logarithmic Decrement

δ Logarithmic decrement ratio

ω Natural frequency

ω_d Frequency of the under-damped oscillation

τ_d Period of the under-damped oscillation

ξ Damping ratio

X_n n-th measured amplitude

Least Square Method

ϕ_I Regressor vector

$\boldsymbol{\theta}$ Vector of parameters to be estimated

λ_{ff} LSM forgeting factor

$\mathbf{e}_I$ LSM prediction error

L

P LSM gain matrix

$\nabla J(\widehat{\boldsymbol{\theta}})$ LSM cost function gradient

$\widehat{\boldsymbol{\theta}}$ Vector of estimated parameters

$J(\widehat{\boldsymbol{\theta}})$ LSM cost function

N Number of samples

$z(t)$ Output signal of parametrization

Observer

$\boldsymbol{\Delta}$ Uncertainty matrix

$\boldsymbol{\Psi}$ States estimation error matrix

χ Unmodeled dynamics

ϵ_o Error dynamics constant

Λ Extended State Observer Error Convergence Radius

λ_{e_j} Eigenvalue of matrix **A**

A Observer coefficient matrix

e Observer error dynamics

μ Observer error dynamics constant

ω_0 Observer gain

ω_o Observer gain

$\psi(\mathbf{x})$ Matrix of the states of the system

ρ_o Error dynamics constant

$\widehat{x}_0$ Estimated of the integrated state of x_1

$\widehat{x}_1$ Estimated position of the elastic beam

$\widehat{x}_2$ Estimated speed of the elastic beam

$\widehat{x}_3$ Estimated system uncertainty

d Measurements disturbance

e_n Observer n-th state error

F_{der} Derivative filter

g System uncertainty

$h_{1,2}$ Gronwall-Bellman Inequality continuous function

L Lipschitz constant

$p_o(t)$ Gronwall-Bellman Inequality continuous function

x_0 Integrated state of x_1

x_1 Position of the elastic beam

x_2 Velocity of the elastic beam

x_3 Uncertainty of the system

x_n^* Duffing Oscillator states space equilibrium point

Physics constants

t Time

Shake Table

$\ddot{p}$ Acceleration of the shake table

$\dot{p}$ Velocity of the shake table

θ_m Denotes Lead-screw angle of the shake table motor

b_{sd} Set-point velocity weight

i_m Applied motor current

k_d PD controller derivative gain

k_f Shake table model gain

k_m Back-emf parameter of the shake table motor

k_p PD Controller Proportional Gain

k_t	Current-torque of the motor
m_t	Total mass moved by the motor
p	Position of the shake table
p_b	Pitch of the lead-screw
r_m	Resistance parameter of the shake table motor
u_{PD}	Shake table proportional-derivative control signal
v_m	Shake table motor applied voltage
x_s	Shake table position
x_{sd}	Desired shake table position

CHAPTER 1

Introduction

Chaos theory is the concept that a slight change in the beginning can result in an enormous change in the future [1–3]. The study of chaotic systems is of great interest since they represent a very attractive topic due to the great variety of systems with this behavior. The chaos phenomenon occurs in important dynamic systems or processes, mainly in nonlinear systems, such as the Van Der Pool oscillator, the Predator-Prey system, and the Duffing oscillator, among others [4–6]. The study of nonlinear mechanical systems has gained great importance in recent decades, and many methods have been proposed to extract and analyze their characteristics, performance, solutions, and applications [7–9].

The Duffing oscillator is a system with a cubic nonlinearity that can have chaotic behavior [10]. Just to mention some areas of research related to this system, multiple works and investigations have been carried out to study it, search for solutions to the Duffing equation, and apply and validate methods for identifying nonlinear systems [11, 12]. Authors have focused on their use for the detection of electrical or mechanical signals [13], on characterizing mechanisms such as a Duffing oscillator, and studies have been carried out on chaos control and the synchronization of oscillators [14]. Also, there are works on its application in energy harvesting and in its use as a reference for the chaosification of systems. Its chaotic behavior can be used in engineering solutions to improve different sensors, such as metal detectors, optical fields, or magnetic fields. For example, in [15], they investigate the application of a Duffing oscillator to build inductive sensors. Other authors have focused on mathematical analysis related to the Duffing equation; for example, Feng et al. [16] used the qualitative theory of flat systems to analyze it, and Zivieri et al. [17] presented analytical and numerical solutions to the Duffing equation. It is known that the behavior of a Duffing oscillator is continuous and has multiple equilibrium points, some of which are unstable. In [11,12,18], they presented some of the equilibrium and stability point configurations of a Duffing oscillator.

The prototype design presented in this thesis is based on the experimental apparatus used by Moon and Holmes [8] and is shown in Figure 1.1. The prototype was mounted on a vibrating table to apply the input force to the system. A laser sensor was used to measure the position of the elastic beam. The system was analyzed through simulations, and the natural frequency of the structure was obtained.

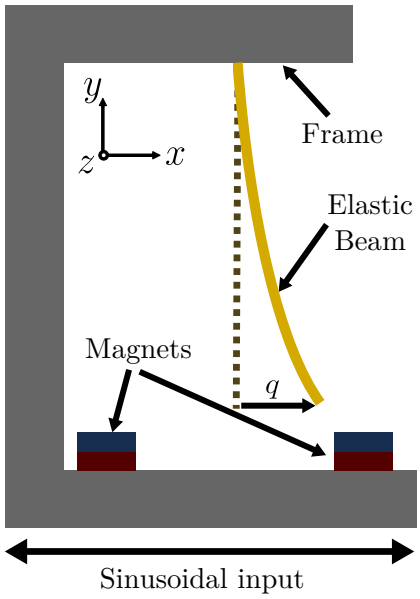

Figure 1.1: Experimental system proposed by Moon and Holmes, where the direction of gravity is in the direction of negative z.

1.1 Motivation

From the previous section, it is clear that many physical phenomena involving nonlinear oscillations are modeled using the Duffing oscillator. There are many works dedicated to the study of the behavior of these systems or their control.

In terms of control, most of the works consider only the simulation. The motivation of the work is to address the aforementioned problems, through:

- Useful prototype for experimentation and investigation of multiple stability configurations of the Duffing oscillator, for research and experimentation of chaotic nonlinear systems, and for future research in the area of energy harvesting.
- One of the objectives of the development of energy harvesting systems is to replace other power sources of autonomous technologies, mainly batteries.
- The possibility of replacing batteries with this type of system proposes a less polluting device power model compared to batteries.
- The prototype will be useful in didactic use for the study of nonlinear systems.

1.2 Problem Formulation

The main problem to solve can be divided into three sections. First, the development of a functional prototype of a bistable Duffing oscillator; second, the estimation of the parameters and the states of the system; and third, the close-loop control of the Duffing oscillator.

1.2.1 Experimental prototype

To understand the real behavior of Duffing systems, it is important to carry out simulation and experimental studies. Numerical simulation can be easily done by implementing the mathematical model (4.1) in software such as MATLAB®. On the other hand, one challenge is to build an experimental prototype that behaves like the Duffing-Holmes system. The design includes the properties of the beam and its instrumentation. A working prototype will also be built to allow experimentation with a wide variety of beams, frequencies, and excitation forces.

1.2.2 Parameters and state estimation

A laser sensor makes it possible to determine the beam's position, but since its speed cannot be determined, a controller must be installed in the system. State estimators, including sliding mode, high-gain, and extended state observers, to mention a few, can be utilized for this. A controller's performance will be enhanced by using the Non-linear Integral Extended State Observer (NIESO) technique to estimate system states and uncertainty.

Conversely, the Duffing-Holmes oscillator's parameters are a mystery. These parameters can be identified with minimum effort and are helpful in enhancing control performance.

1.2.3 Control of the system

Research on the control of chaotic systems is of interest. The behavior of these systems has been demonstrated in numerous articles, most of which report on work with bistable oscillators that are characterized by the Duffing equation. Still, the majority of these works have been simulation-based. Moreover, the majority of the works make the assumption that the system's states and parameters are known.

The main objective is to ensure that the oscillator follows a smooth path. This desired trajectory is generated from a reference model that is described below. It is also important to remember that the reference model will be constructed using the data from the parameter estimates, and that the controller will make use of the estimates that NIESO has provided.

To achieve the desired performance, the system will be simulated using the finite element approach in order to determine the structure's natural frequency. Frequencies that are near to those that will be employed in the experiments will be avoided.

By using a nonlinear integral extended state observer (NIESO) to accurately estimate the system states, a controller built using the *backstepping* method is able to track the reference trajectory for periodic behavior. The thin aluminum bar used in the experiment is fastened within a stiff frame and has magnets embedded in its tip. It holds up two magnets, whose attractive forces cancel out the elastic forces that would keep the beam straight. When there are no outside forces acting on the beam, the tip of the beam rests near one or the other of the magnets. Additionally, there exists a position of unstable center equilibrium where the magnetic forces cancel out.

The development of this platform implies not only its usefulness for investigations and experimentation of control and estimation tools for nonlinear systems with chaotic behavior, but it will also promote a useful prototype for teaching. The proposed design seeks to provide a flexible prototype to expand the range of study beams and frequencies, as well as modifications to study some of the applications of a bistable Duffing oscillator, such as energy harvesting, fault detection and prevention in mechanical systems, and electrical and telecommunications.

1.3 Objectives

Design, simulate, validate and build a prototype of a bistable Duffing oscillator system for its application in experimentation on chaos theory and nonlinear oscillations.

1.3.1 Specific Objectives

The specific objectives of this project are as follows:

- Modeling and simulation of the bistable Duffing oscillator.
- Design and construction of the prototype.
- Identification of the mechanical parameters of the system.
- Design of the NIESO (simulation and experimental validation).
- Proportional Derivative Control (simulation and experimental validation).

1.4 Thesis Structure

The thesis is organized as follows:

- Chapter 1 presents the state of the art of the topics to be dealt with in this text, the reason for studying them, as well as the description of the problem to be solved. Based on the problem, the objectives that must be achieved to generate a possible solution to the aforementioned problem are presented.
- Chapter 2 presents the information collected from the research carried out, including, but not limited to, key concepts, a description of the system and its mathematical model, comparative tables, and a summary of the state of the art. Applications that are being investigated at the time of writing this text.
- In Chapter 3 there is a description of the method that was used for the development of the project and the solution of the problem presented.
- Chapter 4 presents the mathematical model of the system developed, for which the equilibrium points and the dynamics of the oscillator were obtained so that it was possible to generate simulations of the system, which were subsequently carried out for their physical application and the compilation of the data obtained.
- Chapter 5 describes the process and the results of the identification, obtaining the parameters of the prototype of the system in such a way that it was possible to estimate the model of the system.
- Chapter 6 presents the development and work carried out for the design of the state estimator and the control law for the generation of the experimental results.
- Chapter 7 presents the general conclusions of the project, as well as the difficulties that arose during the development of the project and the result of the method used to solve the problem presented.

CHAPTER 2

Methodology

The suggested approach and the ethical issues surrounding the project's development are covered in the section that follows. The overall work approach is shown in Figure 2.1. The subsequent sections provide a more detailed description of this methodology, highlighting the key components of the diagram, procedures, and tasks.

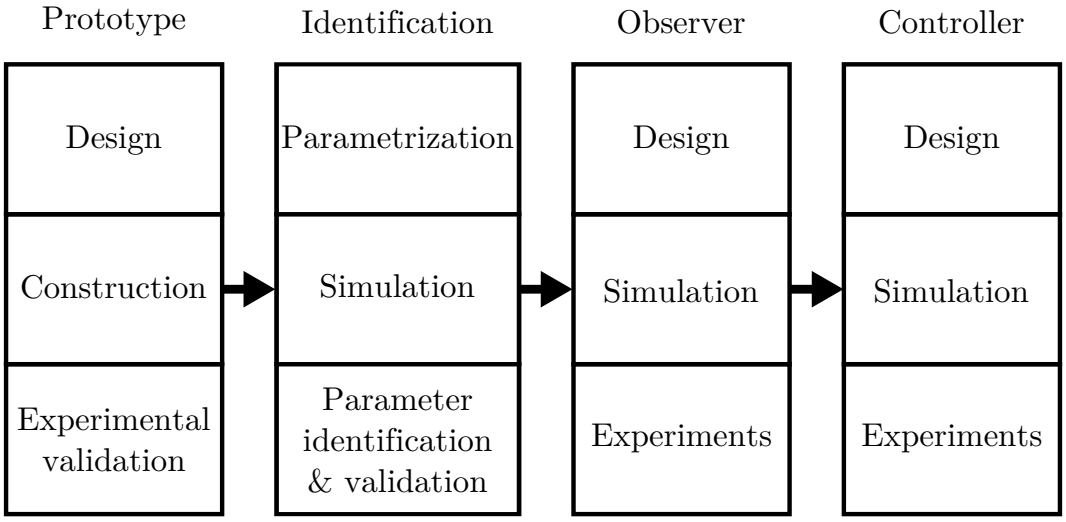

Figure 2.1: Proposed methodology.

2.1 System modeling and simulation

In order to evaluate the model presented in (2.1), it was necessary to find the equilibrium points, after that, the model will be simulated in the MATLAB® software environment to study the dynamics of the system.

$$m\ddot{q}(t) + c\dot{q}(t) - k_l q(t) + k_n q^3(t) = -m\ddot{p}(t) \tag{2.1}$$

where m is the effective mass of the beam, c is the viscous damping coefficient, k_l and k_n are the linear and non-linear stiffness coefficients respectively, $q(t)$, $\dot{q}(t)$ and $\ddot{q}(t)$ are the beam position,

velocity and acceleration, and $\ddot{v}(t)$ is the input acceleration for the system excitation.

2.2 Design and construction of the prototype

The design of a rigid frame was made, where the magnets that will be used will be mounted. It will also be necessary to carry out a frame frequency study to confirm that the natural frequency of the structure is not close to the one that will be used for excitation of the system. The beam will be designed based on the calculation of the natural frequency ω_n.

Prior to the construction of the prototype, its design was carried out in the CAD software SolidWorks®. In addition to the main elements that are part of a bistable Duffing oscillator, it was decided to allow the final prototype to be reconfigurable, that is, mobile, so that it can be used to carry out tests with different sizes of beams. It will also be necessary to be able to move the magnets of the frame to modify the equilibrium points of the system. The prototype design was made based on the horizontal configuration with magnets in the structure. To avoid the effects of gravity, the prototype was oriented in such a way that the movement of the beam is normal to the direction of the force of gravity, as shown in Figure 2.2.

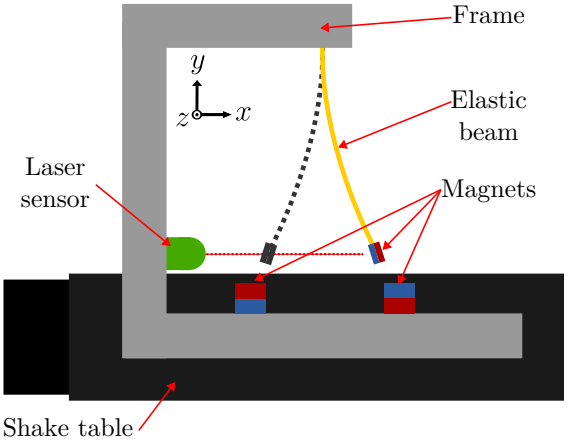

Figure 2.2: Block diagram of the proposed identification method, where the direction of gravity is in the direction of negative z.

2.3 System parameterization

To control the system, it is necessary to know the values of the damping coefficient (c), the linear stiffness (k_l), and the non-linear stiffness (k_n); for this, different strategies and parameter estimation algorithms were used. First, these values were obtained analytically, making use of the formulas and theory presented by Sanguiresu *et al.* [19] and by Kanamaru [20] that are described in Chapter 4.

Other identification techniques were employed in order to compare and contrast the obtained results in order to obtain a better approximation of the developed prototype model, as (2.1) is only an approximate model of the system. Using the online implementation of the offline Least Squares Method (LSM), a direct technique was used to carry out the identification.

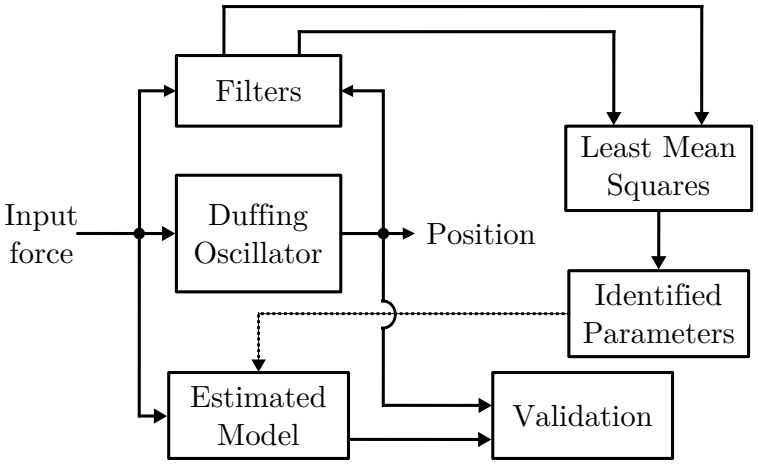

Figure 2.3: Block diagram of the proposed identification method.

Since there were only access to the longitudinal position of the beam tip and the angular position of the vibrating table motor, it was necessary to apply a filter to the output and input of the system in order to apply the LSM. In Chapter 4, the process of filtering the output and input signals of the oscillator is described. Three types of filters were used so that the values obtained could be compared and verified, as well as the performance of the LSM. First, it was decided to apply filters in continuous time to the frequency. Discrete-time filters, which use the same filter in continuous time in discrete time, were employed since the signal is discrete.Finally, the Integral-Based Filtering Method (IBFM) was used for identification. Figure 2.3 shows the proposed identification method, which is based on two main stages: the filtering of the measured signals and the least mean squares method. When obtaining the estimated values of the parameters, a validation of the results was carried out by comparing simulations of the system with the estimated values and the real system, using the same excitation force and similar initial conditions.

2.4 Design and simulation of the Observer

Since the measurements made could only determine the beam's position, it was suggested to utilize an extended-state linear observer to determine the beam's speed from its position. The observer algorithm was simulated and then applied to the real system to confirm that it was operating as intended.

2.5 Observer-based Controller Design

After having obtained the values of the aforementioned parameters, as well as the position and speed, we proceeded to develop a controller that allows the reaching of a desired position trajectory. This project suggested using a controller that was designed using the back-stepping technique.

2.6 Observer experimentation

After carrying out the identification of the system, verifying the performance of the designed NIESO observer, and selecting its gain, experiments of the system using the observer were carried out, and the results validated the correct design of the observer. In addition to this, further experiments with the system were performed using different extended-state observers, including a non-linear (NESO) observer.

2.7 Controller experimentation

Once the observer estimated the states of the system with sufficient accuracy, the controller could be applied, making tests so that the system achieves the desired behavior. First, tests were run to see if the desired behavior can be obtained from a starting state. Tests were then run to adjust the behavior when an alternative has been implemented.

2.8 Experimental validation

In order to evaluate the correct performance of the state observer and the controller, experimental tests were done with different initial conditions for the position of the beam; the objective was to get the system to achieve the type of behavior selected, whether it was interwell, intrawell, or chaotic, that is, the components shown in Figure 3.6. Since the Matlab tool Simulink® allows modifying values during the execution of the models, it was possible to make the desired behavior change.

CHAPTER 3

Prototype design and building

In this chapter, it is described the procedure for the design and building of the prototype used for the experimentation and the results obtained from this project. First, the design of the experimental prototype in computer-aided design (CAD) is described. Second, the construction process, the materials used for it, and the amplifier circuit construction are detailed. Technical drawings of the designed parts are included in the appendices.

3.1 Main references in the literature

The classical Duffing oscillator design consists of a ferromagnetic beam, cantilevered with two symmetrically spaced magnets serving as attractors, and sometimes carrying a mass at the tip of the beam [18]. The majority of earlier research has examined and studied this kind of oscillator in relation to energy harvesting [21]. A comparison table of the various oscillators that various authors have investigated can be seen below. Many studies have investigated how the use of nonlinearities extends the frequency spectrum to extend the bandwidth, activate nonlinear resonances, and facilitate tuning, despite the fact that research over the past ten years has concentrated on its operation in a linear regime [21].

Various oscillator designs have been used by different writers to describe their findings; Erturk and Inman [22] report the beam's range of motion using a prototype that is based on the Moon and Holmes design. While other authors have presented a horizontal configuration in which a permanent magnet is located at the free end of the beam and in front of it is a second magnet seeking to obtain bistable behavior, [21, 27] Studies carried out on harmonically excited systems show that a large amplitude response is robust to [21] parameter variations.

Below is a table that includes the configurations that different authors have reported:

Table 3.2: Oscillator Configuration Comparison.

	Magnet at the tip	**Magnets in the structure**
Horizontal	[21] [34] [35] [36] [37] [38] [23] [39]	[35] [36]
Vertical	Not reported in considered references.	[8] [18] [22]

Table 3.1: Parameters used for bistable oscillators.

	Beam size (cm)	Excitation frequency (Hz)	Excitation acceleration (g)
Kumar *et al.* [18]	$9.61 \times .95$	$4 - 13$	N/R
B. P. Mann [21]	N/R	$3 - 8$	0.6
Erturk e Inman [22]	$14.5\times$ N/R	10	0.36
Moon y Holmes [8]	18.8×0.95	$2 - 10$	N/R
Ibrahim *et al.* [23]	7.2×1	$15 - 17$	0.5
Wu *et al.* [24]	14×1.27	19.5	N/R
Alevras *et al.* [25]	$14.15\times$ N/R	$14 - 16$	N/R
Diankun Pan [26]	10×4	22	2
Arrieta *et al.* [27]	20×20	8.6	3
Betts *et al.* [28]	19×19	18	2
Arrieta *et al.* [29]	18×9.5	20.5	2.3
Betts *et al.* [30]	20×20	54	0.25
Li *et al.* [31]	15×5	59	10
Harris *et al.* [32]	25×6	8.4	31
Diankun *et al.* [33]	10×4	$36 - 38$	6

g: acceleration of gravity on Earth (9.81 m/s^2 approximately).
N/R: Not reported.

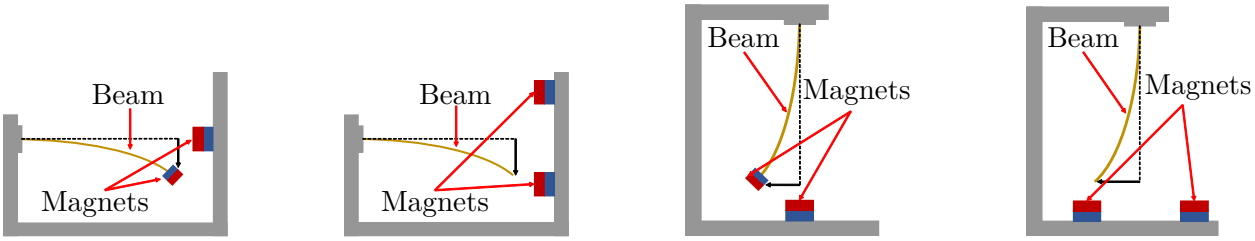

Figure 3.1: Different configurations of the oscillators. a) Horizontal configuration with a magnet at the tip. b) Horizontal configuration with magnets in the structure. c) Vertical configuration with a magnet at the tip. d) Vertical configuration with magnets in the structure.

When a configuration with magnets is presented in the structure, two permanent magnets are placed, as shown in Figures 3.1b and 3.1d, and the beam material used can be ferromagnetic, while When the beam material does not have this characteristic, it is common to use a permanent magnet at the tip and a second magnet in the structure installed symmetrically in relation to the beam, as shown in Figures 3.1a and 3.1c.

3.2 Dynamics of a Duffing-Holmes system

Consider a bistable The Duffing oscillator is excited using an external vibration force, as shown in Figure 2.2, which is constructed by attaching one end of a ferromagnetic elastic beam to the rigid base. When this base is subjected to external vibration, the free end of the elastic beam oscillates

due to the magnetic field generated by two permanent magnets. As mentioned in Chapter 2, this system can be represented by the expression (2.1) and has three equilibrium points, which can be obtained when the excitation force of the system is zero; therefore, you have to:

$$m\ddot{q}(t) + c\dot{q}(t) - k_l q(t) + k_n q^3(t) = 0 \tag{3.1}$$

for the previous expression the equilibrium points are found as:

$$q(-k_l + k_n x^2) = 0 \tag{3.2}$$
$$-k_l + k_n x^2 = 0 \tag{3.3}$$

from the previous expressions we have:

$$q_1^* = 0 \tag{3.4}$$
$$q_{2,3}^* = \pm\sqrt{\frac{k_l}{k_n}} \tag{3.5}$$

On the other hand, the three equilibrium points of $\dot{q}$ are at 0. Therefore, the three equilibrium points can be described in vector form of the form $\mathbf{q}^* = [q^*, \dot{q}^*]^{\mathrm{T}}$, that is:

$$\mathbf{q}_1^* = [0, 0]^{\mathrm{T}} \tag{3.6}$$
$$\mathbf{q}_{2,3}^* = \left[\pm\sqrt{\frac{k_l}{k_n}}, 0\right]^{\mathrm{T}} \tag{3.7}$$

The potential energy $U(x)$ of the system (4.1) can be found using its nonlinear rigidity force as follows:

$$U(q) = \int_0^q (k_n q^3 - k_l q)dq = \frac{1}{4}k_n q^4 - \frac{1}{2}k_l q^2 \tag{3.8}$$

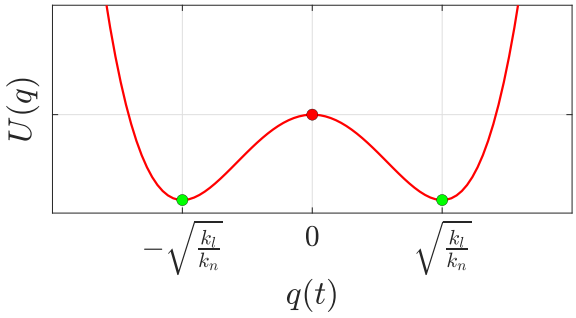

Figure 3.2: Double potential well energy with three equilibrium points.

The behavior of $U(q)$ is shown in Figure 3.2, where the existence of the three equilibrium points can be seen, of which the point equilibrium at $\mathbf{q}_1^* = [0, 0]^{\mathrm{T}}$ is unstable, while the remaining two equilibrium points are stable; Due to this, this system is called a bistable oscillator. The existence of two wells in the potential energy around the equilibrium points $\mathbf{q}_2^*$ and $\mathbf{q}_3^*$ is also observed.

Due to the existence of the two potential energy wells of the stable equilibrium points it is possible to have three different behaviors of the oscillator. When the position of the beam shows movements jumping from one potential well to the other, it is known as an interwell behavior, while when the value of the measured position rotates around one of the stable points it is known as intrawell. The third type of behavior is known as chaotic [40].

The behavior of the system depends on the value of the parameters α, β and γ, as well as the initial conditions $\mathbf{x}(0) = [x(0), \dot{x}(0)]^{\mathrm{T}}$ and the magnitude and frequency of the excitation force. Figure 3.3(a) shows the phase graph of the interwell behavior; It can be seen that the response of the system moves between stable equilibrium points, jumping from one potential well to the other. Figure 3.3(b) corresponds to the displacement amplitude. In this behavior the greatest amplitude can be obtained over time.

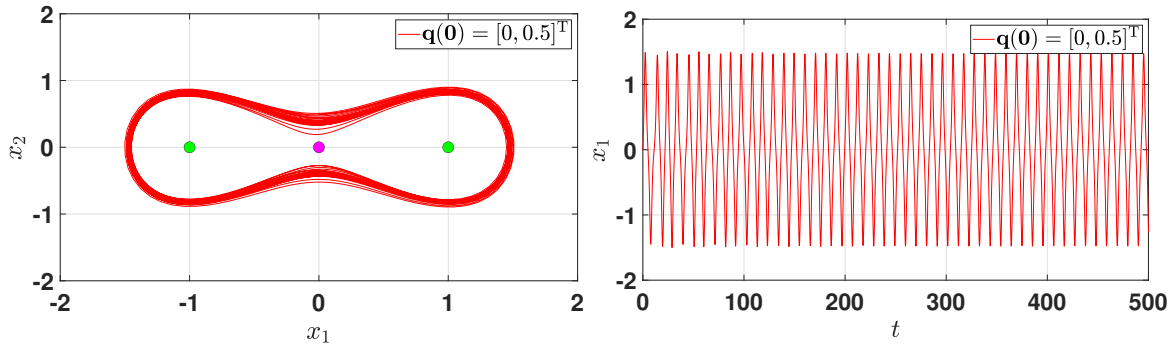

(a) (b)

Figure 3.3: Interwell dynamics. (a) Phase diagram. (b) Position in time.

In the intrawell behavior shown in Figure 3.4(a), the response of the system falls within one of the potential energy wells. Depending on the initial conditions, the obtained behavior can be described by the response in blue or red. The displacement amplitude is small compared to the previous behavior; This is because the position surrounds only one of the balance points, as seen in Figure 3.4(b).

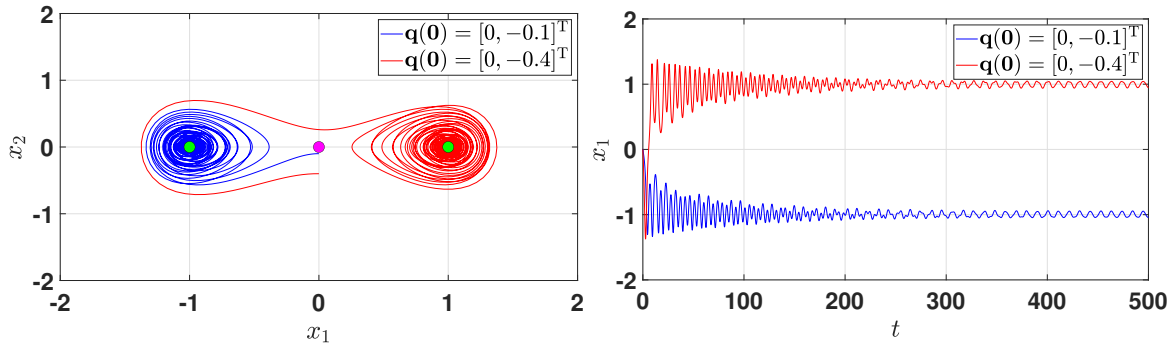

(a) (b)

Figure 3.4: Intrawell dynamics. (a) Phase diagram. (b) Position in time.

The third and final type of behavior is chaotic, so it presents a response similar to a combination of the previous two. Its repeatability is difficult and complicated to deduce. Despite what can be

seen in Figure 3.5(b), the amplitude of the displacement varies on multiple occasions over time, to show in a correct way chaos of a system it is commonly used a Poincare map, Figure 3.5(c) shows the map of a simulation of the Duffing oscillator.

A characteristic of chaotic systems is that they depend significantly on the initial conditions. An insignificant change in the starting conditions is amplified and propagates exponentially throughout the system [41]. This means that the trajectories of the variables (states) of the system, with certain initial conditions, are very different from the trajectories corresponding to a small change in said initial conditions [4].

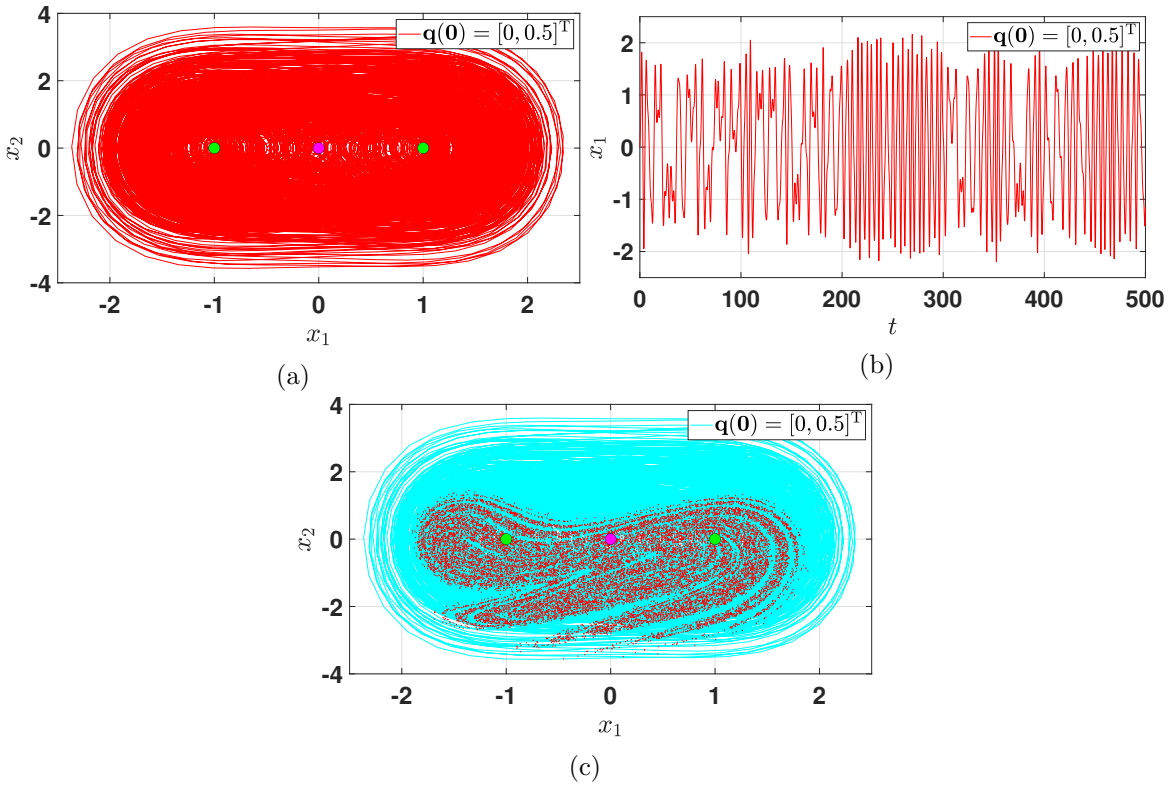

Figure 3.5: Chaotic dynamics. (a) Phase diagram. (b) Position in time. (c) Poincare map.

3.3 Prototype design

The basic materials proposed for the construction of the prototype are listed below, as shown in the enumeration of Figure 3.6:

1. Square structural aluminum profile 30×30 mm.
2. 166×390 mm thick acrylic plate.
3. 120×80 mm thick aluminum plate.
4. M6 screws 60 mm cylindrical head.

5. Base for the support of the flexible beam 1×2 inches.
6. Two neodymium magnets with a diameter of 12 mm and a caliber of 5 mm.
7. Panasonic® HG-C1400-P laser sensor.
8. QUANSER I-40 vibrating table and QUANSER VoltPAQ-X1 amplifier.
9. QUANSER Q2-USB signal acquisition card.
10. Computer with MATLAB® and QUARC software.

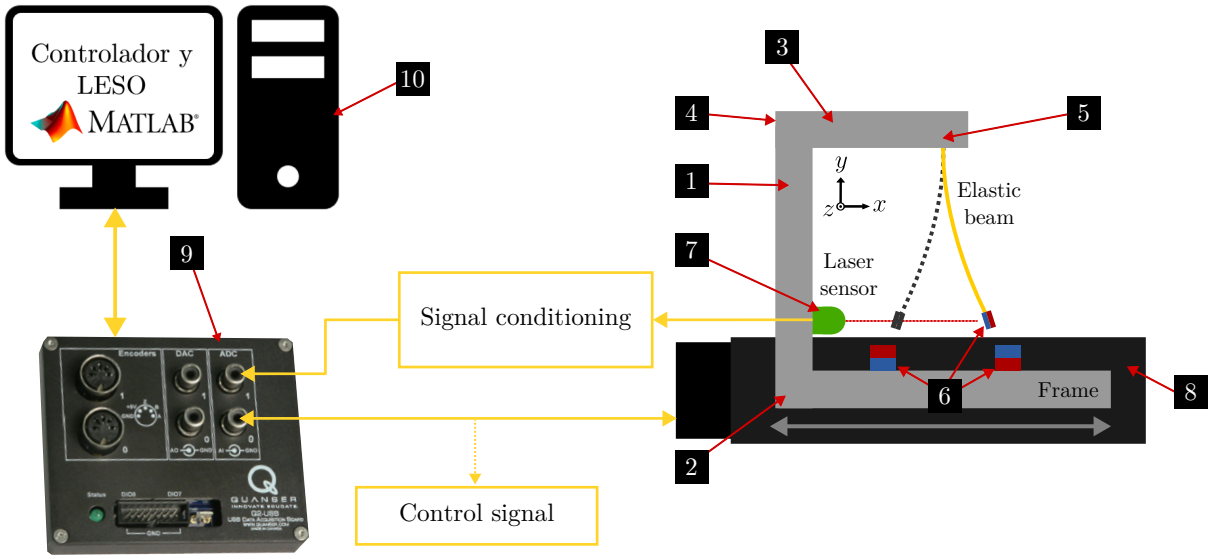

Figure 3.6: Diagram of the proposed system, Where the direction of gravity is in the direction of negative z.

It was determined, based on earlier prototypes that were put out, to position the device so that the direction of gravity's effect was transverse to the beam's displacement, allowing for the system's identification to ignore it. For a bistable system represented by (2.1), the Duffing equation may therefore be used to simulate the suggested experimental system depicted in Figure 3.8.

The material considered for the design was six-millimeter-thick acrylic because it is light and sufficiently resistant. The main base on which the system's frame was mounted and which will be attached to the I-40 vibrating table is a sheet of acrylic. To complete the frame, a thirty-millimeter square aluminum structural profile was used, along with a machined aluminum piece to assemble the section that will hold the elastic beam as well as to modify the dimensions of the frame. The lower frame of the prototype consists of three layers of acrylic, in such a way that a rail is created through which the magnet bases can be moved; these bases are also made of acrylic, so that the distance of the magnets on the rail can be modified. In this way, it can be adapted to different sizes of beams.

The laser sensor was installed on a twenty-millimeter square aluminum structural profile in a second structure. This base can be adjusted to shift the sensor closer or farther away from the primary structure. The primary base also housed this second building.

Figure 3.7: Experimental developed prototype.

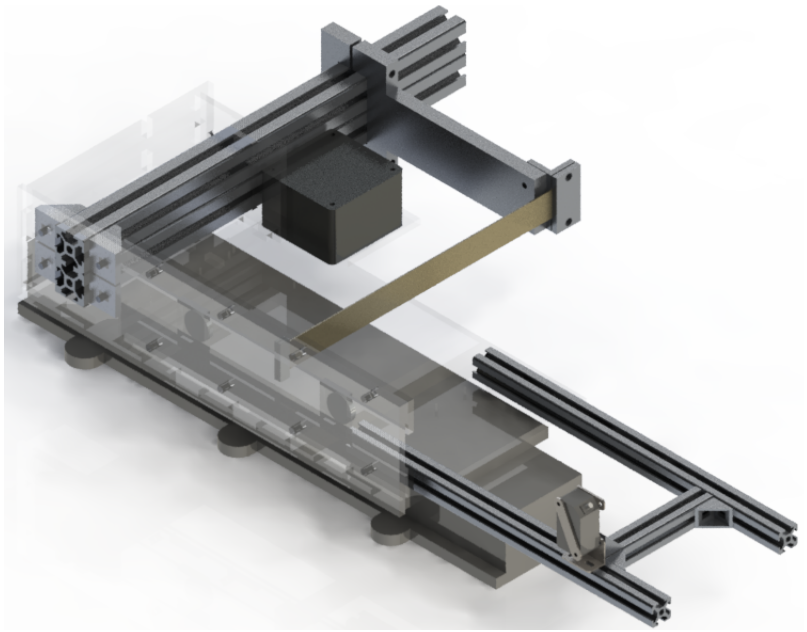

Figure 3.8: Final prototype design, in Appendix A you can find the CAD designs of the parts used to build the prototype.

3.3.1 Shake Table I-40

To generate the force that excites the system, a vibrating table was used on which the system was mounted. This equipment was used to carry out the experimentation of the identification processes and the implementation of the observer and the controller. The Shake Table I-40 is a single-axis motion simulator from Quanser with multiple advantages, including its low-maintenance and open-architecture structure, easy operation with stand-alone Quarq software, and a plug-in for Matlab® Simulink®. It is focused on the simulation of seismic activity for topics related to civil and geotechnical engineering. However, in this case, it has been used successfully for control issues and its application in non-linear oscillators [42]. To use this equipment, it is necessary to have other Quanser brand components, which are the VoltPAQ-X1 voltage amplifier and a data acquisition card. To generate movement, a signal of maximum ±2 [cm] and 10 [Hz] must be introduced. Table 3.3 summarizes some equipment specifications that must be taken into account for its operation.

Table 3.3: Shake table I-40 specifications.

Shake Table I-40 specifications [42]	
Parameter	Description / Value
Dimensions (L×W×H)	57.5 [cm] × 12.7 [cm] × 7.62 [cm]
Maximun travel (end to end)	40 [mm]
Maximun paload at 1.0 g	1.5 [kg]
Maximun acceleration with 1.5 kg payload	1.0 [g]
Operational bandwidth	10 [Hz]
Effective stage position resolution	1.22 [μm]
Maximum continuous current	3.0 [A]
Linear Guide	Misumi LX3010C-B1-T3056.4-150
DC Motor	Magmotor S23 Brushed Servo Motor

3.3.2 Shake Table PD Controller

The Shake Table I-40 model is given by the following transfer function

$$X_s(s) = \frac{1}{k_f s^2} I_m(s), \quad k_f = \frac{m_t p_b}{k_t} \tag{3.9}$$

where $X_s(s)$ is the Laplace of the stage position, I_m is the Laplace of the applied motor current, k_f is the model gain, m_t is the total mass being moved by the motor, p_b is the pitch of the lead-screw, and k_t is the current-torque of the motor [42]. The current applied to the motor is

$$I_m = \frac{V_m(s) - k_m s \Theta_m(s)}{r_m} \tag{3.10}$$

where V_m is Laplace of the applied voltage, k_m and r_m are the back-emf parameter and the resistance of the motor respectively, and, $\Theta_m(s)$ denotes the lead-screw angle.

The Laplace of the proportional-derivative feed-forward control $U_{PD}(s)$ used to regulate the shake table position has the following structure

$$U_{PD}(s) = V_m(s) = k_p(X_{sd}(s) - X_s(s)) + k_d s(b_{sd} X_{sd}(s) - X_s(s)) \tag{3.11}$$

where $k_p = 4874$ [V/m] and $k_d = 4.387$ [V-s/m] are the proportional and derivative control gains respectively. Substituting (3.9) into (3.11) and solving for $X_s(s)/X_{sd}(s)$ gives the closed loop transfer function [42]

$$\frac{X_s(s)}{X_{sd}(s)} = \frac{k_p + b_{sd}k_d s}{K_f P_b r_m \left(s^2 + \frac{2K_m\pi + P_b k_d}{K_f} s + \frac{k_p}{K_f R_m}\right)} \tag{3.12}$$

3.3.3 Laser Distance Sensor

A laser distance sensor was employed to determine the oscillator beam's displacement. The Panasonic HG-C1440-P, which has a linear analog output of 0-+5 [V] and a measuring range of 400 ± 200 [mm], was the distance sensor used. In Figure 3.9, it can be seen that when the measurement goes out of the measurement range, there is a constant output of +5.2 [V] of direct current. Some characteristics of the sensor used are summarized in Table 3.4.

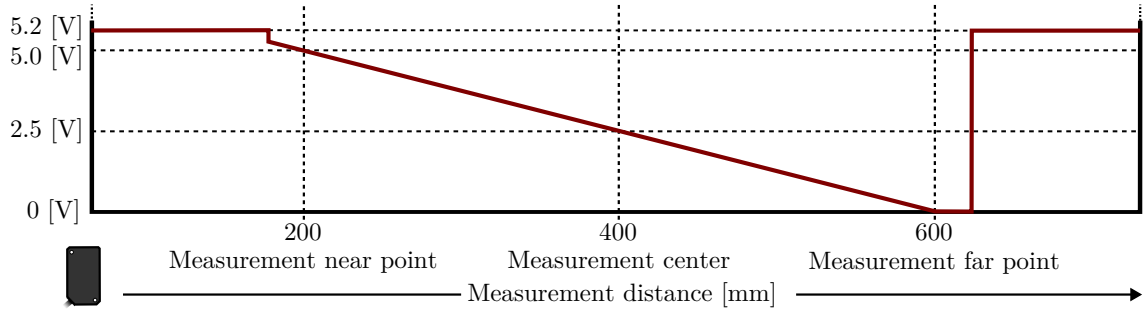

Figure 3.9: Analog voltage output of HG-C1400-P sensor.

Table 3.4: HG-C1400-P distance laser sensor specifications.

	Specifications [43]					
	Measurement range	Repeatability	Beam diameter	Supply voltage	Analog output	Response time
Value	400 ± 200 [mm]	300-800 [μm]	500 [μm]	12-24 $\pm$ 10% [V DC]	0-5[V] 4-20 [mA]	1.5, 5, and 10 [ms]

3.3.4 Signal conditioning circuit

Since the analog output of the HG-C1400-P sensor is 0 - +5 [V] and the Q2-USB data acquisition board supports a $\pm$10 [V] input with 12-bit resolution, an amplification A circuit was used to take advantage of the analog readout characteristics of the Q2-USB board. Amplification was provided by the AD620 Instrumentation Amplifier, which is a low-cost, high-precision instrumentation amplifier that allows gains of 1 to 10,000 times. Thus, the measurement range was achieved to be $\pm$7 [V]. The general schematic of the conditioning circuit is presented in Figure 3.10, while Figure 3.10 shows the approximate range of the sensor output signal compared to the output signal of the

circuit of amplification. Finally, in Table 3.5, the main characteristics of the AD620 amplifier are listed.

Table 3.5: Instrumentation amplifier AD620 specifications.

Specifications [44]						
	Supply voltage	Input voltage	Input Bias current	Input impedance	Operating temperature	Gain range
Value	±18 [V]	±10 [V]	0.5 - 2.0 [nA]	10 ‖ 2 [GΩ_pF]	−40 - +85 4-20 [°C]	1 - 10000

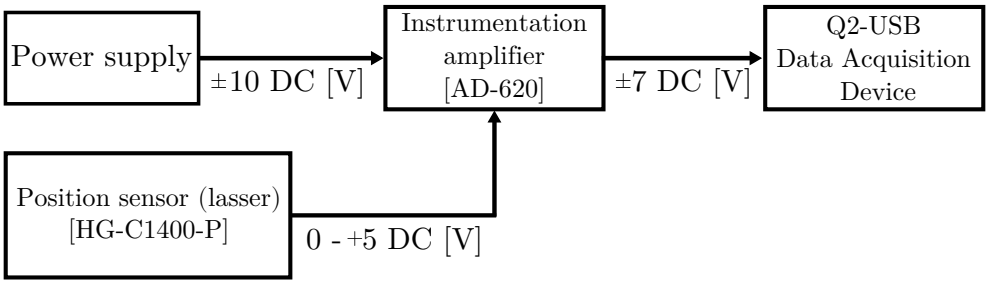

Figure 3.10: Signal conditioning circuit schema.

CHAPTER 4

System Identification

4.1 Introduction

Nonlinear behavior can be found in different engineering topics and applications. For example, in mechanics, stiffness effects, damping, and nonlinear interconnections are just a few examples of problems in vibration testing, where resonant frequencies are generated. Given the rich dynamics of nonlinear systems, their models have different levels of complexity in a high-dimensional space. In the identification process of this type of system, the structural errors of the model become more important. This problem is often inevitable and affects important areas of the identification process, such as the design of the experiment and the selection of the cost function. [45, 46].

Chaotic systems have been studied in recent decades in different areas of science, and given the close relationship between nonlinearity and chaos, what has already been mentioned must be considered in their study. For the control and synchronization applications of these systems, a proper identification process is of great importance. For these types of cases, experimental data are usually used to create the most appropriate estimator [45, 47]. Some commonly used methods are classified into different categories, for example: linearization, time and frequency domain methods, modal methods, time-frequency analysis, black box modeling, and structural model updating [48].

Any linearization is only valid for a given excitation level. Some examples of the use of the linearization method are described below. Caughey [49–51] proposed to replace a nonlinear oscillator with external Gaussian excitation with a linear one with the same excitement. However, it is well known that equivalent linearization does not correctly predict the response of strongly nonlinear random oscillators.

In time domain methods, the data considered during the identification process takes the form of series signals, for example, the restoring force surface (RFS) approach [52]; and a parallel approach called force-state mapping. An extension of the technique has been devised to cover hysteresis and chaotic systems [53–55]. Orthogonal estimation algorithms [56] have also been used, which allow the model parameters to be estimated sequentially.

A method is said to be a frequency domain method if the data considered during the identification process takes the form of a frequency response function (FRF) or spectra. One attempt to exploit data in the frequency domain was the Volterra and Wiener series. These series allow the generalization of the concepts of impulse response function and FRF to nonlinear systems [45, 57].

Multiple works have been carried out focused on the identification of chaotic systems. In [47], the importance of correct identification in the control of chaotic systems is presented. The authors

in [58] present the implementation of a swarm-type algorithm of chaotic ants for identification purposes. This type of approach was also applied in [59], where a particle swarm algorithm was used. Optimized artificial bee colony or particle swarm algorithms [60] have been used for the identification of Van Der Pol-Duffing oscillators [46], and the authors of [61] proposed the use of an extreme learning machine to identify a Duffing oscillator.

This thesis addresses the problem of identifying a Duffing oscillator, a system with cubic non-linearity, using a combination of the offline least squares method with forgetting factor and is complemented by using different filtering methods for the input and system output. The results obtained are compared and validated to verify the correct estimation of the oscillator parameters. The identification method used is described in detail below.

4.2 Mathematical model of the Duffing oscillator

The behavior of a Duffing oscillator is continuous and has multiple equilibrium points, some of which are unstable, in the case of this work, the considered system has only 3 unexcited equilibrium points, two of which are stable and one unstable, as will be defined later.

The above system can be represented by the following equation:

$$m\ddot{q}(t) + c\dot{q}(t) - k_l q(t) + k_n q^3(t) = -m\ddot{p}(t) \tag{4.1}$$

where m is the effective mass of the beam, c is the viscous damping coefficient, k_l and k_n are the linear and non-linear stiffness coefficients respectively, $q(t)$, $\dot{q}(t)$ and $\ddot{q}(t)$ are the beam position, velocity and acceleration, $\ddot{v}(t)$ is the input acceleration for the system excitation, and $u(t)$ is the control signal.

4.3 Direct physical modeling

In order to obtain the mass m and linear stiffness k_l of the real system, we can consider the beam behavior without the influence of the magnets in the frame. The Figure 4.1 represents an equivalent diagram of the beam.

In order to calculate the linear stiffness k_l, it is necessary to obtain the effective mass of the beam, as shown below.

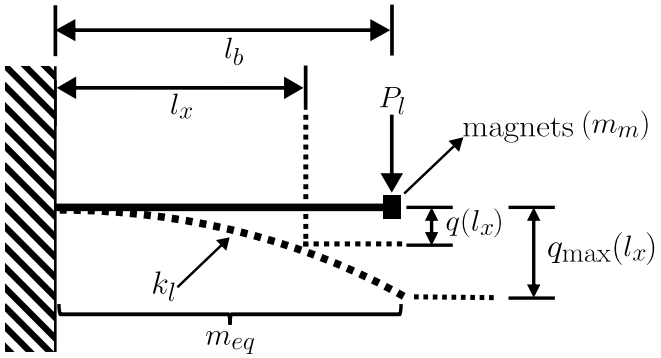

Figure 4.1: Diagram Deflection of the cantilever.

4.3.1 Effective mass

In this case, there are two main mass to consider, the beam and the magnets mass, which are mounted in the tip of the beam. The total effective mass m is given by:

$$m = m_m + m_{eq} \tag{4.2}$$

where m_m is the mass of the magnets and m_{eq} is the equivalent mass of the beam. To obtain the equivalent mass m_{eq} of the beam, we can use the equivalent diagram of a cantilever to describe it, as shown in Figure 4.1. To calculate m_{eq} we will use the deflection q and the maximum deflection $q_{\max}$ of the cantilever. In [19] the author shown that $q_{\max}$ is given by:

$$q_{\max} = \frac{P_l l^3}{3EI_b}. \tag{4.3}$$

where l is the length, E is the Young's modulus, I_b is the moment of inertia, and, P_l is a punctual load due to the mass of the beam. Singiresu [19] presented that static deflection is given by :

$$q(I_x) = \frac{P_l l_x^2}{6EI_b}(3l_b - l_x) = \frac{q_{\max} l_x^2}{2l_b^3}(3l_b - l_x) \tag{4.4}$$

The maximum kinetic energy T_{max} of the beam itself is given by [19]:

$$T_{\max} = \frac{1}{2}\int_0^1 \frac{m_b}{l_b}\left\{\dot{q}(l_x)\right\}^2 dl_x = \frac{1}{2} m_{eq}\dot{q}_{\max}^2 \tag{4.5}$$

where m_b is the total mass of the beam and (m_b/l_b) is the mass per unit length. Deriving (4.4) with respect to time prduces:

$$\dot{q}(l_x) = \frac{\dot{q}_{\max}}{2l_b^3}(3l_x^2 l_b - l_x^3) \tag{4.6}$$

$$T_{\max} = \frac{1}{2}\int_0^1 \frac{m_b}{l_b}\left\{\frac{\dot{q}_{\max}}{2l_b^3}\right\}^2 dl_x = \frac{1}{2}\left(\frac{33}{140} m_b\right)\dot{q}_{\max}^2 \tag{4.7}$$

Replacing (4.6) in (4.7):

$$\frac{1}{2} m_{eq}\dot{q}_{\max}^2 = \frac{1}{2}\left(\frac{33}{140} m_b\right)\dot{q}_{\max}^2 \tag{4.8}$$

hence, the equivalent mass of the beam is:

$$m_{eq} = \frac{33}{140} m_b \tag{4.9}$$

4.3.2 Linear and non-linear stiffness

The deflection of the beam is given by (4.3). So the linear stiffness (k_l) of the beam is given by:

$$k_l = \frac{3EI_b}{l_b^3} \tag{4.10}$$

Figure 4.2 shows a diagram of the shape of the beam, so, the moment of inertia of the beam can be calculated as [62]:

$$I_b = \frac{b_b h_b^3}{12} \tag{4.11}$$

And the natural frequency of the beam is:

$$\omega_n = \sqrt{\frac{k_l}{m}} \tag{4.12}$$

To calculate the non-linear stiffness of the system, it is necessary to obtain the equilibrium points of (4.1). For $m\ddot{v} = 0$ the system converges to one of the equilibria, so $m\ddot{q} = 0$, then (4.1) can be written as:

$$q(-k_l + k_n q^2) = 0 \tag{4.13}$$

solving for q, we have:

$$q_1 = 0 \tag{4.14}$$

$$q_{2,3} = \pm\sqrt{\frac{k_l}{k_n}} \tag{4.15}$$

where q_i and q_e are the unstable and stable equilibrium points. So, all three equilibrium points of $\dot{q}$ are at 0. Therefore, the three equilibrium points can be described in vector form of the form $\mathbf{q}^* = [q^*, \dot{q}^*]$, that is:

$$\mathbf{q}_1^* = [0, 0] \begin{bmatrix} q \\ \dot{q} \end{bmatrix} \tag{4.16}$$

$$\mathbf{q}_{2,3}^* = \left[\pm\sqrt{\frac{k_l}{k_n}}, 0\right] \begin{bmatrix} q \\ \dot{q} \end{bmatrix} \tag{4.17}$$

The linear stiffness factor can be obtained from (4.10). From position measurements is possible to know the equilibria $\mathbf{q}_e^*$, so k_n can be obtained from (4.15):

$$k_n = \frac{k_l}{q_e^{*2}} \tag{4.18}$$

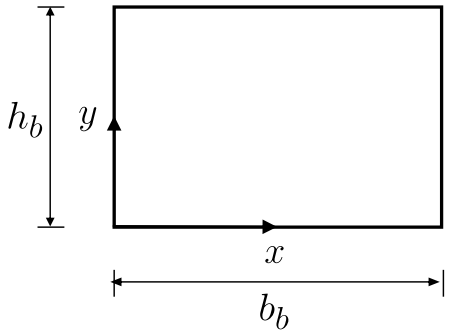

Figure 4.2: Moment of inertia diagram for a rectangular shape.

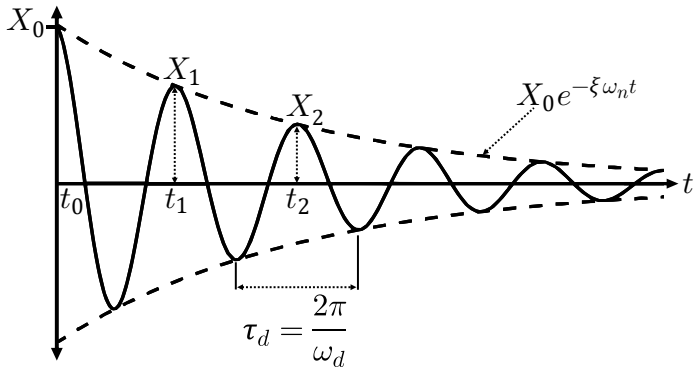

Figure 4.3: Logarithmic decrement diagram.

4.3.3 Damping coefficient

To calculate the system's damping, the logarithmic decrement method [19] is used, defined as the natural logarithm of the ratio of any two consecutive amplitudes of an underdamped free vibration system. Figure 4.3 shows the characteristic shape of a free vibrating system without constant excitation [19]. Let t_1 and t_2 denote the times corresponding to two successive measured amplitudes, X_1 and X_2. Knowing both times and amplitudes, the next ratio is formed:

$$\frac{X_1}{X_2} = \frac{X_0 \exp^{-\xi\omega_n t_1} \cos(\omega_d t_1 - \phi_0)}{X_0 \exp^{-\xi\omega_n t_2} \cos(\omega_d t_2 - \phi_0)} \tag{4.19}$$

where, $\tau_d = 2\pi/\omega_d$ and ω_d are the period and the frequency of the underdamped oscillation respectively, ω_n is the natural frequency of the cantilever, X_0 is the amplitude at $t = 0$. However, because t_1 and t_2 are the times of the consecutive amplitudes, $t_2 = t_1 + \tau_d$. Hence:

$$\cos(\omega_d t_2 - \phi_0) = \cos(2\pi + \omega_d t_1 - \phi_0) = \cos(\omega_d t_1 - \phi_0) \tag{4.20}$$

So (4.19) can be written as:

$$\frac{X_1}{X_2} = \frac{\exp^{-\xi\omega_n t_1} X_0 \cos(\omega_d t_1 - \phi_0)}{\exp^{-\xi\omega_n (t_1+\tau_d)} X_0 \cos(\omega_d t_1 - \phi_0)} = \frac{\exp^{-\xi\omega_n t_1}}{\exp^{-\xi\omega_n (t_1+\tau_d)}} \tag{4.21}$$

The logarithmic decrement δ can be obtained from (4.21) as:

$$\delta = \ln \frac{X_1}{X_2} = \frac{2\pi\xi}{\sqrt{1-\xi^2}} \tag{4.22}$$

The value of δ is dimensionless, and the damping ratio ξ can be obtained from (4.22):

$$\xi = \frac{\delta}{\sqrt{(2\pi)^2 + \delta^2}}, \tag{4.23}$$

so the viscous damping parameter is given by:

$$c = 2\xi\omega_n m. \tag{4.24}$$

4.4 Least Mean Squares Algorithm

The least squares algorithm is probably the most popular and one of the most used in practice [63]. The servomechanism's input and output signals are used as inputs by the constructed algorithm, which employs the direct identification approach. The LMS algorithm, as well as others related to it, are widely used in various applications of adaptive filtering. The convergence speed of the LMS is shown to be dependent on the eigenvalue spread of the input signal correlation matrix [64].

Finding the model parameters that provide an estimated model with N observations that best fits the actual system is the current task. Gauss originally accomplished this goal in 1795 by deriving the least squares method. First, the observation error, defined as [65], was introduced in order to determine the best fit.

$$error = real\ system\ output - \ estimated\ system\ output$$

It is necessary to parametrize the system as follows:

$$z(t) = \boldsymbol{\phi}^{\mathrm{T}}(t)\boldsymbol{\theta} \tag{4.25}$$

where $z \in \mathbb{R}$ is a measurable signal, $\boldsymbol{\phi} = [\phi_1, \phi_2, \cdots, \phi_n]^{\mathrm{T}} \in \mathbb{R}^{n\times 1}$ is a vector of measurable signals, and $\boldsymbol{\theta} = [\theta_1, \theta_2, \cdots, \theta_n]^{\mathrm{T}} \in \mathbb{R}^{n\times 1}$ is the vector of parameters to be estimated.

4.4.1 Offline Least Mean Squares

The Least Mean Squares generates a vector $\widehat{\boldsymbol{\theta}}$ that minimizes the following function:

$$J(\widehat{\boldsymbol{\theta}}) = \sum_{k=1}^{N} \left(z(k) - \boldsymbol{\phi}^{\mathrm{T}}(k)\widehat{\boldsymbol{\theta}}\right)^2, \ J(\widehat{\boldsymbol{\theta}}) \in \mathbb{R} \tag{4.26}$$

where N is the number of samples. The $J(\widehat{\boldsymbol{\theta}})$ function can be written in a matrix form as:

$$J(\widehat{\boldsymbol{\theta}}) = (\mathbf{z}_k - \boldsymbol{\Phi}_k\widehat{\boldsymbol{\theta}})^{\mathrm{T}}(\mathbf{z}_k - \boldsymbol{\Phi}_k\widehat{\boldsymbol{\theta}}) \tag{4.27}$$

where $\mathbf{z}_k = [z(k), z(k+1), \cdots, z(N)]^{\mathrm{T}}$ and $\boldsymbol{\Phi}_k = [\boldsymbol{\phi}(1), \boldsymbol{\phi}(2), \cdots, \boldsymbol{\phi}(k)]^{\mathrm{T}}$, $N \geq 2$.

The function $J(\widehat{\theta})$ that minimizes the LMS can be written as:

$$J(\widehat{\boldsymbol{\theta}}) = \mathbf{z}_k^{\mathrm{T}}\mathbf{z}_k - 2\widehat{\boldsymbol{\theta}}^{\mathrm{T}}\boldsymbol{\Phi}_k^{\mathrm{T}}\mathbf{z}_k + \widehat{\boldsymbol{\theta}}^{\mathrm{T}}\boldsymbol{\Phi}_k^{\mathrm{T}}\boldsymbol{\Phi}_k\widehat{\boldsymbol{\theta}} \tag{4.28}$$

$J(\widehat{\boldsymbol{\theta}})$ is a convex function. The partial derivative of $J(\boldsymbol{\theta})$ with respect to $\boldsymbol{\theta}$ is given by:

$$\frac{\partial}{\partial\widehat{\boldsymbol{\theta}}}J(\widehat{\boldsymbol{\theta}}) = \frac{\partial}{\partial\widehat{\theta}}\left[\mathbf{z}_k^T\mathbf{z}_k\right] - \frac{\partial}{\partial\widehat{\boldsymbol{\theta}}}\left[2\widehat{\boldsymbol{\theta}}^T\boldsymbol{\Phi}_k^T\mathbf{z}_k\right] + \frac{\partial}{\partial\widehat{\boldsymbol{\theta}}}\left[\widehat{\boldsymbol{\theta}}^T\boldsymbol{\Phi}_k^T\boldsymbol{\Phi}_k\widehat{\boldsymbol{\theta}}\right]. \tag{4.29}$$

The minimum of $J(\widehat{\boldsymbol{\theta}})$ is obtained by applying the gradient $\nabla J(\widehat{\boldsymbol{\theta}})$ and setting it equal to zero.

$$\nabla J(\widehat{\boldsymbol{\theta}}) = -2\boldsymbol{\Phi}_k^{\mathrm{T}}\mathbf{z}_k + 2\boldsymbol{\Phi}_k^{\mathrm{T}}\boldsymbol{\Phi}_k\widehat{\boldsymbol{\theta}} = 0 \tag{4.30}$$

so:

$$\boldsymbol{\Phi}_k^{\mathrm{T}}\mathbf{z}_k = \boldsymbol{\Phi}_k^{\mathrm{T}}\boldsymbol{\Phi}_k\widehat{\boldsymbol{\theta}}, \tag{4.31}$$

hence

$$\widehat{\boldsymbol{\theta}} = \left[\boldsymbol{\Phi}_k^{\mathrm{T}}\boldsymbol{\Phi}_k\right]^{-1}\boldsymbol{\Phi}_k^{\mathrm{T}}\mathbf{z}_k. \tag{4.32}$$

Writing (4.32) in the form of sums:

$$\widehat{\boldsymbol{\theta}} = \left[\sum_{k=1}^{N}\boldsymbol{\phi}(k)\boldsymbol{\phi}(k)^T\right]^{-1}\left[\sum_{k=1}^{N}\boldsymbol{\phi}(k)z(k)\right] \tag{4.33}$$

The offline LSM is represented by the above equation; N samples of $\boldsymbol{\phi}, \mathbf{z}$ are acquired, and then an estimate of $\widehat{\boldsymbol{\theta}}$ is made. As will be demonstrated in Section 4.4.2, a model's parameters can also be estimated online, meaning that the estimated $\widehat{\boldsymbol{\theta}}$ can be updated each time a sample is collected.

Theorem 1 (Convergence of the Parameter Estimation of a Non-Linear Static Process)**.** *The parameters $\boldsymbol{\theta}$ of a time-invariant non-linear system can be estimated by the LSM method if the following conditions are met:*

- *The input signal is measurable.*
- $det\left(\boldsymbol{\Phi}_k^{\mathrm{T}}\boldsymbol{\Phi}_k\right) \neq 0$
- *The disturbance is stationary and has zero mean.*
- *The input signal is not correlated with the disturbance*

4.4.2 Online Recursive Least Squares Method (RLSM) with forgetting factor

The online discrete least squares method with forgetting factor is given by the following expressions:

$$\widehat{\boldsymbol{\theta}}(k) = \widehat{\boldsymbol{\theta}}(k-1) + \mathbf{L}(k)e(k) \tag{4.34}$$

$$\mathbf{L}(k) = \frac{\mathbf{P}(k-1)\boldsymbol{\phi}(k)}{\lambda_{ff}(k) + \boldsymbol{\phi}^{\mathrm{T}}(k)\mathbf{P}(k-1)\boldsymbol{\phi}(k)} \tag{4.35}$$

$$\mathbf{P}(k) = \frac{1}{\lambda_{ff}(k)}\left[\mathbf{P}(k-1) - \frac{\mathbf{P}(k-1)\boldsymbol{\phi}(k)\boldsymbol{\phi}^{\mathrm{T}}(k)\mathbf{P}(k-1)}{\lambda_{ff}(k) + \boldsymbol{\phi}^{\mathrm{T}}(k)\mathbf{P}(k-1)\boldsymbol{\phi}(k)}\right] \tag{4.36}$$

$$e_i(k) = z(k) - \widehat{z}(k) = z(k) - \boldsymbol{\phi}^{\mathrm{T}}(k)\widehat{\boldsymbol{\theta}}(k-1) \tag{4.37}$$

where $\widehat{\boldsymbol{\theta}}(k)$ is an estimate of $\boldsymbol{\theta}$ from parameterization (4.45), $\boldsymbol{\phi}(k)$ is the regressor, $\mathbf{P}(k)$ is the gain matrix, $\mathbf{z}(k)$ is the output signal from parameterization, $\mathbf{e}_i(k)$ is the prediction error and $\boldsymbol{\lambda}_{ff}(k)$ is the forgetting factor. For systems with time-varying parameters, it is known that the most common way to choose the forgetting factor is as a positive constant, always chosen slightly less than or equal to one.

Theorem 2 (Persistency excitation [63,66])**.** *For the vector of estimated parameters $\widehat{\boldsymbol{\theta}}$ to converge to the vector of real parameters $\boldsymbol{\theta}$, the regression vector $\boldsymbol{\phi}(k)$ of the identification algorithm that estimates $\widehat{\boldsymbol{\theta}}$ must satisfy the following persistent excitation condition [66]:*

$$\lim_{k\to\infty}\Omega_k = \lim_{k\to\infty}\lambda_{\min}\left[\sum_{k=1}^{N}\phi(k)\phi^{\mathrm{T}}(k)\right] = \infty \tag{4.38}$$

where $\lambda_{\min}[\cdot]$ is the smallest eigenvalue of $\sum_{k=1}^{N}\phi(k)\phi^{\mathrm{T}}(k)$ for every iteration.

4.5 Bistable Duffing oscillator model parametrization

The values of the viscous damping coefficient c, the linear stiffness k_l, and the non-linear stiffness k_n must be known in order to control the system; various filtering techniques used for parameter estimation are used for these reasons. First, using the formulas and theories given in Section 4.3, these parameters were determined analytically.

A better approximation of the built prototype model was obtained because (4.1) is an approximate model of the system, and different parametrization methods were used to compare and contrast the results. Recursive Least Mean Squares (RLMS) with the forgetting factor was used to carry out the identification, allowing for online implementation.

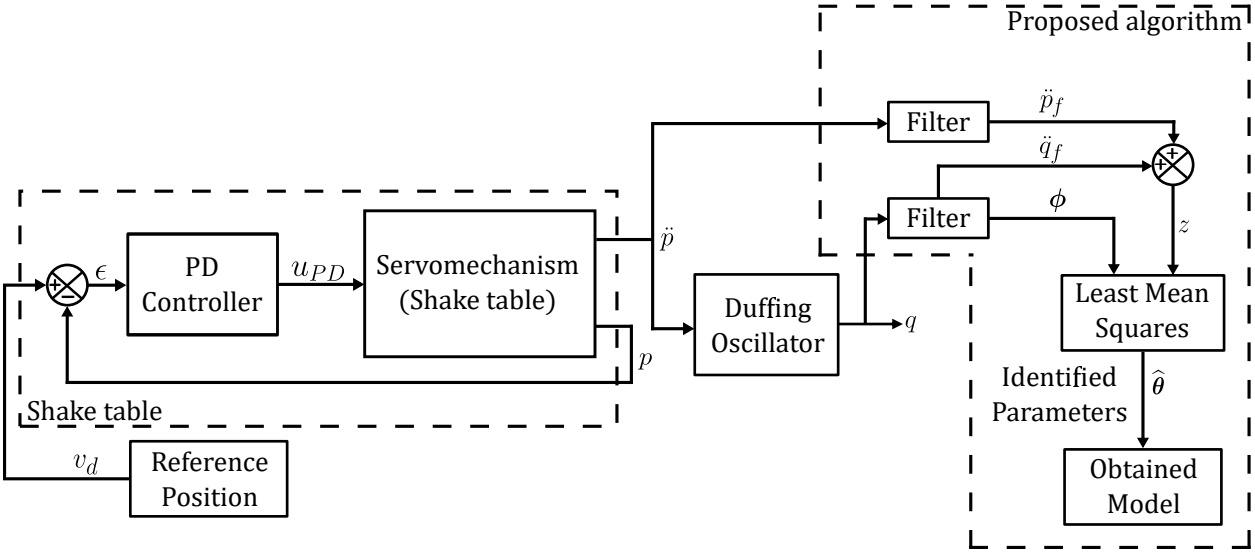

Figure 4.4: Block diagram of the proposed identification method.

Identifying the parameters of an uncertain system requires parameterization, and it consists of writing (4.1) in the form of (4.25).

Consider the system model described by (4.1), it can be written as:

$$\ddot{q}(t) + \alpha\dot{q}(t) - \beta q(t) + \gamma q^3(t) = -\ddot{p}(t) \tag{4.39}$$

where m is known, $\alpha = c/m$, $\beta = k_l/m$, and $\gamma = k_n/m$. Supposing the control signal and initial conditions are equal to zero, the Laplace transform of (4.39) is given by:

$$s^2Q(s) = -s\alpha Q(s) + \beta Q(s) - \gamma\mathcal{L}\{q^3\} - s^2P(s) \tag{4.40}$$

where $\mathcal{L}$ is the Laplace operator.

The parameterization process consists of multiplying both sides of the previous equation by a filter $F(s)$ in order to estimate the parameters via measurements from the position $q(t)$ and the input acceleration $\ddot{w}(t)$, obtaining the following expression:

$$s^2F(s)Q(s) + s^2F(s)P(s) = -s\alpha F(s)Q(s) + \beta F(s)Q(s) - \gamma F(s)\mathcal{L}\{q^3(t)\} \tag{4.41}$$

4.5.1 Continuous filter parametrization

Consider the following filter: $F_c(s) = \lambda_2/(s^2 + \lambda_1 s + \lambda_2)$. Applying the filter $F_c(s)$ previously defined to (4.41), we have:

$$\begin{aligned}\frac{s^2\lambda_2}{s^2+\lambda_1 s+\lambda_2}Q(s) = -\alpha\frac{s\lambda_2}{s^2+\lambda_1 s+\lambda_2}Q(s) + \beta\frac{\lambda_2}{s^2+\lambda_1 s+\lambda_2}Q(s) \\ -\gamma\frac{\lambda_2}{s^2+\lambda_1 s+\lambda_2}\mathscr{L}\{q^3\} - \frac{\lambda_2 s^2}{s^2+\lambda_1 s+\lambda_2}P(s)\end{aligned} \tag{4.42}$$

By defining $Q_f(s) = Q(s)F_c(s)$ and $P_f(s) = P(s)F_c(s)$, equation (4.42) in the time domain is given by:

$$\ddot{q}_f(t) = -\alpha\dot{q}_f(t) + \beta q_f(t) - \gamma q_f^3(t) - \ddot{p}_f(t) \tag{4.43}$$

where the subscript f means filtered quantities. Changing the variable of (4.43) gives us:

$$z(t) = -\zeta\phi_1(t) + k_l\phi_2(t) - k_n\phi_3(t) \tag{4.44}$$

where $z(t) = \ddot{q}_f(t) + \ddot{p}_f(t)$, $\phi_1(t) = \dot{q}_f$, $\phi_2(t) = q_f$ and $\phi_3(t) = q_f^3$. With the model described now with (4.44) we can write (4.39) as (4.25):

$$z(t) = \boldsymbol{\phi}^{\mathrm{T}}(t)\boldsymbol{\theta} \tag{4.45}$$

where $z(t) = \ddot{q}_f(t) + \ddot{p}_f(t)$, $\boldsymbol{\phi}_i = [\phi_1(t), \phi_2(t), \phi_3(t)]^{\mathrm{T}}$, and $\boldsymbol{\theta} = [\alpha, \beta, \gamma]^{\mathrm{T}}$.

4.5.2 Discrete filter parametrization

The discrete filters were obtained getting the Z-transform of (4.42) using Tustin method.

$$z(kT_s) = \boldsymbol{\phi}^{\mathrm{T}}(kT_s)\boldsymbol{\theta} \tag{4.46}$$

where $\boldsymbol{\phi} = \left[\dot{q}_f(kT_s), q_f(kT_s), q_f^3(kT_s)\right]^{\mathrm{T}}$, $\boldsymbol{\theta} = [\alpha, \beta, \gamma]^{\mathrm{T}}$, T_s is the sampling period, $k = 1, 2, \cdots, N$, and N is the number of samples.

4.5.3 Linear Integral filter parametrization

Consider the following integrator operator:

$$\mathcal{I}_n\{\rho(t)\} = \frac{g_i}{\delta_i^n}\int_{t-\delta}^{t}\int_{\tau_1-\delta}^{\tau_1}\cdots\int_{\tau_{n_1}-\delta}^{\tau_1}\rho(\tau_n)d\tau_n\cdots d\tau_1 \tag{4.47}$$

where g_i is a user-defined gain, δ is a time window that depends on the sampling period (T_s), and n is the number of integrals to apply to the function $\rho(t)$. In this case, g_i/δ^n serves as the filter gain. The following formula provides the value of δ:

$$\delta_i = rT_s \tag{4.48}$$

where T_s is the sampling period and r is the filter's length factor. To approximate the frequency of the system under study, the value of r for the filter's bandwidth should be selected. The integral operator's Laplace transform is defined as follows:

$$\mathscr{L}\left[\mathcal{I}_n\{\rho(t)\}\right] = g_i\left(\frac{1-e^{-\delta_i s}}{\delta_i s}\right)^n \mathscr{L}\{\rho(t)\} \tag{4.49}$$

As a pre-filter from measured signals, the integral operator $\mathcal{I}_n\{\rho(t)\}$ is helpful in removing offsets and measurement noise [66, 67]. Using $\mathcal{I}_1$ as an operator on (4.1) produces:

$$\frac{g_i}{\delta_i}\left[\int_{t-\delta}^{t}\ddot{q}(\tau)d\tau + \int_{t-\delta}^{t}\ddot{p}(\tau)d\tau = -\int_{t-\delta}^{t}\alpha\dot{q}(\tau)d\tau + \int_{t-\delta}^{t}\beta q(\tau)d\tau - \int_{t-\delta}^{t}\gamma q(\tau)d\tau\right] \tag{4.50}$$

$$\frac{g_i}{\delta_i}\left[\dot{q}(t) - \dot{q}(t-\delta_i) + \dot{p}(t) - \dot{p}(t-\delta_i) = \alpha[q(t) - q(t-\delta_i)] + \beta\int_{t-\delta_i}^{t} q(\tau)d\tau - \gamma\int_{t-\delta_i}^{t} q(\tau)d\tau\right] \tag{4.51}$$

So, if we apply the operator $\mathcal{I}_4\{\rho(t)\}$ on (4.1) we have:

$$\begin{aligned}\frac{g_i}{\delta_i^4}\Bigg[\int_{t-\delta_i}^{t}\int_{\tau_1-\delta_i}^{\tau_1}[q(\tau_2) - 2(\tau_2-\delta_i) + q(\tau_2-2\delta_i)d\tau_2 d\tau_1] + \int_{t-\delta_i}^{t}\int_{\tau_1-\delta_i}^{\tau_1}\int_{\tau_2-\delta_i}^{\tau_2}\int_{\tau_3-\delta_i}^{\tau_3}\ddot{v}(\tau_4)d\tau_4 d\tau_3 d\tau_2 d\tau_1 = \\ -\alpha\int_{t-\delta_i}^{t}\int_{\tau_1-\delta_i}^{\tau_1}\int_{\tau_2-\delta_i}^{\tau_2}[q(\tau_3) - q(\tau_3-\delta_i)]\,d\tau_3 d\tau_2 d\tau_1 + \beta\int_{t-\delta_i}^{t}\int_{\tau_1-\delta_i}^{\tau_1}\int_{\tau_2-\delta_i}^{\tau_2}\int_{\tau_3-\delta_i}^{\tau_3} q(\tau_4)d\tau_4 d\tau_3 d\tau_2 d\tau_1 \\ -\gamma\int_{t-\delta_i}^{t}\int_{\tau_1-\delta_i}^{\tau_1}\int_{\tau_2-\delta_i}^{\tau_2}\int_{\tau_3-\delta_i}^{\tau_3} q^3(\tau_4)d\tau_4 d\tau_3 d\tau_2 d\tau_1\Bigg]\end{aligned} \tag{4.52}$$

Defining $F_i(s) = \mathscr{L}[\mathcal{I}_4\rho(t)]$, hence, the Laplace transform of (4.52) can be written as:

$$s^2F_i(s)Q(s) + s^2F_i(s)P(s) = -s\alpha F_i(s)Q(s) + \beta F_i(s)Q(s) - \gamma F_i(s)\mathscr{L}\{q^3(t)\} \tag{4.53}$$

where $F(s)$ is the following fourth-order filter:

$$F_i(s) = \frac{g_i}{\delta_i^4}\left(\frac{1-e^{\delta_i s}}{s}\right)^4, \tag{4.54}$$

whose magnitude and cut-off frequency are given by the following expressions:

$$mag[F_i(s)] = |F_i(j\omega)| = \frac{g_i}{\delta_i^4}\left|\delta_i\frac{\sin(\pi\omega/\omega_0)}{\pi\omega/\omega_0}\right|^4, \quad \omega_0 = \frac{2\pi}{\delta_i}, \tag{4.55}$$

from (4.53) the filters F_{i_1}, H_{i_2} and H_{i_3} can be defined as:

$$F_{i_1} = F_i(s),\ F_{i_2} = sF_i(s),\ \text{and}\ F_{i_3} = s^2F_i(s) \tag{4.56}$$

The inverse Laplace transform of (4.53) is given by: defining $Q_f(s) = Q(s)F(s)$ and $P_f(s) = P(s)F(s)$, where the subscript f indicates filtered quantities

$$\frac{g_i}{\delta^4}z(t) = \frac{g_i}{\delta^4}\left[\boldsymbol{\phi}^{\mathrm{T}}(t)\boldsymbol{\theta}\right] \tag{4.57}$$

where $z(t) = \mathscr{L}^{-1}\left[\mathcal{I}_4\{\ddot{q}(t) + \ddot{p}(t)\}\right]$, $\boldsymbol{\phi}_i = [\phi_{i_1}(t), \phi_{i_2}(t), \phi_{i_3}(t)]^{\mathrm{T}}$, and $\boldsymbol{\theta} = [\alpha, \beta, \gamma]^{\mathrm{T}}$. The parametrization signals are:

$$\phi_{i_1}(t) = -\alpha \int_{t-\delta_i}^{t} \int_{\tau_1-\delta_i}^{\tau_1} \int_{\tau_2-\delta_i}^{\tau_2} \left[q(\tau_3) - q(\tau_3 - \delta_i)\right] d\tau_3 \tau_2 d\tau_1 \tag{4.58}$$

$$\phi_{i_2}(t) = \beta \int_{t-\delta_i}^{t} \int_{\tau_1-\delta_i}^{\tau_1} \int_{\tau_2-\delta_i}^{\tau_2} \int_{\tau_3-\delta_i}^{\tau_3} q(\tau_4) d\tau_4 d\tau_3 d\tau_2 d\tau_1 \tag{4.59}$$

$$\phi_{i_3}(t) = -\gamma \int_{t-\delta_i}^{t} \int_{\tau_1-\delta_i}^{\tau_1} \int_{\tau_2-\delta_i}^{\tau_2} \int_{\tau_3-\delta_i}^{\tau_3} q^3(\tau_4) d\tau_4 d\tau_3 d\tau_2 d\tau_1 \tag{4.60}$$

4.6 Results

This section presents the results of the identification process of the built prototype, as well as the design and calculations of the methods used in this chapter. In this order, direct physical modeling is presented; the design of the filters used for the parameterization of the system, as well as its frequency response; the results of the identification by LSM; and the validation of the estimated parameters.

4.6.1 Direct physical modeling

The modeling of the real system is then obtained. The magnets at the tip have a mass of $m_m = 0.0228$ [kg], and the beam has a mass of $m_{beam} = 0.0206$ [kg]. The equivalent mass of the beam is determined from Section 4.3.1; hence, $m_{eq} = 0.0049$ [kg]. The effective mass that results is therefore $m = 0.027[kg]$.

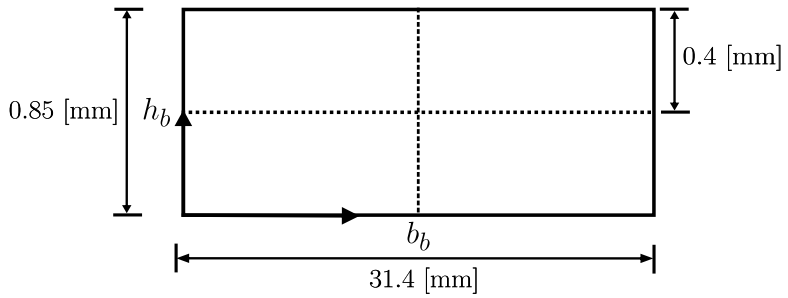

Figure 4.5: Dimensions of the beam.

Equations from Section 4.3.2 were used to calculate the linear and non-linear stiffness; Figure 4.5 shows the dimensions of the beam of the prototype, which were used to calculate its second moment of inertia. Using (4.11) $I_x = 1.6 \times 10^{-12}$ [m^4]. The beam is mainly made of aluminum, so Young's modulus of aluminum is $E = 6.3 \times 10^{10}$ [N/m^2]. It was used (4.10) to calculate the linear stiffness k_l of the beam, obtaining $k_l = 10.7$ [N/m]. Since the equilibrium points are given by (4.15), the non-linear stiffness can be calculated from the magnitude of (4.15), so $k_n = 1.106 \times 10^4$ [N/m^3]. For the next identification experiments, it is necessary to know the natural frequency of the beam, from (4.12) $\omega_n = 3.13$ [Hz]

The logarithmic decrement method outlined in Section 4.3.3 was utilized to obtain the viscous damping. The experimental result of the beam oscillating freely without any magnetism on the structure is shown in Figure 4.6; this behavior is comparable to that of Figure 4.3. Equations (4.22) through (4.24) from Section 4.3.3 were applied to determine the viscous damping coefficient for the two consecutive amplitudes shown in the figure below.

The two consecutive amplitudes are $X_1 = 0.00781624$ [m] and $X_2 = 0.00759612$ [m], so $\delta = 0.028566$, then calculating ξ, obtaining $\xi = 0.0045463$, finally the viscous damping coefficient value obtained is $c = 0.004947$, and $\zeta = c/m = 0.17889$ [N·m/s·kg].

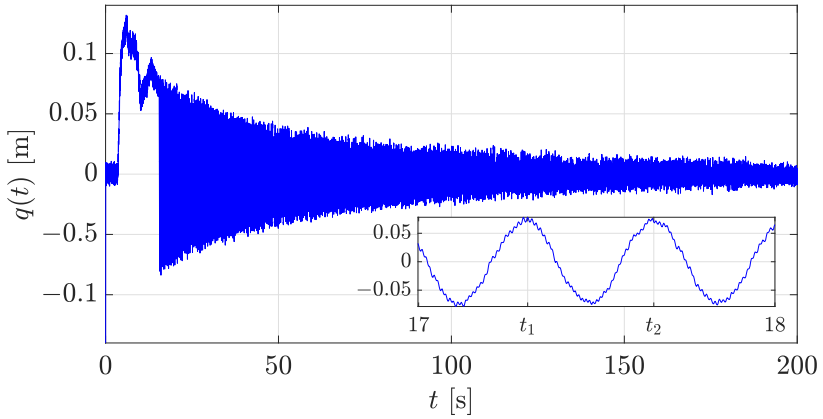

Figure 4.6: Logarithmic decrement experiment.

4.6.2 Filters frequency response

The continuous filter designed for identifications experiments used the following values for $\lambda_1 = 40$ and $\lambda_2 = 400$, so:

$$F_c(s) = \frac{400}{s^2 + 40s + 400} \tag{4.61}$$

The frequency response of the filters used is shown in Figure 4.7.

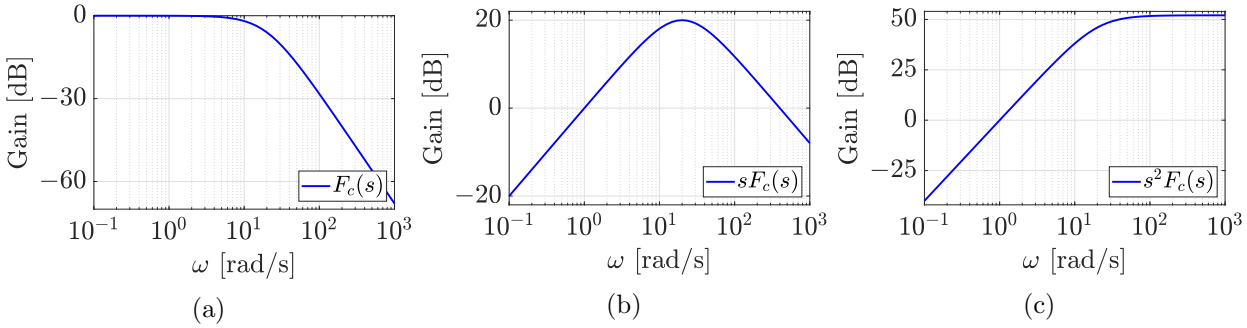

Figure 4.7: Magnitude of the frequency response of continuous filters.

The discrete filters used for identification experiments were obtained by getting the z transform

of the continuous filters $F_c(s)$, $sF_c(s)$, and $s^2F_c(s)$:

$$F_{z_1}(z) = \mathcal{Z}\{F_c(s)\} = \mathcal{Z}\left\{\frac{400}{s^2+40s+400}\right\} = \frac{0.000779z + 0.0007585}{z^2 - 1.922z + 0.9231} \tag{4.62}$$

$$F_{z_2}(z) = \mathcal{Z}\{sF_c(s)\} = \mathcal{Z}\left\{\frac{400s}{s^2+40s+400}\right\} = \frac{-0.7686z + 0.7686}{z^2 - 1.922z + 0.9231} \tag{4.63}$$

$$F_{z_3}(z) = \mathcal{Z}\{s^2F_c(s)\} = \mathcal{Z}\left\{\frac{400s^2}{s^2+40s+400}\right\} = \frac{400z^2 - 799.7z + 399.7}{z^2 - 1.922z + 0.9231} \tag{4.64}$$

The frequency response of the filters used is the same as the continuous filters, because what was changed was their representation. So Figure 4.7 represents the same response for this filters.

From Section 4.5.3, the equations (4.54) to (4.56) are used to obtain the frequency response of the filters based on integrals F_{i_1}, F_{i_2}, and F_{i_3} whose response is shown in Figure 4.8.

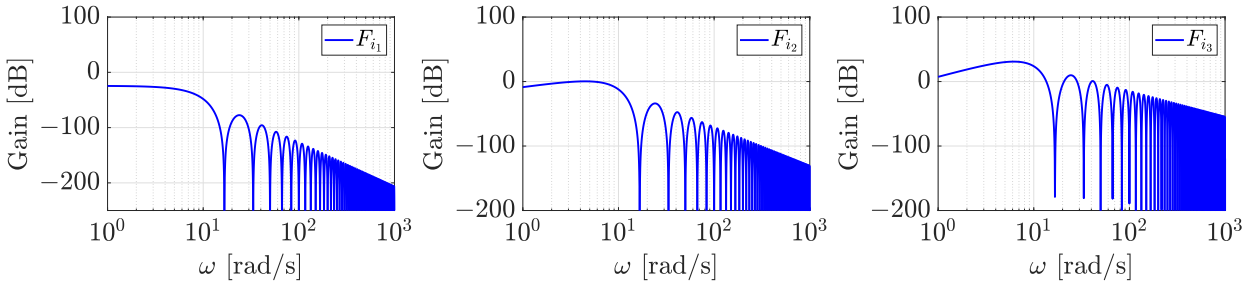

(a) (b) (c)

Figure 4.8: Magnitude of the frequency response of integral filters.

4.6.3 Parameters identification

For identification, the position of the shake table was given by the addition of two harmonic signals: 0.5 [cm] magnitude and 3 [Hz] frequency, and 0.2 [cm] magnitude and 2 [Hz]. Thus, the acceleration of the shake table is:

$$\ddot{p}(t) = \frac{d^2}{dt^2}\left[0.5\sin 6\pi + 0.2\sin 2\pi\right] \ \ [\mathrm{m/s^2}] \tag{4.65}$$

The system exhibits a frequency-rich behavior given its excitation. The fast Fourier transform, as illustrated in Figure 4.9, can be used to observe that while the frequency of 3 [Hz] is predominant, the effects of 2, 4, 6, 8, and 9 [Hz] are also discernible. This further indicates that there are several resonance frequencies in the system.

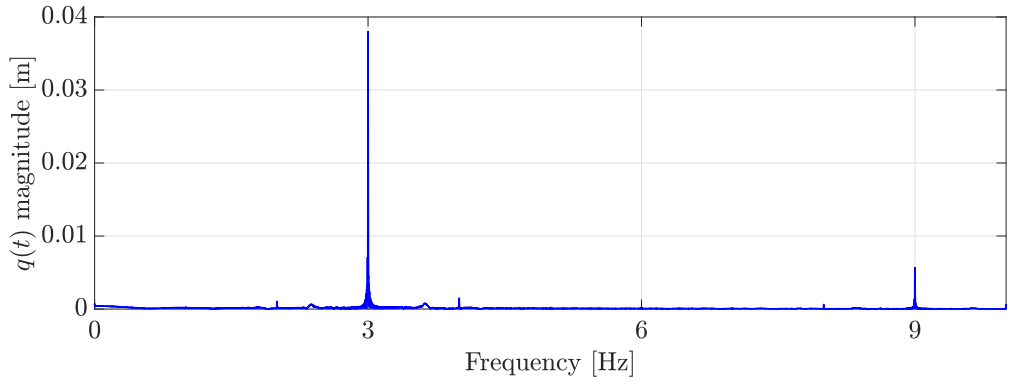

Figure 4.9: Fast Fourier transform from measured position during identification.

Figures 4.10, which display three graphs illustrating the behavior of the estimated values of each parameter and a comparison of the filtering techniques, display the results of the identification of each parameter. It is possible to distinguish between the various approaches. It is important to emphasize that the values found using the analytical modeling of the system are most similar to the results obtained using the discrete filters. Section 4.6.5 presents a comparison of the identification validation carried out with each method.

The result of identifying the viscous damping coefficient is shown in Figure 4.10; this parameter was found to be the most different from the value obtained analytically (Figure 4.10). b. The linear stiffness of the beam's obtained result is shown. It is simpler to understand the variations in the outcomes for each of the filtering techniques in this graph. Moreover, one can observe that the identification with integral filters converges a little bit quicker.

Table 4.1 summarizes the outcomes for all of the applied filtering and identification techniques. It is simpler to understand the disparity between the values obtained in this way. The values in the table are those that were used for the experimental validation of the suggested identification, observer states, and controller in the ensuing experiments.

Table 4.1: Identified parameters from the four parametrization methods.

Method	**Identified values**		
	ζ/m [N·m/s·kg]	k_l/m [N/m·kg]	k_n/m [N/m^3·kg]
Physical	0.1789	387.0638	4.0012×10^5
Integral	0.3757	462.1897	5.8881×10^5
Continuous	0.3862	527.9839	6.4535×10^5
Discrete	0.4372	366.3472	5.3209×10^5

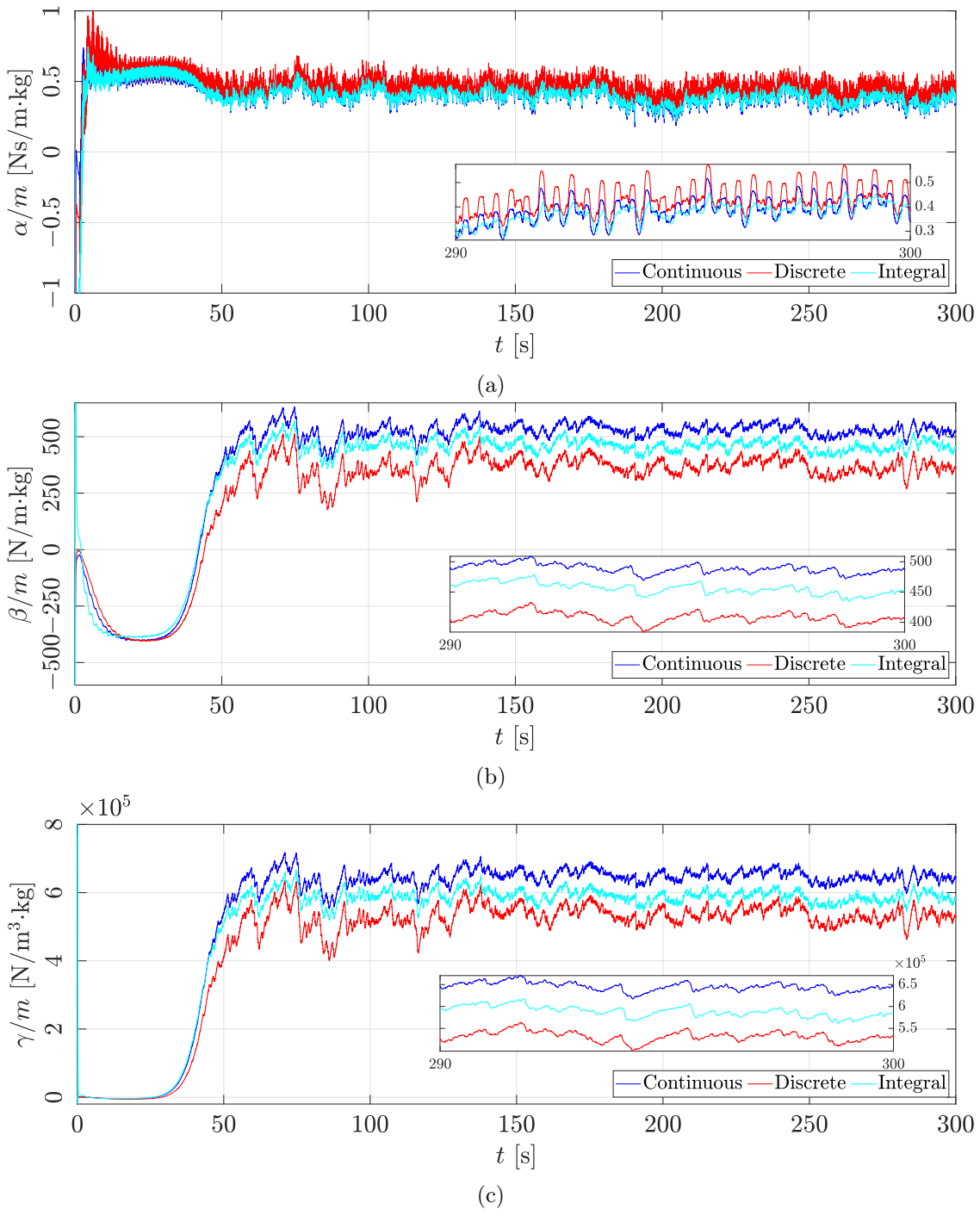

Figure 4.10: Identification results. a) Damping coefficient identification. b) Linear stiffness coefficient identification. c) Non-linear stiffness coefficient identification.

4.6.4 Persistency excitation validation

The persistent excitation described in Theorem 2 was employed to verify the convergence of the values found for the parameters α, β, and γ. Figures 4.11 from a) to c) display the outcome of applying the equation (4.38) to the data collected during the experiment. The graphs in all three scenarios show that the LSM used for identification is convergent, despite their slow growth rates.

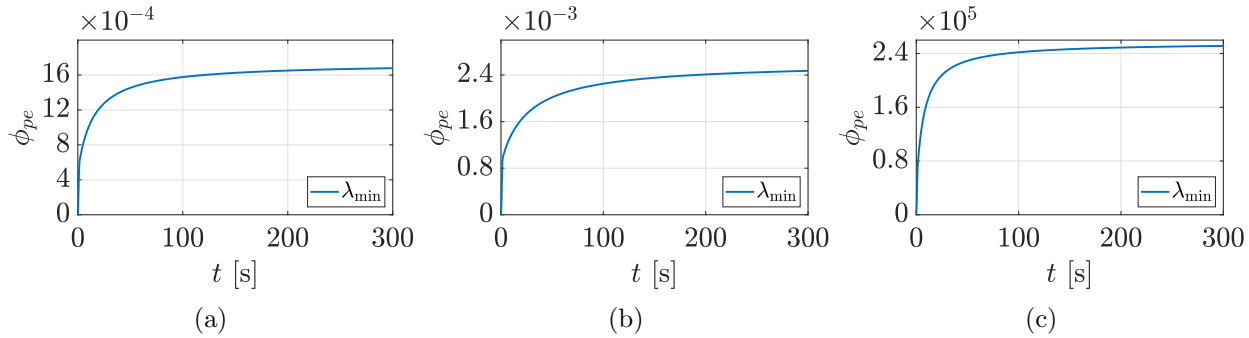

Figure 4.11: Results: Persistence of excitation (PE) condition validation for a) continuous parametrization, b) discrete parametrization, and c) integral parametrization.

4.6.5 Validation

A summary of the identification results validation process is shown in Figure 4.12. Essentially, four models are constructed with the estimated parameters and applied with the same excitation as the actual system. For every type of behavior, similar initial conditions were taken into account. Given that the aforementioned conditions yield the same kind of behavior, it was determined that the estimated parameters are accurate enough.The process was carried out for the interwell behavior shown in Figure 4.13; Figures 4.14 and 4.15 show the validation for both wells of attraction of the intrawell behavior; for the chaotic case, the characteristics of this type of system must be considered; small changes cause very different results; however, despite the difference in the trajectories, they are all chaotic, as shown in Figure 4.16, thus validating the estimated parameters with each filtering and identification method.

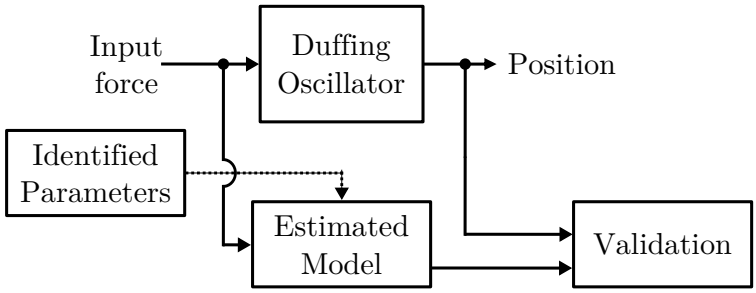

Figure 4.12: Validation proposed method.

The direct estimated model exhibits a larger beam movement amplitude than the others, as seen in Figure 4.13. This effect is also observed in the remaining validation experiments. Nonetheless, it is the model that most closely approximates the system's actual equilibrium points when it comes

to intrawell behavior. In addition, it is easier to see the measurement disturbances caused by the laser position sensor in the graphs presented in Figures 4.14 and 4.15.

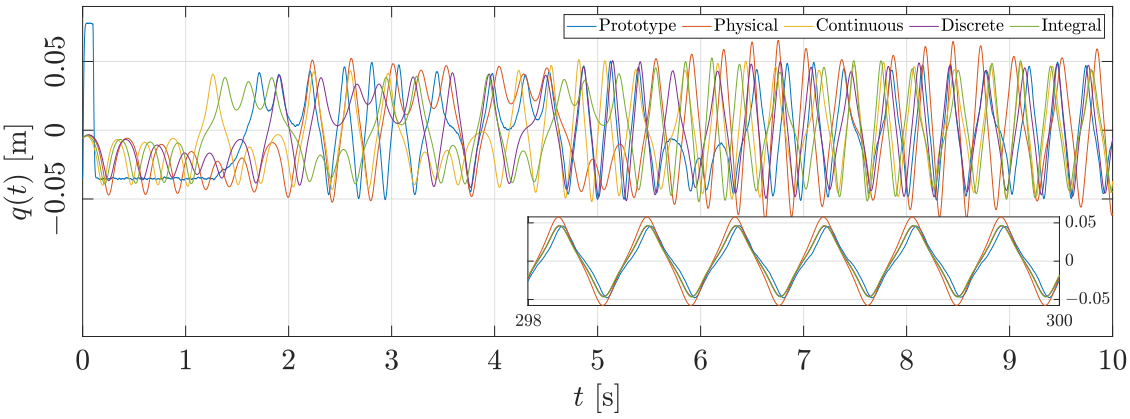

Figure 4.13: Interwell behavior validation.

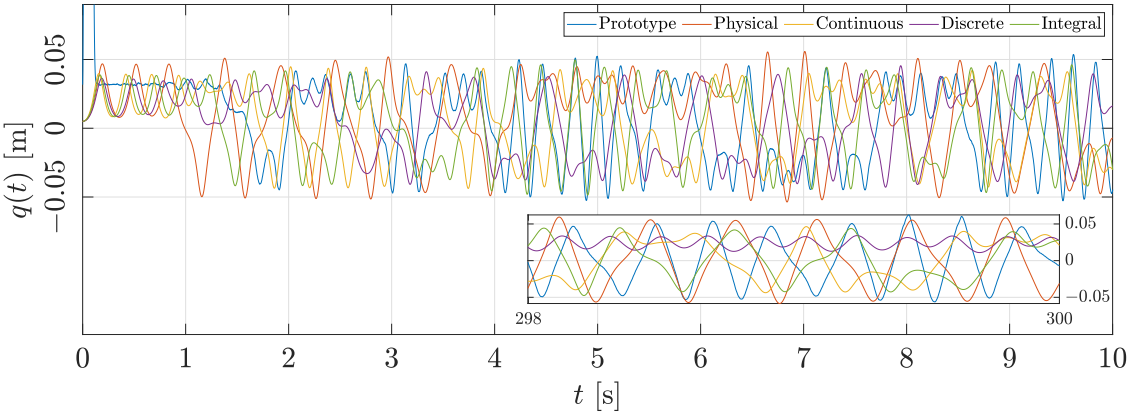

Figure 4.14: Chaos behavior validation.

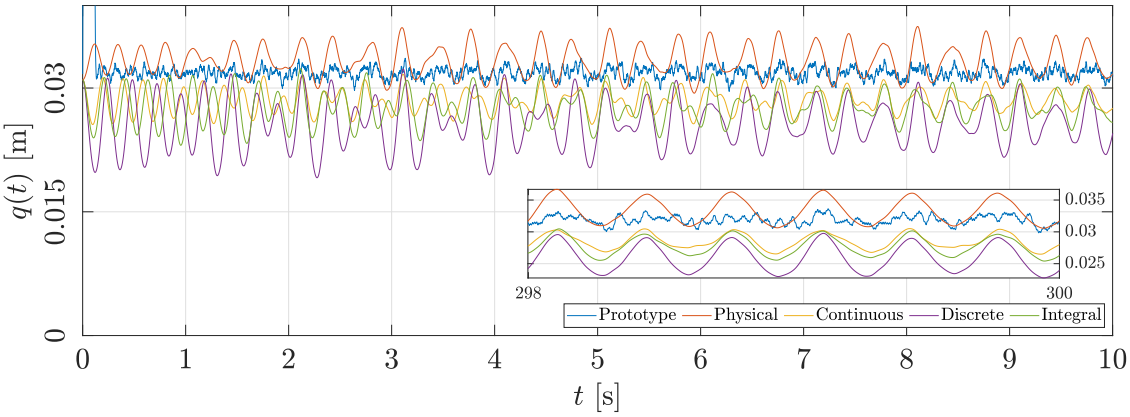

Figure 4.15: Intrawell behavior validation for the right equilibrium point.

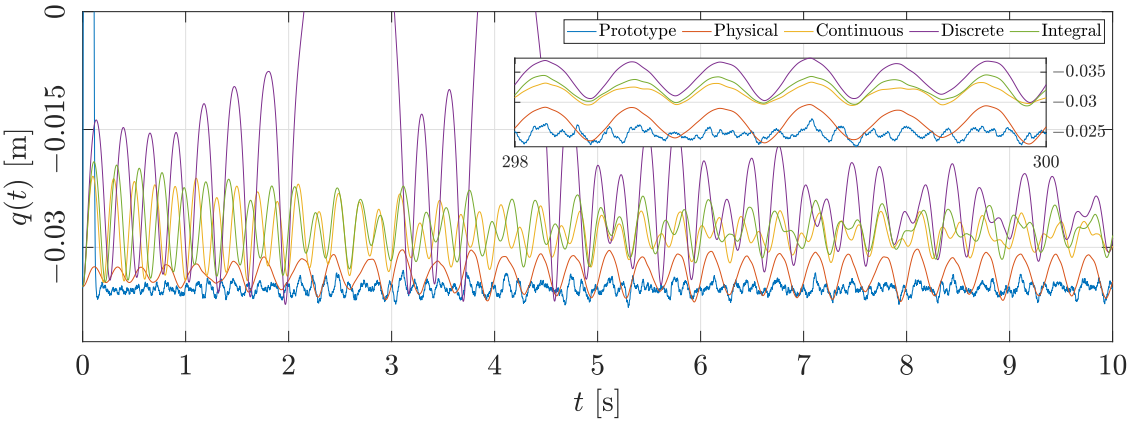

Figure 4.16: Intrawell behavior validation for the left equilibrium point.

Table 4.2: Parameters used for validation experiments.

Experiment	**Harmonic signal 1**		**Harmonic signal 2**		**Initial conditions**	
	Amplitude [cm]	Frequency [Hz]	Amplitude [cm]	Frequency [Hz]	$q_0(t)$ [m]	$\dot{q}_0(t)$ [m/s]
Interwell	0.4	3	0.1	2	0.005	0.1
Intrawell	0.3	3	0.05	2	0.033	0
Chaos	0.41	5.4	0.1	2	0.005	0

4.7 Conclusion

As was indicated at the beginning of the chapter, the identification of Duffing oscillators, also known as nonlinear oscillators, is the subject of multiple works, each of which offers solutions varying in complexity. Two approaches were offered in this instance to estimate the parameters of the prototype that was in use. First, parameters obtained with the second proposed method were sufficiently close to those obtained through analytical estimation using the presented formulas.

The use of the LMS method was useful to make a relatively fast identification of the system, but the results varied depending on the flitting method used for signal preprocessing. However, the validation shows that the estimated parameters are sufficiently close to the real values of the system, obtaining similar behaviors. It is important to take into account the use of Theorem 1 to ensure proper identification of the system, in addition to avoiding harmonic frequencies during this process because it can alter the results significantly.

CHAPTER 5

Non-linear Integral Extended State Observer

5.1 Introduction

Sometimes, in practice, there is no possibility of knowing the states of a system; that is, they cannot be measured. This may be due to economic or physical limitations related to the system or the inexistence of technology capable of performing such measurements. Due to this, state estimation methods have been studied and proposed. Estimating the unknown states of a system is essential for different activities or applications, decision-making, monitoring, or system control. One of the most widely used estimation methods is the state observer, since it can use information from sensors to approximate unknown values [68–70]. A correct selection and design of a state observer improve the performance of the applied controller [68, 70].

However, it is also necessary to consider that systems present uncertainties and disturbances that can be significant and also unknown. The estimation of uncertainties and disturbances is important since it is difficult to measure them [71]. It is possible to apply state and disturbance observers [72]. Because of this, the extended state observer (ESO) is a promising technology, as it can estimate both internal uncertainty and perturbations [72]. Basically, the ESO, in addition to its usefulness in estimating system states, takes uncertainties and disturbances as general uncertainties and encompasses them as a new extra state. The state observer can be considered an extended high-gain observer. Thus, the output of the extended observer and the total uncertainty of the system can be compensated by a controller, increasing its robustness [73]. In the literature, the use of an ESO is often presented in active disturbance rejection control (ADRC) [73]. For example, different applications and variations of ESO have been described and successfully implemented in systems such as flight control, chemical processes, robot control, or motion control [72, 74, 75].

However, despite the advantages of an extended state observer, it has limitations in the face of high-frequency noise in the measurements, and spikes occur during the transient period [73]. However, several solutions to these problems have been developed [73, 76].

For this project, a nonlinear integral extended state nonlinear extended state observer (NIESO) was proposed based on the observer designed and described in [70]. The position is obtained from the laser sensor measurements, and the parameters estimated during identification were used, so the system is partially known. Therefore, the proposed NIESO is intended to estimate the velocity,

the remaining parameters, and the unmodeled dynamics, i.e., the uncertainty, of the constructed Duffing oscillator. In the next section, the design of the proposed observer is presented.

5.2 Observer Design

Consider the Duffing-Holmes system (4.39). By defining $x_1 = q$ and $x_2 = \dot{q}$ its state-space form is

$$\begin{aligned} \dot{x}_1 &= x_2 \\ \dot{x}_2 &= \beta x_1 - \gamma x_1^3 - \alpha x_2 + \ddot{p} \end{aligned} \tag{5.1}$$

For this, it is considered that the position of the system is known, available to be measured using a laser distance sensor. Since in the previous chapter the identification of the system was made for the parameters α, β, and γ, their estimated values are known, so the previous equation can be rewritten as:

$$\begin{aligned} \dot{x}_1 &= x_2 \\ \dot{x}_2 &= \widehat{\beta} x_1 - \widehat{\gamma} x_1^3 - \widehat{\alpha} x_2 + (\beta - \widehat{\beta}) x_1 - (\gamma - \widehat{\gamma})\, x_1^3 \\ &\quad - (\alpha - \widehat{\alpha})\, x_2 + \chi + \ddot{p} \\ y &= x_1 + d \end{aligned} \tag{5.2}$$

where $\widehat{\alpha}$, $\widehat{\beta}$, and $\widehat{\gamma}$ are estimated values of the system parameters, χ is the unmodeled system dynamics, y is the position measurement output, and d is the bounded measurement noise from the position sensor.

Assumption 1. *The system parameters* $\boldsymbol{\theta} = [\alpha, \beta, \gamma]^{\mathrm{T}}$ *and its estimates* $\widehat{\boldsymbol{\theta}} = \left[\widehat{\alpha}, \widehat{\beta}, \widehat{\gamma}\right]^{\mathrm{T}}$ *satisfy the following conditions:*

$$\begin{aligned} \alpha, \widehat{\alpha} &\in \Omega_\alpha \triangleq \{\alpha : 0 < \alpha_{\min} < \alpha < \alpha_{\max}\} \\ \beta, \widehat{\beta} &\in \Omega_\beta \triangleq \{\beta : 0 < \beta_{\min} < \beta < \beta_{\max}\} \\ \gamma, \widehat{\gamma} &\in \Omega_\gamma \triangleq \{\gamma : 0 < \gamma_{\min} < \gamma < \gamma_{\max}\} \end{aligned} \tag{5.3}$$

hence, the corresponding parameter estimation errors $(\alpha - \widehat{\alpha})$, $(\beta - \widehat{\beta})$, *and* $(\gamma - \widehat{\gamma})$ *are constants and bounded.*

Assumption 2. *The unmodeled system dynamics* χ *is a smooth bounded function, hence* $\dot{\chi}$ *is also bounded.*

By defining the new extended states $x_0 = \int_0^t \dot{x}_1(\tau) d\tau$, $\psi(\mathbf{x}) = \widehat{\beta} x_1 - \widehat{\gamma} x_1^3 - \widehat{\alpha} x_2$, and $x_3 = \chi + (\beta - \widehat{\beta}) x_1 - (\gamma - \widehat{\gamma})\, x_1^3 = g$, their dynamics $\dot{x}_0 = x_1 + d$, and $\dot{x}_3 = \dot{g}$, (5.2) becomes:

$$\begin{aligned} \dot{x}_0 &= x_1 + d \\ \dot{x}_1 &= x_2 \\ \dot{x}_2 &= x_3 + \psi(\mathbf{x}) + \ddot{p} \\ \dot{x}_3 &= \dot{g} \end{aligned} \tag{5.4}$$

where the integral state x_0 is used to obtain robustness of the observer and controller designs toward the measurement noise d, and x_3 represents the uncertainty of the system. Consider the following nonlinear integral extended state observer (NIESO) design for the system represented in (5.4):

$$\begin{aligned}
\dot{\widehat{x}}_0 &= \widehat{x}_1 + 4\omega_o(x_0 - \widehat{x}_0) + d \\
\dot{\widehat{x}}_1 &= \widehat{x}_2 + 6\omega_o^2(x_0 - \widehat{x}_0) \\
\dot{\widehat{x}}_2 &= \widehat{x}_3 + \psi(\mathbf{x}) + \ddot{p} + 4\omega_o^3(x_0 - \widehat{x}_0) \\
\dot{\widehat{x}}_3 &= \omega_o^4(x_0 - \widehat{x}_0)
\end{aligned} \tag{5.5}$$

where ω_o is the only tuning parameter of the observer, it also represents the bandwidth of the observer.

5.3 States estimation convergence

Defining the state estimation error $e_i = x_i - \widehat{x}_i$, where $i = 0, ..., 3$, the error dynamics of the systems (5.4) and (5.5) becomes:

$$\begin{aligned}
\dot{e}_0 &= e_1 - 4\omega_o e_0 + d \\
\dot{e}_1 &= e_2 - 6\omega_o^2 e_0 \\
\dot{e}_2 &= e_3 + \psi(\mathbf{x}) - \psi(\widehat{\mathbf{x}}) - 4\omega_o^3 e_0 \\
\dot{e}_3 &= \dot{g} - \omega_o^4 e_0
\end{aligned} \tag{5.6}$$

Representing (5.6) in the following matrix form:

$$\dot{\mathbf{e}} = \mathbf{A}\mathbf{e}(t) + \mathbf{\Psi}(\mathbf{x}, \widehat{\mathbf{x}}, t) + \mathbf{\Delta}(t) \tag{5.7}$$

where $\mathbf{e} = [e_0, e_1, e_2, e_3]^{\mathrm{T}}$,

$$\mathbf{A} = \begin{bmatrix} -4\omega_o & 1 & 0 & 0 \\ -6\omega_o^2 & 0 & 1 & 0 \\ -4\omega_o^3 & 0 & 0 & 1 \\ -\omega_o^4 & 0 & 0 & 0 \end{bmatrix}, \ \mathbf{\Psi} = \begin{bmatrix} 0 \\ 0 \\ \psi(\mathbf{x}) - \psi(\widehat{\mathbf{x}}) \\ 0 \end{bmatrix}, \text{ and } \mathbf{\Delta} = \begin{bmatrix} d \\ 0 \\ 0 \\ \dot{g} \end{bmatrix}.$$

Proposition 1. *The boundedness of* $\mathbf{\Delta}$.

Proof. The boundedness of the signal $\mathbf{\Delta}$.

$$\dot{g} = \dot{\chi} + (\beta - \widehat{\beta}) - 3(\gamma - \widehat{\gamma})x_1^2 x_2 - (\alpha - \widehat{\alpha})\dot{x}_2 \tag{5.8}$$

is shown below:

- According to the Assumption 1, the terms $(\alpha - \widehat{\alpha})$, $(\beta - \widehat{\beta})$, and $(\gamma - \widehat{\gamma})$ are constants and bounded, and as per Assumption 2, $\dot{\chi}$ is bounded.
- Due to the system dynamics and structure, the states of (5.4), for $F = 0$ converge to any of the stable equilibrium points, and for $F \neq 0$ oscillates around any of the two stable equilibrium points $(x_1^*, x_2^*) = (\pm\sqrt{\beta/\gamma}, 0)$. Then the signals x_1, x_2, and $\dot{x}_2$, are bounded.

- The measurement noise d is a bounded signal related to sensor tolerance reported by the manufacturer [43] and physical limitations from the sensor and environment.

So, it can be concluded that $||\mathbf{\Delta}|| \leq \overline{\mathbf{\Delta}}$, in other words, $\mathbf{\Delta}$ is bounded. □

The characteristic polynomial of the matrix $\mathbf{A}$ is $p(s) = (s + \omega_o)^4$, and for any $\omega_o > 0$, $\mathbf{A}$ is Hurwitz, obtaining four repeated eigenvalues in $\lambda_{e_j} = -w_o < 0, j = 1, ..., 4$. The analysis of the convergence of the error of the a observer is based on the work done by the authors in [70] in which a NESO observer is studied for a bistable Duffing observer. In this case, use was made of the Gronwall-Bellman inequality described below.

Lemma 1 (Gronwall-Bellman Inequality). There are two continuous functions $h_1(t) : [0, t_1] \rightarrow \mathbb{R}$ and $h_2 : [0, t_1] \rightarrow \mathbb{R}_+$. For a continuous function $p_o(t) : [0, t_1] \rightarrow \mathbb{R}$ that satisfies:

$$p_o(t) \leq h_1(t) + \int_0^t h_2(\tau) p_o(\tau) d\tau, \quad 0 \leq t \leq t_1 \tag{5.9}$$

for the same interval $p(t)$ satisfies:

$$p_o(t) \leq h_1(t) + \int_0^t h_1(\tau) h_2(\tau) \exp^{\int_0^t h_2(s) ds} d\tau \tag{5.10}$$

Theorem 3. *The solution of the error dynamics* (5.3) *is:*

$$\mathbf{e}(t) = \exp^{\mathbf{A}t} \mathbf{e}(0) + \int_0^t \exp^{\mathbf{A}(t-\tau)} \mathbf{\Psi}(\mathbf{x}, \widehat{\mathbf{x}}, \tau) d\tau + \int_0^t \exp^{\mathbf{A}(t-\tau)} \mathbf{\Delta}(\tau) d\tau \tag{5.11}$$

Proof. Now, for every $\epsilon_o > 0$ and $\rho_o = (\omega_o - \epsilon_o) > 0$, there exist a constant $\mu > 0$ that satisfies:

$$|| \exp^{\mathbf{A}t} || \leq \mu \exp^{-\rho t}, \ t \geq 0 \tag{5.12}$$

Both vectors $\mathbf{\Psi}(\mathbf{x}, \widehat{\mathbf{x}}, t)$ and satisfies the Lipschitz condition as shown in [70], then, there exist an Lipschitz constant L that satisfies:

$$|\psi(\mathbf{x}) - \psi(\widehat{\mathbf{x}})| \leq L||\mathbf{x} - \widehat{\mathbf{x}}|| = L||\mathbf{e}(t)||, \ \forall \{\mathbf{x}, \widehat{\mathbf{x}}\} \subset \Omega_x, \tag{5.13}$$

where $\Omega_x = \{\mathbf{x}, \widehat{\mathbf{x}} \in \mathbb{R}^n : ||\mathbf{x}|| \leq r, \ ||\widehat{\mathbf{x}}|| \leq r\}$. This Lipschitz constant satisfies $L \leq \sup_{\mathbf{x} \in \Omega_x} \left\| \frac{\partial \psi(\mathbf{x})}{\partial \mathbf{x}} \right\|_\infty$, and leads to:

$$L = \beta_{\max} + 3\gamma_{\max} r^2 + \alpha_{\max} \tag{5.14}$$

Using (5.12) and (5.13), (5.11) satisfies:

$$\|\mathbf{e}(t)\| \leq \mu \exp^{-\rho t} \|\mathbf{e}(0)\| + \frac{\bar{\Delta}\mu}{\rho} \left(1 - \exp^{-\rho t}\right) \ + \exp^{-\rho t} \int_0^t \mu L \|\mathbf{e}(\tau)\| \exp^{\rho \tau} d\tau, \tag{5.15}$$

where $\bar{\Delta}$ is the upper bound value of the vector $\mathbf{\Delta}$, by multiplying (5.15) with $\exp^{\rho t}$ yields:

$$\|\mathbf{e}(t)\| \exp^{\rho t} \leq \mu \|\mathbf{e}(0)\| + \frac{\bar{\Delta}\mu}{\rho} \left(\exp^{\rho t} - 1\right) \ + \int_0^t \mu L \|\mathbf{e}(\tau)\| \exp^{\rho \tau} d\tau, \tag{5.16}$$

to apply Gronwall-Bellman inequality, the following are defined:

$$h_1(t) = \mu||\mathbf{e}(t)|| + \frac{\bar{\Delta}\mu}{\rho_o}\left(\exp^{\rho_o t} - 1\right), \quad h_2(t) = \mu L, \text{ and } \quad p_o(t) = ||\mathbf{e}(t)||\exp^{\rho_o t} \tag{5.17}$$

Replacing the expressions of (5.17) into (5.10) yields:

$$||\mathbf{e}||\exp^{\rho_o t} \leq \mu||\mathbf{e}(0)|| + \frac{\bar{\Delta}\mu}{\rho_o}(\exp^{\rho_o t} - 1) + \int_0^t \left[\mu||\mathbf{e}(0)|| + \frac{\bar{\Delta}\mu}{\rho_o}(\exp^{\rho_o t} - 1)\right] \mu L \exp^{\mu L(t-\tau)}\, d\tau \tag{5.18}$$

Splitting the integral:

$$\begin{aligned} ||\mathbf{e}(t)||\exp^{\rho_o t} \leq{}& \mu||\mathbf{e}(0)|| + \frac{\bar{\Delta}\mu}{\rho_o}(\exp^{\rho_o t} - 1) + \int_0^t \mu^2 L||\mathbf{e}(0)||\exp^{\mu L t}\exp^{-\mu L\tau}\, d\tau \\ &+ \frac{\bar{\Delta}\mu}{\rho_o}\left[\int_0^t \mu L \exp^{\mu L(t-\tau)}\exp^{\rho_o t}\, d\tau - \int_0^t \mu L \exp^{\mu L(t-\tau)}\, d\tau\right] \end{aligned} \tag{5.19}$$

Simplifying after integration the following expression is obtained:

$$||\mathbf{e}(t)||\exp^{\rho_o t} \leq \mu||\mathbf{e}(0)||\exp^{\mu L t} + \Lambda(\exp^{\rho_o t} - \exp^{\mu L t}), \tag{5.20}$$

where:

$$\Lambda = \frac{\bar{\Delta}\mu}{\rho_o}\left(1 - \frac{\mu L}{(\rho_o - \mu L)}\right), \tag{5.21}$$

which is a positive constant. By multiplying (5.21) with $\exp^{-\rho_o t}$ it yields:

$$||\mathbf{e}(t)|| \leq \exp^{(\mu L - \rho_o)t}(\mu||\mathbf{e}(0)|| - \Lambda) + \Lambda, \ t \geq 0 \tag{5.22}$$

Now, by choosing $\rho > \mu L$, the estimation error $\mathbf{e}(t)$ is bounded and the estimated state vector $\widehat{\mathbf{x}}$ converges bounded inside a ball with radius Λ around the system state vector $\mathbf{x}$. □

Notice, first, that $0 < (\omega_o - \epsilon) < \mu L$, second, that the bigger ω_o gets, yields a faster convergence and a smaller radius Λ [70].

5.4 Poincare map

Using the time series of their states, nonlinear systems' dynamics can be identified and examined using Poincare maps. The geometry and topology of the data serve as the foundation for the analysis of these maps. Trajectories that represent the entirety of the dynamics of a system in a stable regime are known as attractors [77]. These trajectories can present specific structures of the system.

To construct these maps, a section surface that cuts the trajectory under study must be selected, and the points at which it passes through said section will be recorded. This process can be done with different trajectories, and depending on the behavior of the system, specific patterns will be generated. For example, a limit cycle is a trajectory that will always pass through the same point in the section [78, 79].

5.5 Experimental results

The experimentation process followed a similar protocol to the experimental validation protocol outlined in Section 4.6.5. The parameters estimated in Section 4.6.3 were used to compare the various NIESO observers produced with those parameters. The parameters used for the experiments are displayed in Table 4.1 to obtain the different behaviors of the oscillator.

Since the NIESO observer uses the values of the system parameters, experiments were carried out using the different estimated values for each parameter in such a way that the results could be compared and the most accurate observer could be used. Figures 5.1 a) to d) are the results of the observers' experiment for each behavior of the system. In addition, the table 5.1 shows the RMS error for each experiment. The observer that presents the best results compared to the rest is the one that uses the parameters estimated with the discrete filters. From now on, when the observer is used with NIESO in simulations and experiments, we will talk about the one that uses the values obtained with the discrete filters.

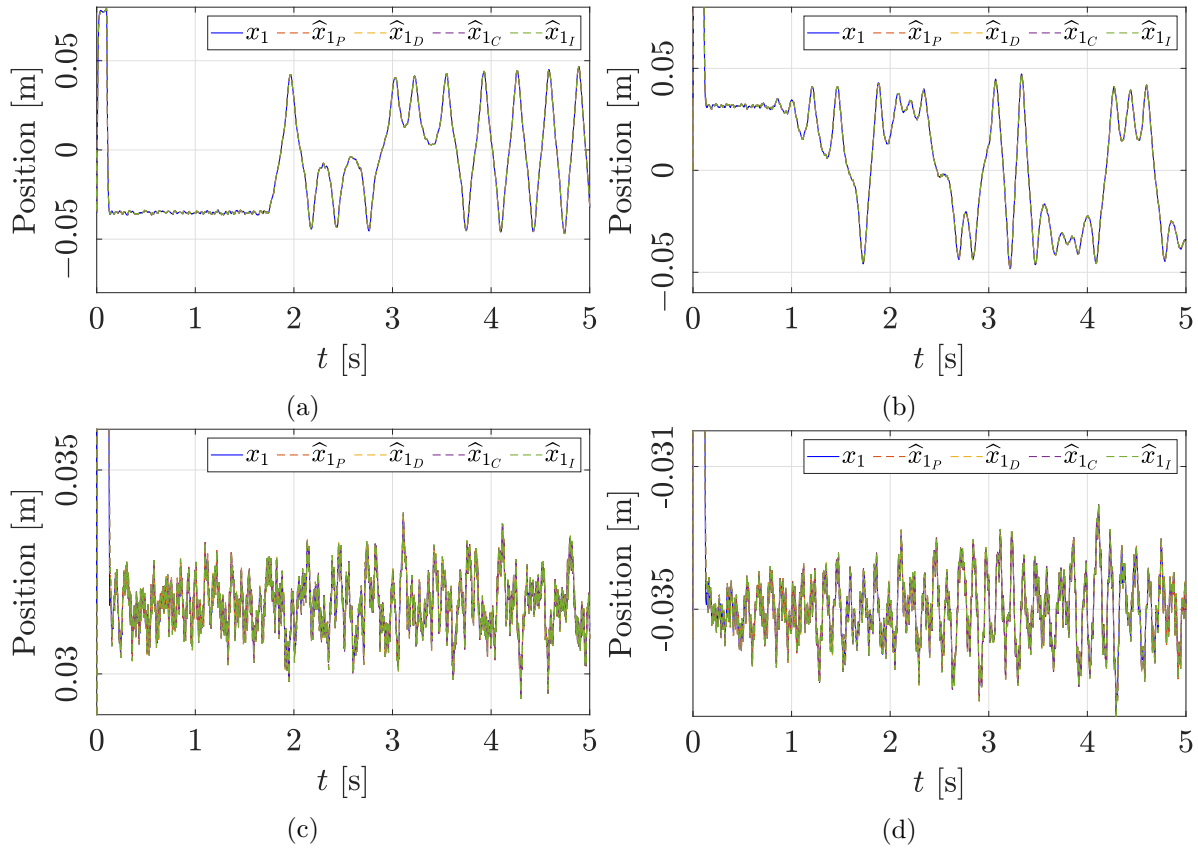

Figure 5.1: Comparison of the x_1 estimation performance of the NIESO observer with each group of parameters estimated in Chapter 4, where the subscripts P, D, C, and I refer to Physical, Discrete, Continuous and Integral, referring to the filtering or parameter estimation methods.. a) Interwell Behavior. b) Chaotic behavior. c) Intrawell behavior left equilibrium point. d) Intrawell behavior of right equilibrium point.

Experiments were conducted with the prototype for each of the dynamic behaviors of the Duffing

Table 5.1: Root mean square error.

Method	**RMSE** [m]			
	Interwell	Chaos	Right Intrawell	Left Intrawell
Physical	1.8968×10^{-4}	1.9960×10^{-4}	2.2157×10^{-4}	2.1919×10^{-4}
Integral	1.8818×10^{-4}	2.0677×10^{-4}	2.3594×10^{-4}	2.1829×10^{-4}
Continuous	1.8798×10^{-4}	2.098×10^{-4}	2.4135×10^{-4}	2.1815×10^{-4}
Discrete	1.8830×10^{-4}	2.0442×10^{-4}	2.3179×10^{-4}	2.1836×10^{-4}

oscillator to verify that the designed observer was functioning as intended. The performance of the Linear Integral Extended State Observer (LIESO), whose representation in the state space is (5.23), was also compared to that of the NIESO observer (5.5).

$$\begin{aligned}
\dot{\widehat{x}}_0 &= \widehat{x}_1 + 4\omega_o(x_0 - \widehat{x}_0) + d \\
\dot{\widehat{x}}_1 &= \widehat{x}_2 + 6\omega_o^2(x_0 - \widehat{x}_0) \\
\dot{\widehat{x}}_2 &= \widehat{x}_3 + \ddot{p} + 4\omega_o^3(x_0 - \widehat{x}_0) \\
\dot{\widehat{x}}_3 &= \omega_o^4(x_0 - \widehat{x}_0).
\end{aligned} \tag{5.23}$$

All observers used identical position and acceleration data, making comparisons simple. The parameters used in each experiment are compiled in Table 5.2. Various experiments were conducted for every oscillator behavior. The results obtained for a duration of 10 seconds are displayed in the figures. Table 5.3 displays the root mean square error (RMSE). It is evident that the nonlinear integral observer with extended states exhibits a marginally smaller error than the other observer under study. This error is small enough to justify the use of the observer in the design of the oscillator controller. However, since the estimation error is very small, the use of any of the observers is acceptable here, and they are precise enough to be able to apply any of them both for the controller and in different situations.

Table 5.2: Parameters used for validation experiments.

	System behavior			
	Interwell	Chaos	Right Intrawell	Left Intrawell
Amplitude [cm]	0.4	0.41	0.2	0.2
Frequency [Hz]	3	5.4	4	4
$x_1(0)$ [cm]	-3.17	3.1	3.52	-3.2
$x_2(0)$ [m/s]	0	0	0	0

The state observer experiments were conducted using a methodology akin to that employed in the preceding chapter for the validation of the estimated parameters presented in Section 4.6.5. Table 4.2 displays the experiment parameters that were used to produce the various oscillator behaviors. The position of the system was measured using the HG-C1400-P laser sensor, which has a response time of 1.5 [ms]. This measurement is used to compare the estimate $\widehat{x}_1$ of the state x_1 of the state observers. One observer was implemented for each set of parameters obtained

in the identification process, which are compiled in Table 4.1, because the NIESO observer uses the estimated parameters of the system. For each observer, the same gain value ($\omega_0 = 500$) was utilized. The comparison between the estimated and measured values of the position is displayed in Figures 5.2 through 5.4. The four plots demonstrate how accurate the estimate x_1 is—so accurate that there is no discernible difference between the measurements and the output of the observer.

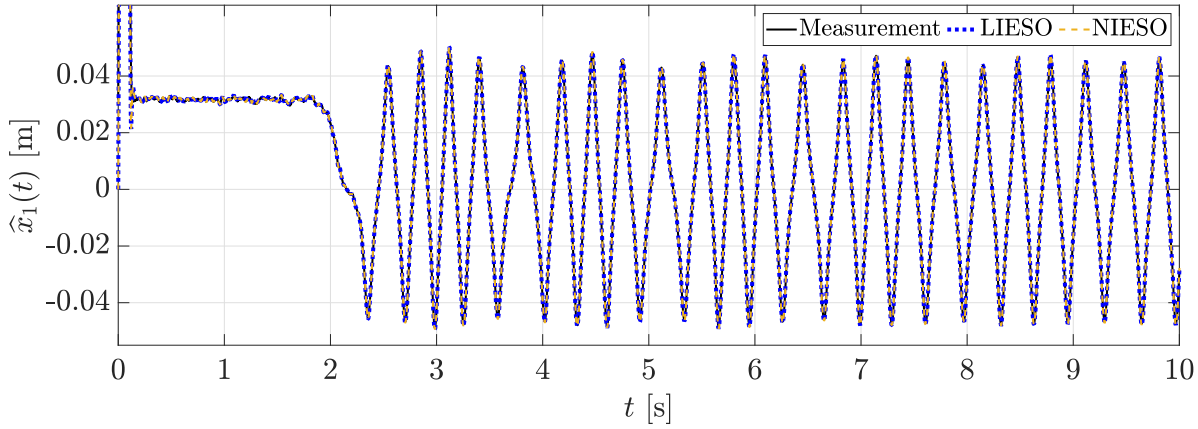

Figure 5.2: Interwell estimated and real position.

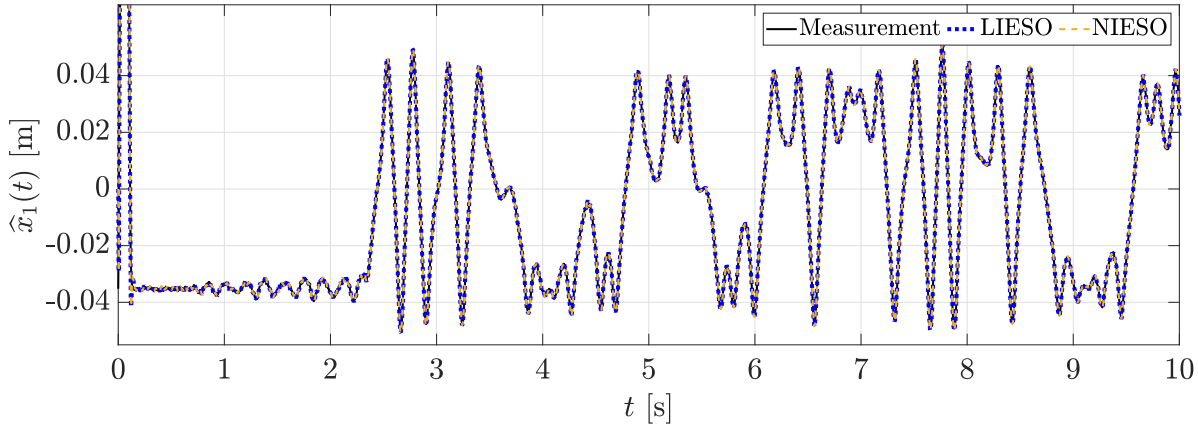

Figure 5.3: Chaos estimated and real position.

Given that measurements cannot determine the velocity of the beam $\dot{q}(t)$, an estimate of the velocity was obtained by applying the derivative filter (5.24) to the measured position. The output of F_{der} was compared with the estimated velocity of the observer $\widehat{\dot{q}}(t)$. The results of the estimation of $\dot{q}(t)$ are displayed in Figures 5.5 to 5.7; it is noted that the estimates are fairly similar in these, even when considering the output of the (5.24) filter. It is important to remember that the filter does not attenuate the high-frequency noise because, in contrast to the observer, it functions as a high-pass filter.

$$F_{der} = \frac{500s}{s + 500} \tag{5.24}$$

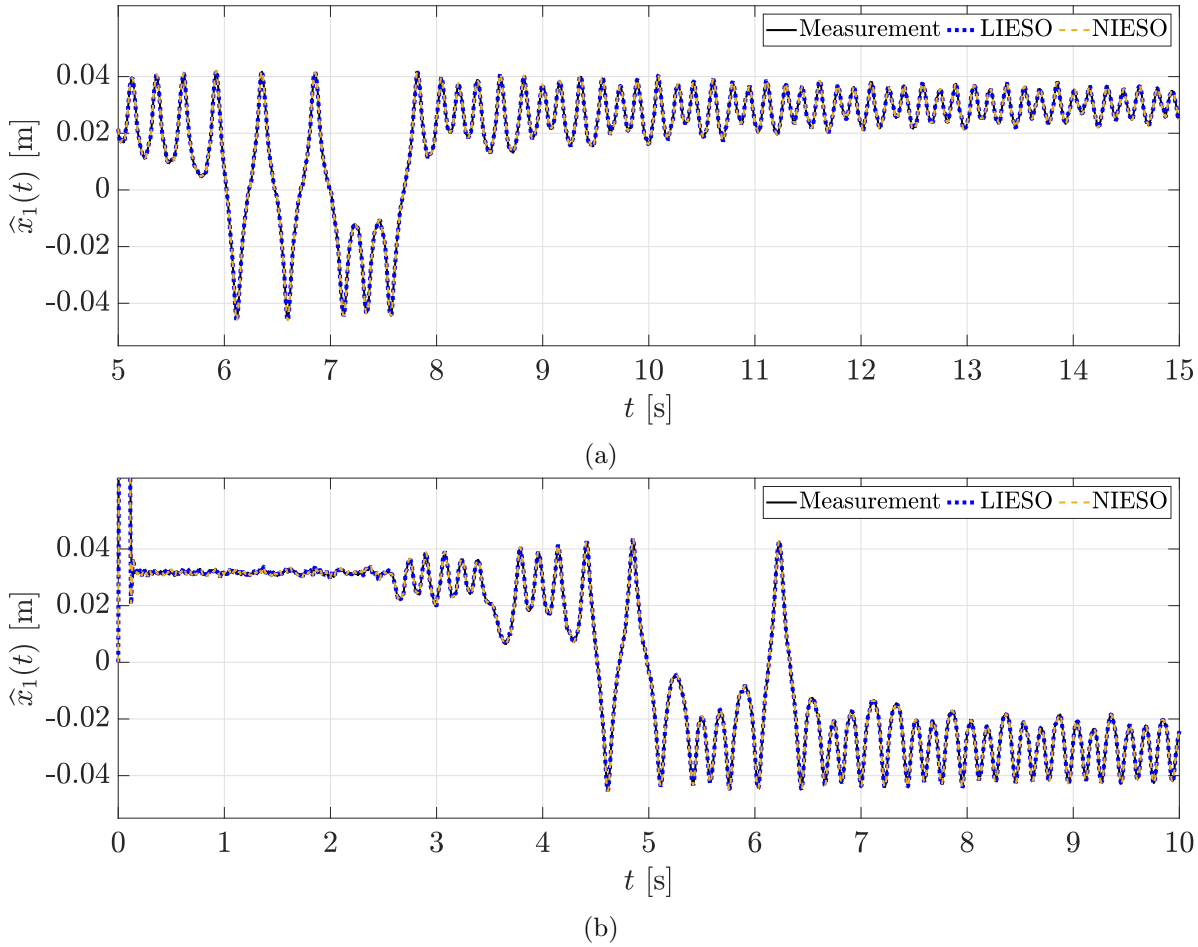

Figure 5.4: Intrawell estimated and real position. a) Right equilibrium point. b) Left equilibrium point.

Regression analysis is a useful tool for assessing how well a regression model fits the actual data set by enabling one to comprehend and measure the relationship between the predicted values of the model and the actual values obtained from a data set. The standard deviation of the prediction or estimation error is known as the root mean square error (RMSE); Put another way, it can be thought of as the average error of the model predictions compared to the actual data. As a result, the better the estimate fit, the lower the RMSE value. The following formula can be used to determine the RMSE:

$$\text{RMSE} = \sqrt{\frac{1}{N}\sum_{i=1}^{N}[x_1(i) - \widehat{x}_1(i)]^2} \tag{5.25}$$

where N is the total number of samples.

The RMSE results for each observer used for experimentation are found in Table 5.3, here it should be noted that both for the studied observers, regardless of the oscillator behavior, have very similar, and small, RMSE values. Just as in Figures 5.5 to 5.7, one has an accurate estimate.

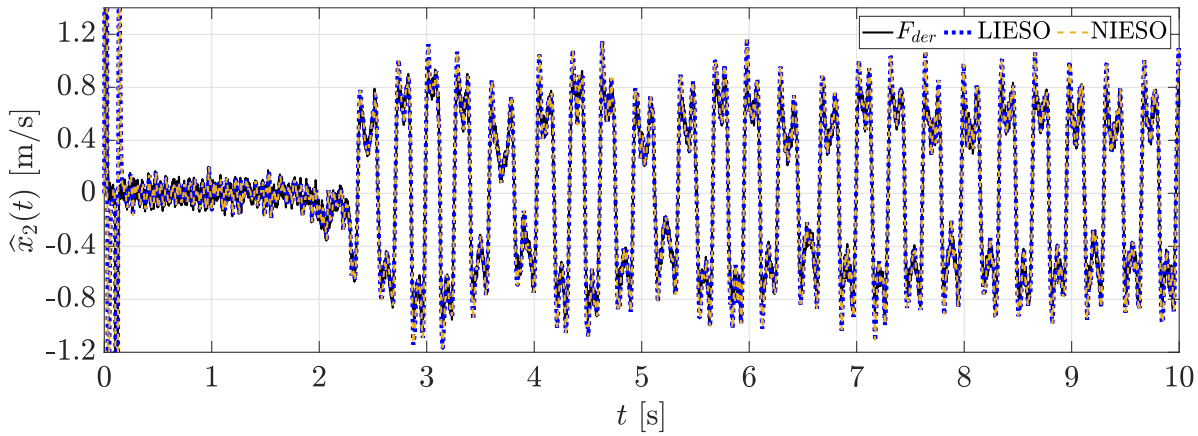

Figure 5.5: Interwell estimated velocity.

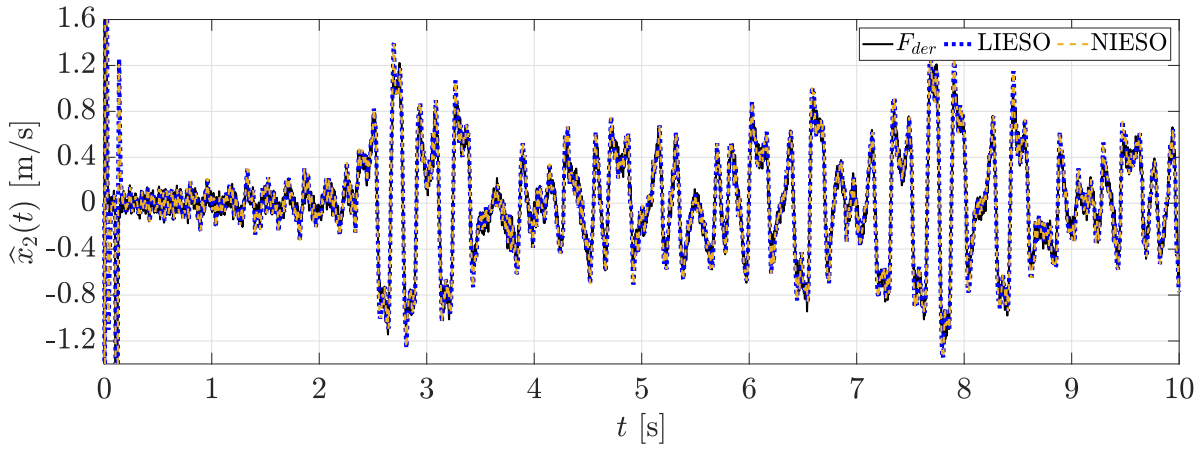

Figure 5.6: Chaos estimated velocity.

Table 5.3: Root mean square error of position in meters.

Observer	**RMSE**			
	Interwell	Chaos	Right Intrawell	Left Intrawell
LIESO	5.4642×10^{-4}	4.7643×10^{-4}	4.3348×10^{-4}	4.8946×10^{-4}
NIESO	5.4322×10^{-4}	4.7443×10^{-4}	4.317×10^{-4}	4.865×10^{-4}

Finally, figures 5.8 a) to c) show the Poincare maps of the chaotic behavior for a sine excitation given by $v(t) = (0.51/100)\sin(8 * 2\pi t)$. In all figures, the characteristic shape obtained for the chaotic behavior in the Duffing oscillator is obtained. The experiment was repeated three times, obtaining very similar results.

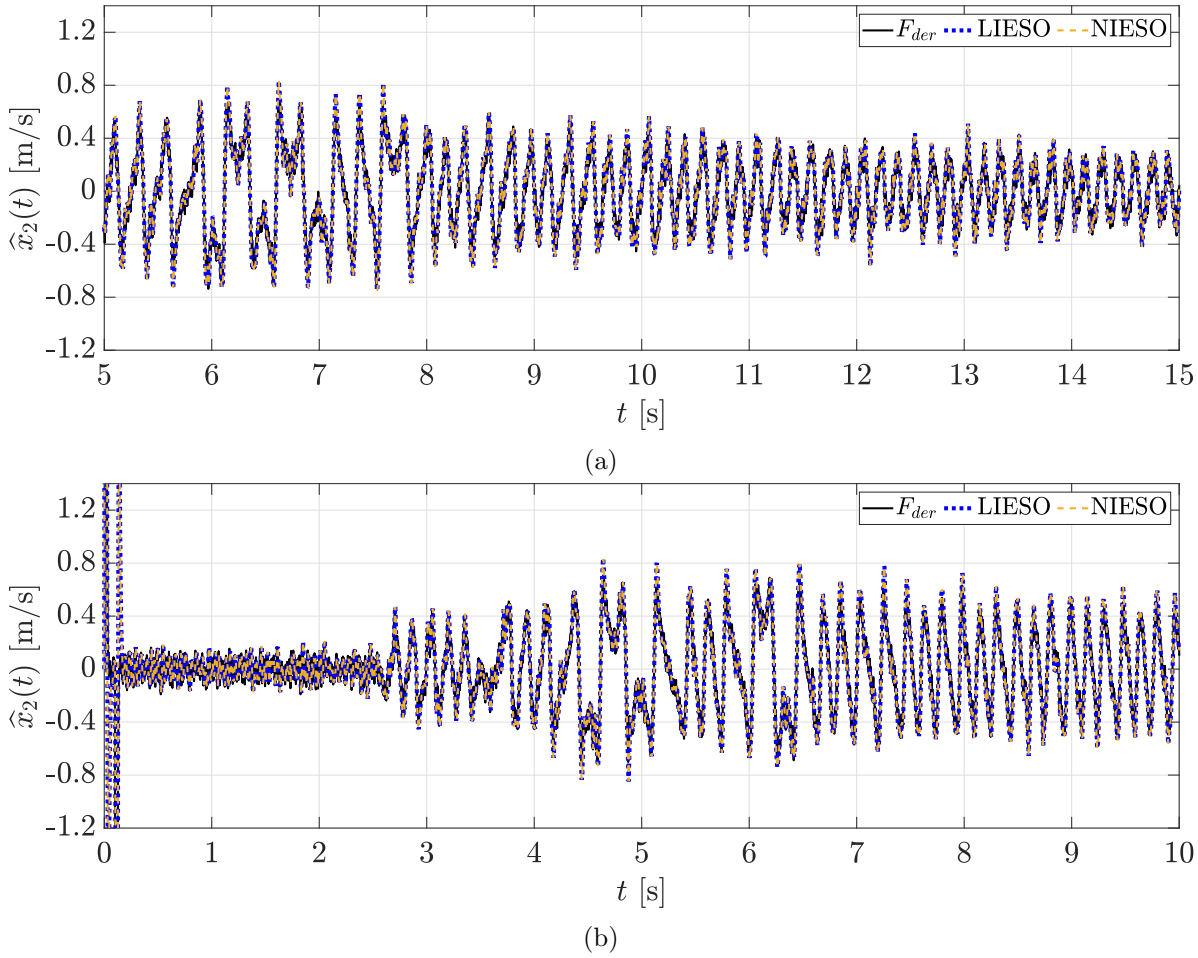

Figure 5.7: Intrawell estimated velocity. a) Right equilibrium point. b) Left equilibrium point.

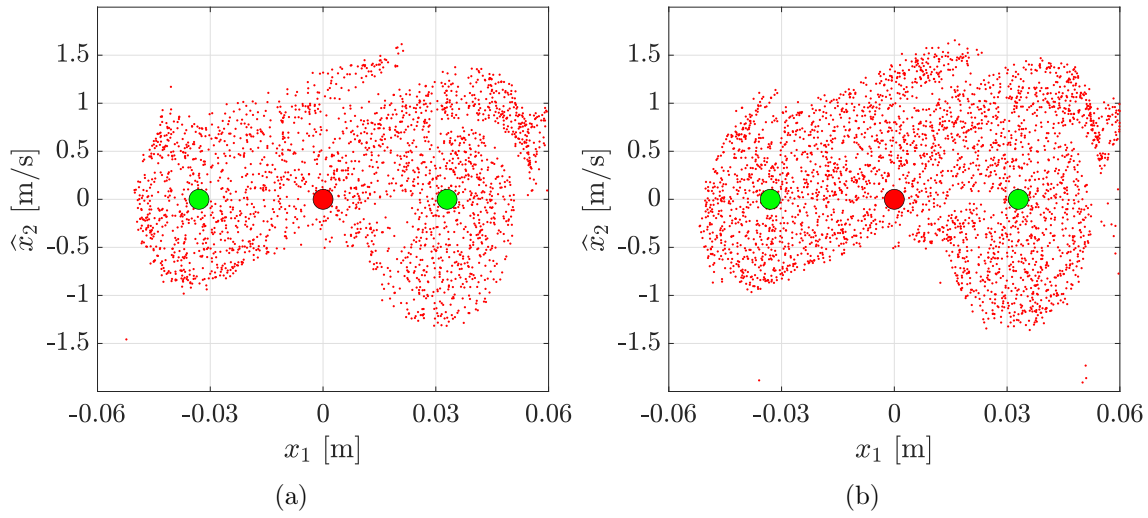

Figure 5.8: Poincare map of chaotic behavior experimental results.

5.6 Conclusions

The stability of the observer was demonstrated by the Gronwall-Bellman inequality, thus ensuring its correct functioning. The use of a large gain allowed rapid convergence and high accuracy in estimating system states. For the experiment, a large gain $w_o = 500$ was used; both observers have errors less than 0.1 [mm], that is, less than 0.1×10^{-3} [m]. Since the controller uses the states x_0 and the nonlinearities of the system as presented in Chapter 6, the use of the NIESO observer was chosen.

There was a comparison between the performance of NIESO and LIESO observers. Comparing the two, significant variations are observed in the estimation of the states x_1, x_2, and x_3. On the other hand, the NIESO-type observer has a lower RMSE error and allows the global uncertainty of the system to be estimated. For the controller used in the next chapter, it is useful to use the extended states $\widehat{x}_0$ and $\widehat{x}_3$.

Finally, the Poincaré maps in Figures 5.8 a) to c) were produced using the state observer estimates. Since the shapes formed in all three cases are indicative of chaos in the Duffing bistable oscillator, it was possible to confirm that the built prototype, shown in Chapter 3, was designed, modeled and operated correctly.

CHAPTER 6

Observer based controller

6.1 Introduction

The last ten years have seen a rise in the amount of research on chaotic system control, particularly on nonlinear oscillators like the Duffing oscillator. The fact that these systems are highly dependent on the starting conditions and can be significantly altered by small control actions is one of the factors that makes them interesting to control [80]. Additionally, the benefits of using chaotic systems have been investigated recently in a variety of fields, including flexible robotics, quantum transition, sensor development, precision measurements, energy harvesting, system chaos, signal amplification and detection, and energy harvesting [13, 15, 81–83].

Since it was presented, multiple strategies for controlling the Duffing oscillator have been studied, to a large extent. Thanks to the increasing computing power of current equipment, the viability and performance of the proposed controllers have been demonstrated numerically and analytically [80–88]. Multiple studies focused on the control of the Duffing oscillator have been carried out; for example, Sifakis and Elliott [80] propose four different control strategies: continuous delayed feedback (CDF), occasional proportional feedback, Ott, Grebogi, and Yorke (OGY), which were validated using numerical simulations. Cunli Wu [84] presented the simulation of the implementation of a feedback-free noise phase addition controller for the control of the chaotic behavior of a Duffing oscillator. While simulations check the feasibility of using a robust slider mode controller and a class of optimal polynomial controller to expand the stability region of the system [83] In [81], a phase controller was applied in its experiments to estimate the parameters of the experimental platform used. Bedri Bahtiyar [87] used a predictive fuzzy controller to classify systems using the Duffing oscillator as a reference. Huang and Ji [82] applied a vibration controller to coupled Duffing oscillators representing flexible junction manipulators using a Quanser® experimental platform. In other cases, what is sought is to suppress the effect of chaos. Vinícius Piccirillo [88] numerically verified the use of a linear vibration absorber to suppress the chaotic behavior of a duffing oscillator.

Harb *et al.* [86] presented and validated the use of a recursive back-stepping controller through simulations for the control of duffing oscillators, concluding that robustness can be added to the controller by using state or parameter estimators to reduce the effect of model uncertainties. For example, Yao *et al.* [85] used an Extended State Observer (ESO) to mitigate the effect of structured and unstructured uncertainties in the control of DC motors together with an Adaptive Robust Controller. For the design of the controller implemented in this project, tools such as those presented in the two aforementioned works were used. Here, a controller based on a non-linear integral

extended state observer (NIESO) was designed using the backtracking technique.

6.2 Control Objective

The objective is to design a controller such that the system position $x_1 \to x_d$, i.e., the controller design is focused on tracking a desired trajectory x_d given by the non-linear reference model (6.1), where the desired position is a smooth bounded function.

$$\begin{aligned} \dot{x}_d &= \frac{d}{dt} x_d \\ \ddot{x}_d &= \widehat{\beta} x_d - \widehat{\gamma} x_d^3 - \widehat{\alpha} \dot{x}_d + \ddot{p} \end{aligned} \tag{6.1}$$

For the control of the system studied in this thesis (5.1), the back-stepping technique is used to obtain a stable closed-loop system with the desired dynamics. To compensate for the present uncertainty, the designed controller will be based on the estimated states of the observer $\widehat{x}_1, \widehat{x}_3$ and $\widehat{x}_3$. The back-stepping control technique is based on a recursive design process that, in summary, disassembles the nonlinear control problem into simpler control elements, focusing on achieving global asymptotic stability of feedback systems [89, 90].

6.3 Observer-based Controller Design

The back-stepping technique was applied to design the controller for the system (5.1). For that, let us define the following new state variables

$$z_1 = \widehat{x}_1 - x_d \tag{6.2}$$

$$z_2 = \widehat{x}_2 - \nu \tag{6.3}$$

where z_1 is the tracking errors, and ν is a virtual control input that will be chosen later.

The dynamics of z_1 is calculated as

$$\dot{z_1} = \dot{\widehat{x}}_1 - \dot{x}_d = z_2 + \nu + 6\omega_o^2 e_0 - \dot{x}_d, \tag{6.4}$$

choosing ν as follows

$$\nu = \dot{x}_d - k_1 z_1 - 6\omega_o^2 e_0, \tag{6.5}$$

where k_1 is one control gain, the equation (6.5) becomes

$$\dot{z}_1 = -k_1 z_1 + z_2. \tag{6.6}$$

The dynamics of z_2 is given by

$$\begin{aligned} \dot{z}_2 =& \dot{\widehat{x}}_2 - \dot{\nu} \\ =& \widehat{x}_3 + \psi(\widehat{\mathbf{x}}) + u + 4\omega_o^3 e_0 - \dot{\nu} \end{aligned} \tag{6.7}$$

where

$$\begin{aligned} \dot{\nu} =& \ddot{x}_d - k_1 \dot{z}_1 - 6\omega_o^2 \dot{e}_0 \\ =& \ddot{x}_d - k_1 \dot{z}_1 - 24\omega_o^3 e_0 - 6\omega_o^2 (e_1 + d). \end{aligned} \tag{6.8}$$

Since $e_1 = x_1 - \widehat{x}_1 = (y - d) - \widehat{x}_1$, then

$$\dot{\nu} = \ddot{x}_d - k_1 \dot{z}_1 - 24\omega_o^3 e_0 - 6\omega_o^2 (y - \widehat{x}_1) \tag{6.9}$$

where all the signals are available. Finally, the proposed control law u is:

$$u = -z_1 - k_2 z_2 - \widehat{x}_3 - \psi(\widehat{\mathbf{x}}) - 4\omega_o^3 e_0 + \dot{\nu}, \tag{6.10}$$

it yields:

$$\dot{z}_2 = -z_1 - k_2 z_2 \tag{6.11}$$

The closed-loop dynamics of the system consisting of (6.6) and (6.11) is expressed as the z-system is an LTI system:

$$\frac{d}{dt} \begin{bmatrix} z_1 \\ z_2 \end{bmatrix} = \begin{bmatrix} -k_1 & 1 \\ -1 & -k_2 \end{bmatrix} \begin{bmatrix} z_1 \\ z_2 \end{bmatrix} \tag{6.12}$$

which is Hurwitz i.e. stable for positive controller gains k_1 and k_2. Then the position tracking error goes to zero asymptotically, hence the z_1 is bounded and depends on the observer estimation error.

6.4 Controlling Duffing oscillator via shake table

The system operates, as described in Chapter 4, by feeding a reference position signal v_d to the shaking table and feeding the Duffing oscillator with the acceleration $\ddot{v}$ caused by the table movement. In actual use, the table's position is managed independently of its acceleration. In other words, the vibrating table system, depicted in Figure 6.1, is in a closed loop.

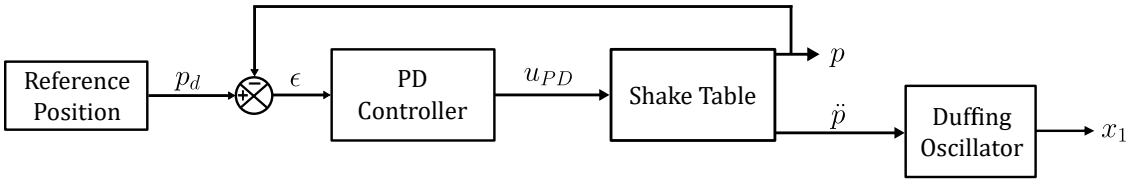

Figure 6.1: General open-loop operation of the prototype system.

The control signal (6.10) is in terms of acceleration; however, in this case, it is necessary to generate the control signal (6.10) in such a way that it is in terms of the position of the table [91]. To do this, consider that the desired position of the table is given by

$$p_d = \int_0^t \int_0^{\tau_1} u(\tau_2) d\tau_2 d\tau_1 \tag{6.13}$$

Figure 6.2 is the block diagram representation of the previous expression, so that it can be implemented in the Simulink® environment. However, the drawback of using pure integrators, $F_{ii} = 1/s$, to obtain $\dot{x}_d$ and x_d is that the low frequency components of u will be amplified, which will generate a signal x_d that can be increasing. This phenomenon is known as drift and can cause x_d to take values larger than the allowed limits [92, 93]. To avoid this problem, the following integrating filter (6.14) is used, called drift-free-integrator, which does not integrate very low frequency components or offsets, thus preventing x_d from taking on high values.

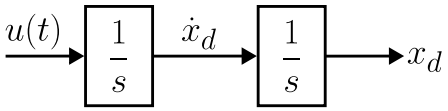

Figure 6.2: Control signal double integration block diagram.

$$F_{dfi} = \frac{s^2}{s^3 + 10.77s^2 + 10.56s} \tag{6.14}$$

Figure 6.3 shows the Bode plot of the integrating filter, which is compared to the Bode plot of a pure integrator. Note that the integrating filter attenuates low-frequency components, lower than $\omega = 10$ [rad/s] or $f = 1.59$ [Hz]. For frequencies greater than this value, F_{dfi} behaves as a pure integrator.

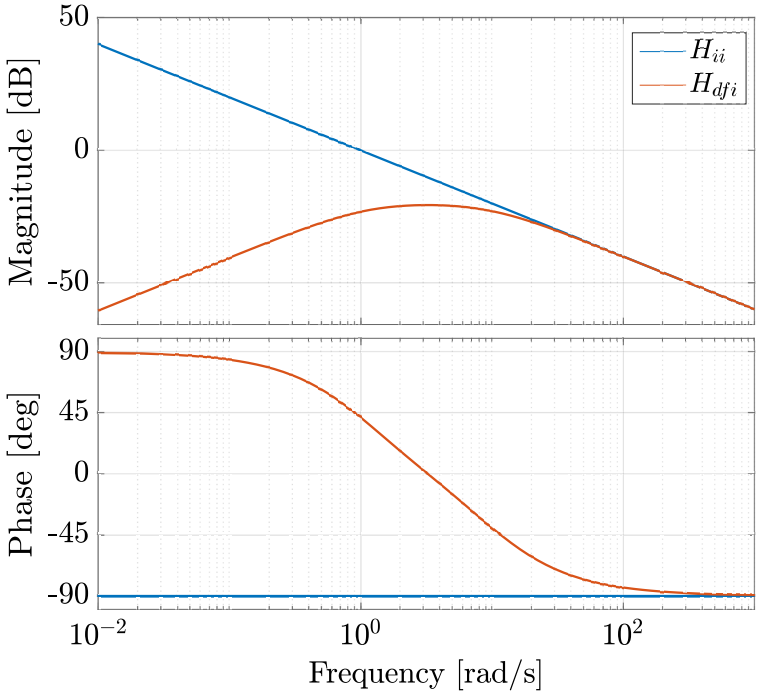

Figure 6.3: Bode diagrams of drift-free-integrator H_{nd} and pure integrator H_p.

The diagram in Figure 6.4 can be used to resume the implementation of the controller. It should be noted that the controller uses the reference model states x_d, $\dot{x}_d$, and $\ddot{x}_d$, and that $\ddot{p}$ should equal u. Additionally, the controller makes use of the estimated states $\widehat{\mathbf{x}}$, the error e_0, and the controller itself, as well as the vibration table designed by the equipment supplier Quanser®. Finally, the good performance of the shake table $p \approx p_d$ implies $\ddot{p} \approx u$.

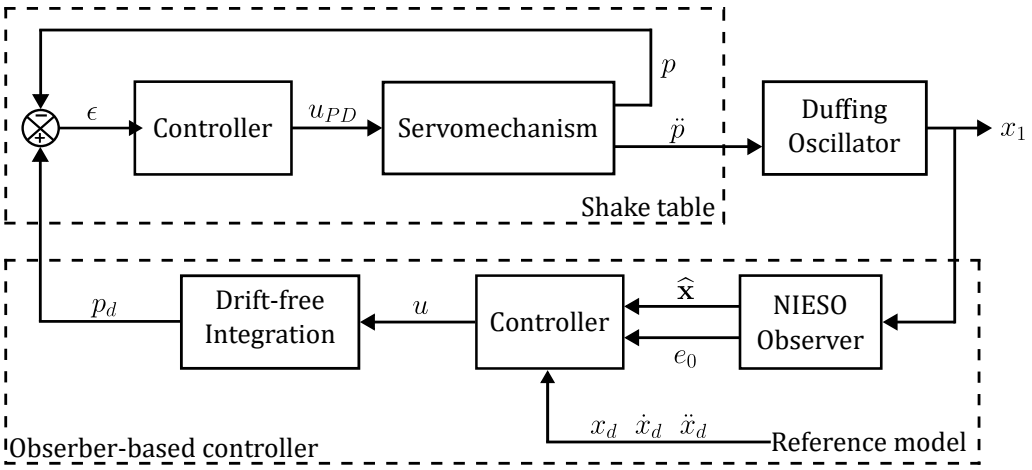

Figure 6.4: Implementation of the proposed control scheme.

6.5 Results

The findings from the controller simulations and the experiments conducted on the experimental system are shown in this section. The simulations and their parameters are displayed first, followed by the experiments that were conducted and their parameters.

6.5.1 Simulations

This section shows the results of the simulations of the controller applied to each of the behaviors of the Duffing oscillator. The parameters used for the reference model and the state observer are the parameters estimated using the integral filters, and for the simulation of the real system, the values obtained with the discrete filters were used from Table 4.1. The observer gain is $\omega_o = 500$, and the controller gains used are $k_1 = 600$ and $k_2 = 250$. The initial position of the simulated real system depends on its behavior as well as the input force. $\ddot{v}$, for interwell $x_1(0) = 0.006$ [m], and $\ddot{p} = 1.7765\sin(6\pi t)$; for left intrawell $x_1(0) = 0.031$ [m], and $\ddot{p} = 1.0659\sin(6\pi t)$; for right intrawell $x_1(0) = 0.032$ [m], and $\ddot{p} = 1.0659\sin(6\pi t)$; and for chaotic $x_1(0) = 0.035$ [m], and $\ddot{p} = 4.9288\sin(5.1\pi t)$.

In the simulations, the controller shows correct tracking of the reference trajectory, obtaining small z_1 values. Figure 6.5 (a) shows the tracking of the position in the interwell behavior, in which it even manages to follow the reference in the transient prior to reaching the desired behavior. Figure 6.5 (b) shows the error z_1 obtained.Figures 6.6 (a) and 6.7 (a) show the simulation of the controller for intrawell simulations. For either experiment, the control action produces an acceptable tracking position. It is difficult to tell the difference between x_d and x_1. The resulting error is shown in Figures 6.6 (b) and 6.7 (b), where the error amplitude is less than 0.6×10^{-4} [m]. After validating the correct operation of the controller through the simulations carried out, it was possible to move on to experimental validation using the built prototype. The results of the experimentation are presented below.

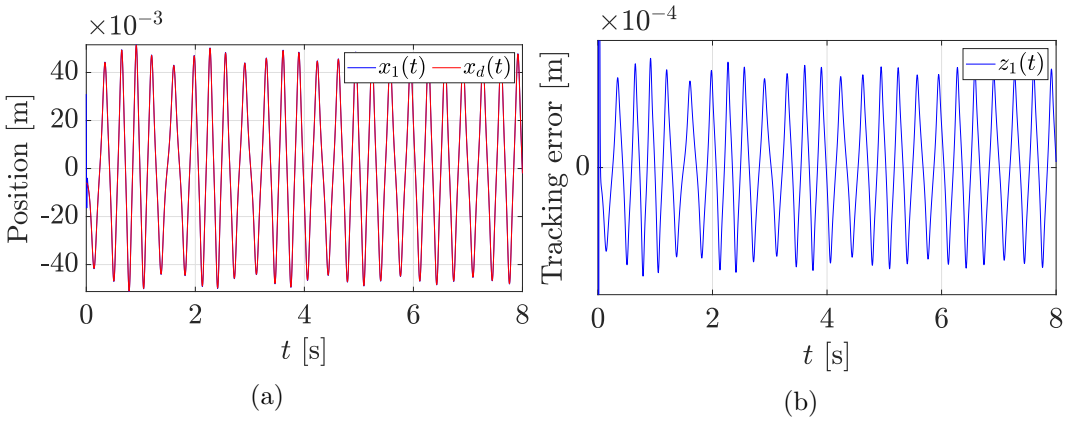

Figure 6.5: Interwell controller position tracking simulation result. (a) Position tracking. (b) Position tracking error z_1.

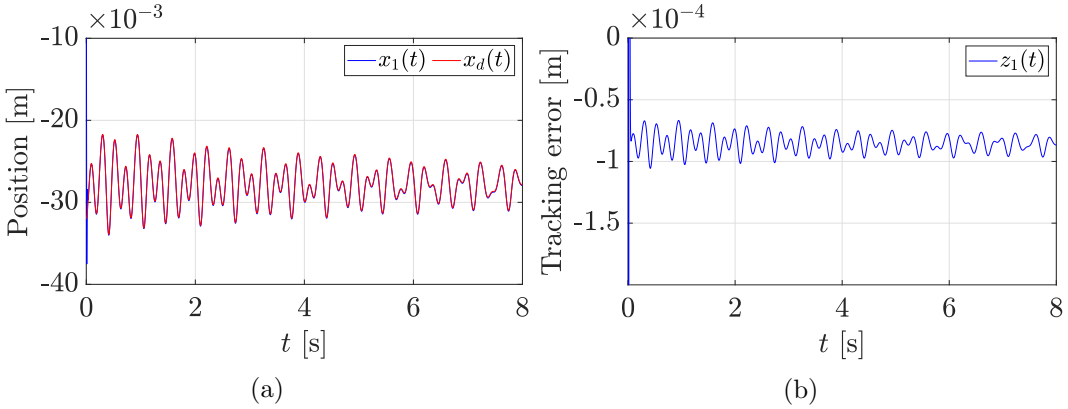

Figure 6.6: Right intrawell controller position tracking simulation result. (a) Position tracking. (b) Position tracking error z_1.

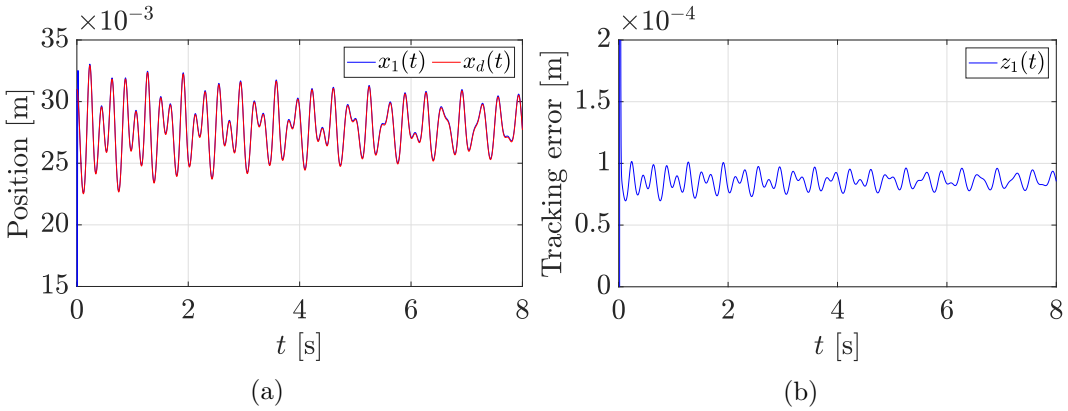

Figure 6.7: Left intrawell controller position tracking simulation result. (a) Position tracking. (b) Position tracking error z_1.

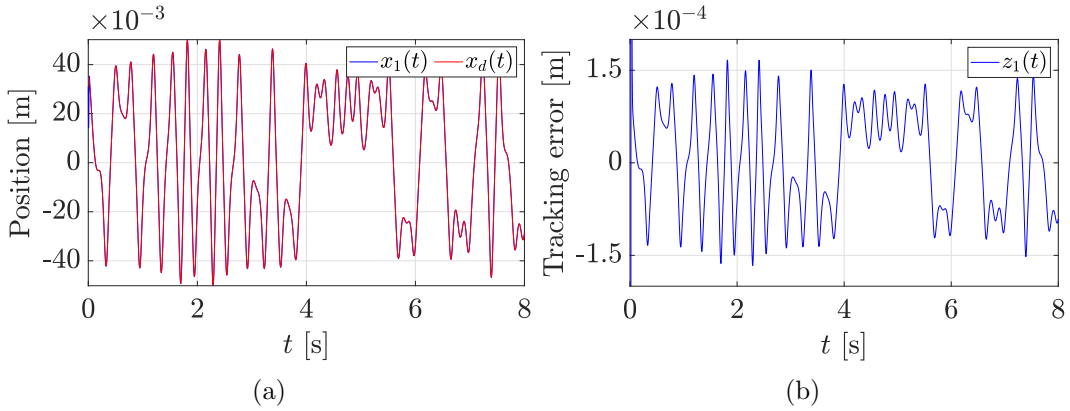

Figure 6.8: Chaos controller position tracking simulation result. (a) Position tracking. (b) Position tracking error z_1.

6.5.2 Experiments

Experiments were carried out to check the performance of the controller; for this, they were applied to each of the oscillator behaviors. The parameters used for the reference model and the state observer are the parameters estimated using the integral filters.

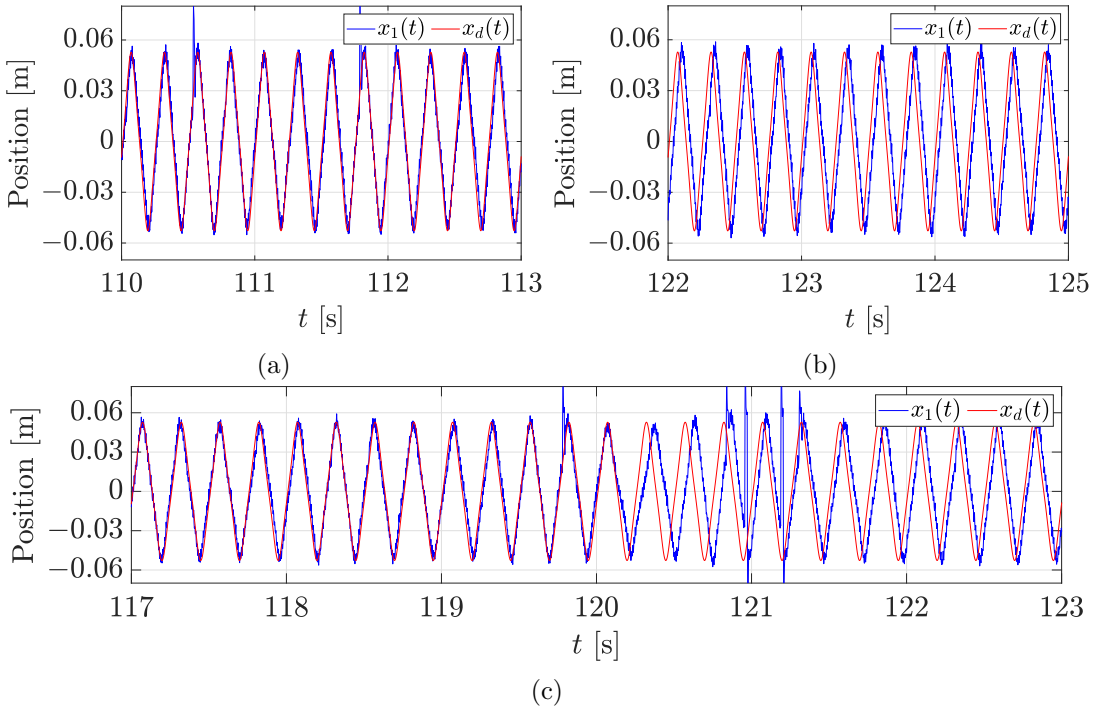

Figure 6.9: Interwell controller position tracking experimental results. (a) System behavior with control applied. (b) System behavior without control applied. (c) Controller application until $t = 120$ [s].

The observer gain is $\omega_o = 500$, and the controller gains used are $k_1 = 600$ and $k_2 = 250$. The

initial position of the reference model on the interwell behavior was $x_1(0) = 0.006$ [m], and the input force to both the reference model and the real system was $\ddot{v} = -1.7765\sin(18.8496t)$, so the reference signal has a 3 [Hz] frequency. In this way, the control signal will have this frequency and can be correctly integrated using the integrating filter (6.14). For the Interwell behavior control, the mean absolute and relative errors between the measured and desired positions were calculated. Table 5 presents both errors in the case of the uncontrolled system and the controlled system. The use of (6.15) was made to calculate the mean absolute and mean relative errors, respectively.

$$\epsilon = \frac{1}{N}\sum_{i=1}^{N}|x_1(i) - x_d(i)|, \quad \epsilon_r = \frac{1}{N}\sum_{i=1}^{N}\left[\frac{|x_1(i) - x_d(i)|}{x_d(i)} \times 100\right] \tag{6.15}$$

where N is the total number of samples.

Table 6.1: Controller performance.

System	**Controller position error**	
	Absolute mean error ϵ [m]	Relative mean error ϵ_r [%]
Uncontrolled	0.0218	94.5237
Controlled	0.0052	15.4779

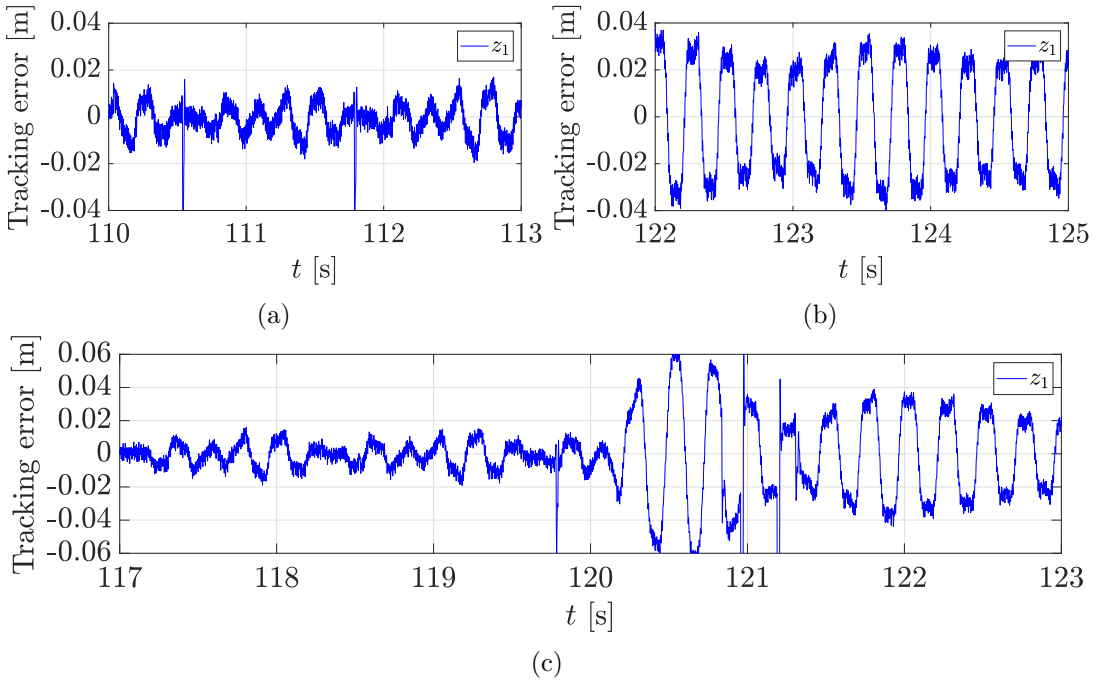

Figure 6.10: Interwell controller position tracking error z_1 experimental results. (a) System behavior with control applied. (b) System behavior without control applied. (c) Controller application until $t = 120$ [s].

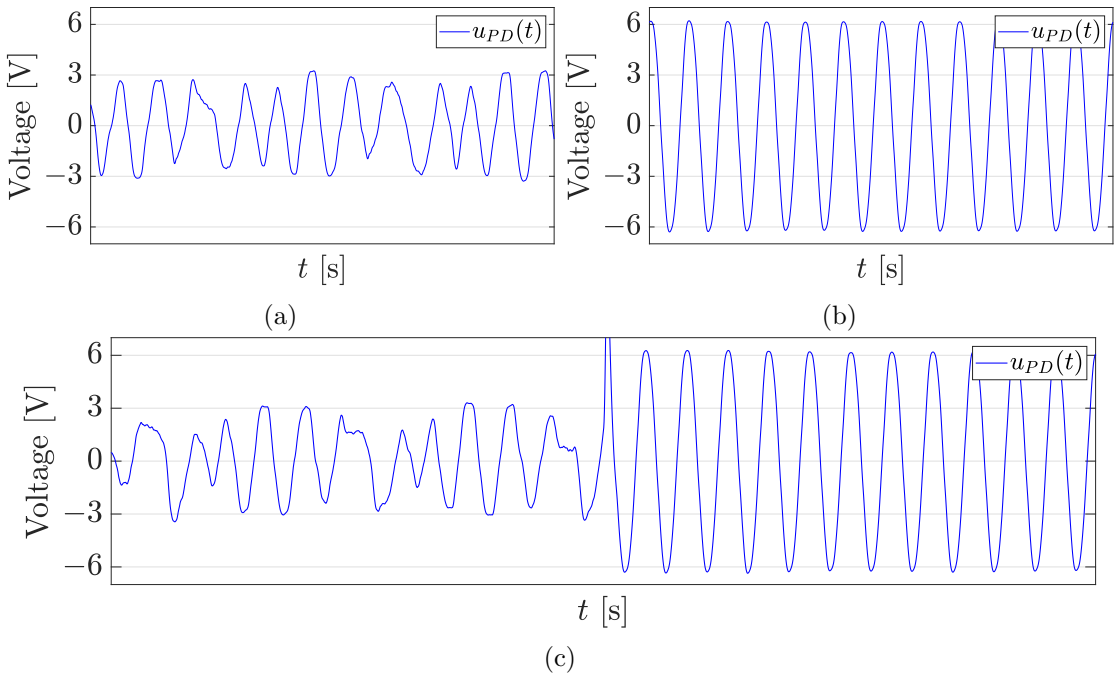

Figure 6.11: Interwell table input voltage experimental results. (a) System behavior with control applied. (b) System behavior without control applied. (c) Controller application until $t = 120$ [s].

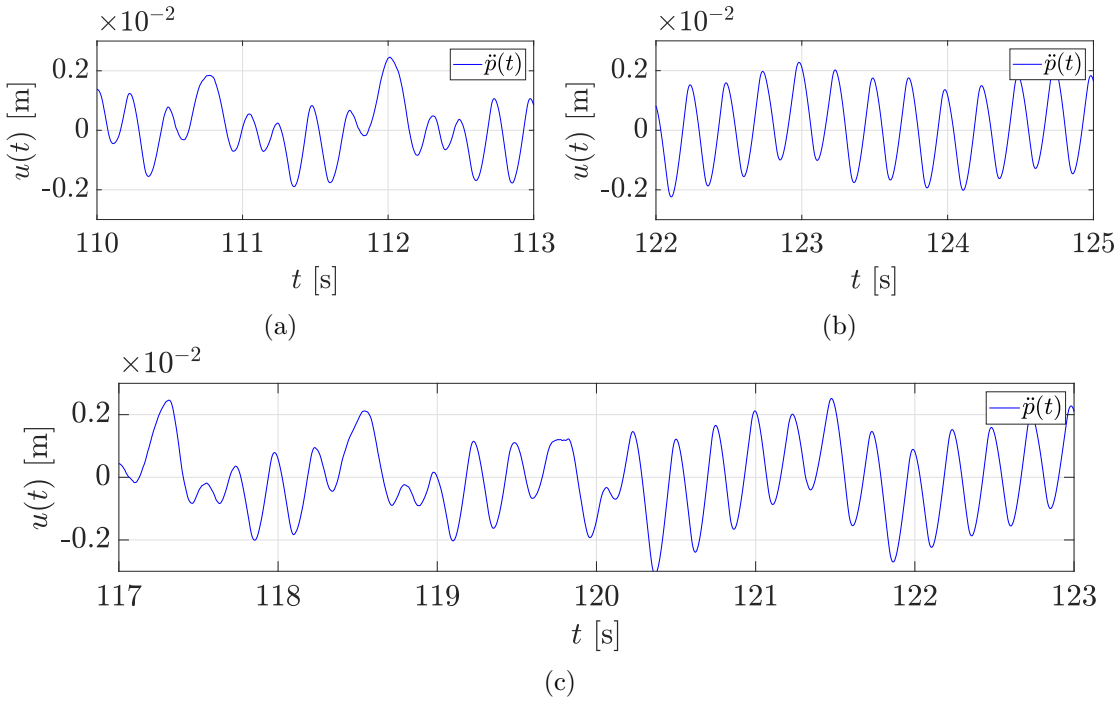

Figure 6.12: Interwell control signal [m] experimental results. (a) System behavior with control applied. (b) System behavior without control applied. (c) Controller application until $t = 120$ [s].

6.6 Conclusions

The experiments and simulations of the controller demonstrate its correct performance to track the reference trajectory x_d. However, the output of the controller is in terms of acceleration, and to control the shake table, it is necessary to use a reference position. It was necessary to apply a drift-free integrator, which allowed experimentation to be carried out. Due to the characteristics of the integrating filter used, it was not possible to obtain valid results for the intrawell and chaotic behaviors since the controller output for both cases presents low frequencies, and they are attenuated by the H_{nd} filter. Experimentally, it was possible to apply the controller appropriately for the Interwell behavior. The results show that x_1 properly tracks the reference x_d, and that both the voltage consumed by the table and the error between the reference position and the measured position are significantly reduced compared to when the designed controller is not applied to the system. Due to this problem, you can choose to use a method that allows you to control the table by taking advantage of the acceleration signal or, using the appropriate equipment, apply the controller to any dynamics of the system as demonstrated in the simulations.

CHAPTER 7

Conclusion

A Duffing oscillator prototype was created in order to make up for the elastic beam's non-ferromagnetic composition. Two neodymium magnets were used at the tip to make up for this. This made it possible to validate the system's behavior through experimentation. We were able to confirm through these experiments that the prototype's dynamics matched the theoretical description. In comparison to merely using the HG-C1400P sensor's typical output range, more accurate measurements could be obtained by better utilizing the resolution of the analog reading of the Q2-USB card because the amplification circuit functioned as intended.

Because the Quanser brand equipment has pre-designed and pre-defined tools for both digital coupling of the analog DAQ readings and vibration table calibration and control, the experimentation was completed quickly and effectively. Its use is nevertheless subject to certain software and hardware limitations, as with any experimental platform.

Both analytical techniques produced values that were comparable to the outcomes of the least squares method, and the systems identification methods produced reasonable estimated values. Three sets of estimated parameters make up the LMS results. These values are relatively similar to one another because the system's input and output signals were filtered using three different techniques.

The validation process was carried out in a hybrid way, that is, as a combination of experiments and simulations. The experimental excitation signal was injected into simulations with the parameter estimates. The validation was successful since the dynamics of the system were similar in each case compared to the experimental data; for each type of behavior, the same was obtained in both the experiment and the simulation. It was also verified that the identification convergence requirement was met.

The designed state observer allowed the state x_1 of the system to be accurately estimated, and, therefore, the rest of the estimates are considered to have small errors. Since the observer uses the estimated parameters in the identification, tests were carried out with each group of parameters to be able to choose the one that had the best results, resulting in the choice of the parameters obtained with the discrete filtering method. The observer used (NIESO) was compared with another similar observer (LIESO), and although the performance of both turned out to be very similar, the first showed to have less error in the estimation of x_1.

Once the state x_2 of the system could be estimated, it was possible to construct the Pincaré map of the chaotic behavior of the oscillator, which shows the characteristic form of the chaotic dynamics of the Duffing oscillator, demonstrating again that the constructed prototype is described

by the Duffing equation.

The design of the controller was carried out using the back-stepping technique and considered the use of the state observer for its design, so it was important to choose it appropriately. Experiments and simulations of the controller show that it works correctly and allows tracking of a reference trajectory with a small error. Here it is important to return to the physical limitations of the Shake Table I40 equipment, since the reference signal must be position in [m] and has a movement limit of $\pm$ 2 [cm]. However, because the controller output is given in terms of acceleration [m/s^2], it was necessary to use two drift-free integration filters so that the control signal could be sent to the actuator. However, by attenuating the low-frequency elements of u, it was not possible to obtain successful results in experimentation for the intrawell and chaotic behaviors. Despite this limitation, in the case of Interwell behavior, favorable results were obtained, managing to follow the reference x_d with a relatively small error and low voltage consumption by the vibration table, thus demonstrating the correct performance of the controller despite the limitations of the experimental equipment.

7.1 Future work

In this work, there are areas of opportunity in which work can be done to improve the project presented in this thesis. The amplification circuit can be modified to achieve a range of $\pm$ 12 [V], thus taking advantage of the full resolution of the DAQ's analog readout. Regarding identification, you can choose to use other methods or approaches to compare the results to find a method that can obtain a more accurate estimate, which will improve the performance of the proposed state observer. Regarding the state estimation method, an improvement process similar to that described for the identification method can be carried out. Regarding the controller, it can be redesigned to obtain an output in position, use another method of controlling the vibration table, or use another design technique for the controller in order to obtain successful results in experimentation with the complete dynamics of the system.

Bibliography

[1] E. N. Lorenz, "Deterministic nonperiodic flow," *Journal of atmospheric sciences*, vol. 20, no. 2, pp. 130–141, 1963.

[2] H. R. Biswas, M. M. Hasan, and S. K. Bala, "Chaos theory and its applications in our real life," *Barishal University Journal Part*, vol. 1, no. 5, pp. 123–140, 2018.

[3] R. L. Devaney and K. T. Alligood, *Chaos and Fractals: The Mathematics Behind the Computer Graphics: The Mathematics Behind the Computer Graphics*, vol. 1. American Mathematical Soc., 1989.

[4] Y. Jia, "Review of nonlinear vibration energy harvesting: Duffing, bistability, parametric, stochastic and others," *Journal of Intelligent Material Systems and Structures*, vol. 31, no. 7, pp. 921–944, 2020.

[5] A. Harb, "Energy harvesting: State-of-the-art," *Renewable Energy*, vol. 36, no. 10, pp. 2641–2654, 2011.

[6] C. A. Levano Huamaccto, "Caos en el oscilador de duffing mediante los mapas de poincaré," *Universidad Nacional Del Callao Repositorio Institucional Digital*, 2021.

[7] González Cruz, C. A., *Identificación de parámetros en sistemas mecánicos no lineales.* PhD thesis, Universidad Autónoma de Querétaro, http://ri-ng.uaq.mx/handle/123456789/769, July 2016.

[8] F. Moon and P. J. Holmes, "A magnetoelastic strange attractor," *Journal of Sound and Vibration*, vol. 65, no. 2, pp. 275–296, 1979.

[9] J.-H. He, "The simpler, the better: Analytical methods for nonlinear oscillators and fractional oscillators," *Journal of Low Frequency Noise, Vibration and Active Control*, vol. 38, no. 3-4, pp. 1252–1260, 2019.

[10] A. H. Salas Salas, J. E. Castillo Hernández, and L. J. Martínez Hernández, "The duffing oscillator equation and its applications in physics," *Mathematical Problems in Engineering*, vol. 2021, pp. 1–13, 2021.

[11] G. M. Moatimid, "Stability analysis of a parametric duffing oscillator," *Journal of Engineering Mechanics*, vol. 146, no. 5, p. 05020001, 2020.

[12] T. K. Dutta and P. K. Prajapati, "Some dynamical properties of the duffing equation," *International Journal of Engineering Research & Technologies*, vol. 5, no. 12, pp. 500–503, 2016.

[13] Z. Zhihong and Y. Shaopu, "Application of van der pol–duffing oscillator in weak signal detection," *Computers & Electrical Engineering*, vol. 41, pp. 1–8, 2015.

[14] F.-q. Wu, J. Ma, and G.-d. Ren, "Synchronization stability between initial-dependent oscillators with periodical and chaotic oscillation," *Journal of Zhejiang University-Science A*, no. 12, pp. 889–903, 2018.

[15] T. Karimov, E. G. Nepomuceno, O. Druzhina, A. Karimov, and D. Butusov, "Chaotic oscillators as inductive sensors: Theory and practice," *Sensors*, vol. 19, no. 19, p. 4314, 2019.

[16] Z. Feng, G. Chen, and S. Hsu, "A qualitative study of the damped duffing equation and applications," *DISCRETE AND CONTINUOUS DYNAMICAL SYSTEMS SERIES B*, vol. 6, no. 5, p. 1097, 2006.

[17] R. Zivieri, S. Vergura, and M. Carpentieri, "Analytical and numerical solution to the nonlinear cubic duffing equation: An application to electrical signal analysis of distribution lines," *Applied Mathematical Modelling*, vol. 40, no. 21-22, pp. 9152–9164, 2016.

[18] K. A. Kumar, S. Ali, and A. Arockiarajan, "Piezomagnetoelastic broadband energy harvester: nonlinear modeling and characterization," *The European Physical Journal Special Topics*, vol. 224, no. 14, pp. 2803–2822, 2015.

[19] S. R. Singiresu *et al.*, *Mechanical vibrations*. Addison Wesley Boston, MA, 1995.

[20] T. Kanamaru, "Duffing oscillator," *Scholarpedia*, vol. 3, no. 3, p. 6327, 2008. revision #91210.

[21] B. Mann, "Broadband energy harvesting from a bistable potential well," in *Advances in Energy Harvesting Methods*, pp. 91–115, Springer, 2013.

[22] A. Erturk and D. J. Inman, "Broadband piezoelectric power generation on high-energy orbits of the bistable duffing oscillator with electromechanical coupling," *Journal of Sound and Vibration*, vol. 330, no. 10, pp. 2339–2353, 2011.

[23] A. Ibrahim, S. Towfighian, and M. I. Younis, "Dynamics of transition regime in bistable vibration energy harvesters," *Journal of Vibration and Acoustics*, vol. 139, no. 5, 2017.

[24] Z. Wu, R. Harne, and K. Wang, "Excitation-induced stability in a bistable duffing oscillator: analysis and experiments," *Journal of Computational and Nonlinear Dynamics*, vol. 10, no. 1, 2015.

[25] P. Alevras, S. Theodossiades, and H. Rahnejat, "Broadband energy harvesting from parametric vibrations of a class of nonlinear mathieu systems," *Applied Physics Letters*, vol. 110, no. 23, p. 233901, 2017.

[26] D. Pan and F. Dai, "Design and analysis of a broadband vibratory energy harvester using bi-stable piezoelectric composite laminate," *Energy conversion and management*, vol. 169, pp. 149–160, 2018.

[27] A. Arrieta, P. Hagedorn, A. Erturk, and D. Inman, "A piezoelectric bistable plate for nonlinear broadband energy harvesting," *Applied Physics Letters*, vol. 97, no. 10, p. 104102, 2010.

[28] D. N. Betts, C. R. Bowen, H. A. Kim, N. Gathercole, C. T. Clarke, and D. J. Inman, "Nonlinear dynamics of a bistable piezoelectric-composite energy harvester for broadband application," *The European Physical Journal Special Topics*, vol. 222, no. 7, pp. 1553–1562, 2013.

[29] A. Arrieta, T. Delpero, A. Bergamini, and P. Ermanni, "Broadband vibration energy harvesting based on cantilevered piezoelectric bi-stable composites," *Applied Physics Letters*, vol. 102, no. 17, p. 173904, 2013.

[30] D. N. Betts, R. A. Guyer, P.-Y. Le Bas, C. R. Bowen, D. Inman, and H. A. Kim, "Modelling the dynamic response of bistable composite plates for piezoelectric energy harvesting," in *55th AIAA/ASMe/ASCE/AHS/SC Structures, Structural Dynamics, and Materials Conference*, p. 0154, 2014.

[31] H. Li, F. Dai, and S. Du, "Broadband energy harvesting by exploiting nonlinear oscillations around the second vibration mode of a rectangular piezoelectric bistable laminate," *Smart materials and structures*, vol. 24, no. 4, p. 045024, 2015.

[32] P. Harris, C. R. Bowen, and H. A. Kim, "Manufacture and characterisation of piezoelectric broadband energy harvesters based on asymmetric bistable laminates," *Journal of Multifunctional Composites*, vol. 2, no. 3, pp. 113–123, 2014.

[33] D. Pan, B. Ma, and F. Dai, "Experimental investigation of broadband energy harvesting of a bi-stable composite piezoelectric plate," *Smart Materials and Structures*, vol. 26, no. 3, p. 035045, 2017.

[34] L. Wang, J. Ding, Z. Jiang, G. Luo, L. Zhao, D. Lu, X. Yang, and M. Ryutaro, "A packaged piezoelectric vibration energy harvester with high power and broadband characteristics," *Sensors and Actuators A: Physical*, vol. 295, pp. 629–636, 2019.

[35] R. L. Harne and K.-W. Wang, *Harnessing bistable structural dynamics: for vibration control, energy harvesting and sensing*. John Wiley & Sons, 2017.

[36] S. P. Pellegrini, N. Tolou, M. Schenk, and J. L. Herder, "Bistable vibration energy harvesters: a review," *Journal of Intelligent Material Systems and Structures*, vol. 24, no. 11, pp. 1303–1312, 2013.

[37] B. A. Owens, S. C. Stanton, and B. P. Mann, "Analysis of the bistable piezoelectric inertial generator by the harmonic balance method," in *ASME International Mechanical Engineering Congress and Exposition*, vol. 45202, pp. 1159–1166, American Society of Mechanical Engineers, 2012.

[38] V. Agarwal, X. Zheng, and B. Balachandran, "Influence of noise on frequency responses of softening duffing oscillators," *Physics Letters A*, vol. 382, no. 46, pp. 3355–3364, 2018.

[39] J. Y. Yoon, M. Noh, and D. L. Trumper, "Duffing oscillation and jump resonance: Spectral hysteresis and input-dependent resonance shift," *Precision Engineering*, vol. 70, pp. 63–69, 2021.

[40] G. A. Correa, J. V. Cabreraa, and C. M. Péreza, "Estudio de la entropía de shannon de la dinámica no lineal de dos osciladores de duffing no disipativos acoplados," *Encuentro participación de la mujer en la ciencia*, 2015.

[41] S. Moriello, "Sistemas complejos, caos y vida artificial," *Red científica*, pp. 1579–0233, 2003.

[42] Quanser Inc., *Shake Table I-40 User Manual*, 2012.

[43] Panasonic Electric Works, *CMOS Type Micro Laser Distance Sensor Amplifier Built-in HG-C SERIES*, 2016.

[44] Analog Devices, *Low Cost Low Power Instrumentation Amplifier AD620*, 2011.

[45] J. Schoukens and L. Ljung, "Nonlinear system identification: A user-oriented road map," *IEEE Control Systems Magazine*, vol. 39, no. 6, pp. 28–99, 2019.

[46] F. Gao, X.-j. Lee, F.-x. Fei, H.-q. Tong, Y.-b. Qi, Y.-f. Deng, I. Balasingham, and H.-l. Zhao, "Parameter identification for van der pol–duffing oscillator by a novel artificial bee colony algorithm with differential evolution operators," *Applied Mathematics and Computation*, vol. 222, pp. 132–144, 2013.

[47] L. Jun-An, T. Chao-Hai, L. Jin-Hu, and L. Min, "Parameter identification and tracking of a unified system," *Chinese Physics Letters*, vol. 19, no. 5, p. 632, 2002.

[48] A. H. Nayfeh and D. T. Mook, *Nonlinear oscillations*. John Wiley & Sons, 2008.

[49] T. Caughey, "Response of van der pol's oscillator to random excitation," *Journal of Applied Mechanics 26*, 1959.

[50] T. Caughey, "Random excitation of a system with bilinear hysteresis," *Journal of Applied Mechanics 27*, 1960.

[51] T. K. Caughey, "Equivalent linearization techniques," *The Journal of the Acoustical Society of America*, vol. 35, no. 11, pp. 1706–1711, 1963.

[52] S. Masri and T. Caughey, "A nonparametric identification technique for nonlinear dynamic problems," *Journal of Applied Mechanics 46*, 1979.

[53] H. Lo and J. Hammond, "Identification of a class of nonlinear systems," *preprint, Institute of Sound and Vibration Research, Southampton*, 1988.

[54] G. E. Box, G. M. Jenkins, G. C. Reinsel, and G. M. Ljung, *Time series analysis: forecasting and control*. John Wiley & Sons, 2015.

[55] I. Leontaritis and S. A. Billings, "Input-output parametric models for non-linear systems part i: deterministic non-linear systems," *International journal of control*, vol. 41, no. 2, pp. 303–328, 1985.

[56] M. Korenberg, S. A. Billings, Y. Liu, and P. McIlroy, "Orthogonal parameter estimation algorithm for non-linear stochastic systems," *International Journal of Control*, vol. 48, no. 1, pp. 193–210, 1988.

[57] F. Mezghani, A. F. del Rincón, M. A. B. Souf, P. G. Fernandez, F. Chaari, F. V. Rueda, and M. Haddar, "Alternating frequency time domains identification technique: Parameters determination for nonlinear system from measured transmissibility data," *European Journal of Mechanics-A/Solids*, vol. 80, p. 103886, 2020.

[58] L. Li, Y. Yang, H. Peng, and X. Wang, "Parameters identification of chaotic systems via chaotic ant swarm," *Chaos, Solitons & Fractals*, vol. 28, no. 5, pp. 1204–1211, 2006.

[59] H. Modares, A. Alfi, and M.-M. Fateh, "Parameter identification of chaotic dynamic systems through an improved particle swarm optimization," *Expert Systems with Applications*, vol. 37, no. 5, pp. 3714–3720, 2010.

[60] G. Quaranta, G. Monti, and G. C. Marano, "Parameters identification of van der pol–duffing oscillators via particle swarm optimization and differential evolution," *Mechanical Systems and Signal Processing*, vol. 24, no. 7, pp. 2076–2095, 2010.

[61] G. Li, L. Zeng, L. Zhang, and Q. J. Wu, "State identification of duffing oscillator based on extreme learning machine," *IEEE Signal Processing Letters*, vol. 25, no. 1, pp. 25–29, 2017.

[62] M. U. Rani, "Calculation of moment of inertia for various geometrical cross section using c programming," *International Research Journal of Engineering and Technology (IRJET)*, vol. 8, no. 11, 2021.

[63] A. Concha, "Estudio comparativo de métodos de identificación en lazo cerrado para un servomecanismo," Master's thesis, Centro de investigación y de estudios avanzados del instituto politécnico nacional, 2009.

[64] S. Paulo, *Diniz, Adaptive Filtering: Algorithms and Practical Implementation, Springer*. Springer Nature Switzerland AG, 2010.

[65] R. Isermann and M. Münchhof, *Identification of dynamic systems: an introduction with applications*, vol. 85. Springer, 2011.

[66] R. Garrido and A. Concha, "Estimation of the parameters of structures using acceleration measurements," *IFAC Proceedings Volumes*, vol. 45, no. 16, pp. 1791–1796, 2012.

[67] S. Sagara and Z.-Y. Zhao, "Numerical integration approach to on-line identification of continuous-time systems," *Automatica*, vol. 26, no. 1, pp. 63–74, 1990.

[68] P. Bernard, V. Andrieu, and D. Astolfi, "Observer design for continuous-time dynamical systems," *Annual Reviews in Control*, vol. 53, pp. 224–248, 2022.

[69] J. H. Ahrens and H. K. Khalil, "High-gain observers in the presence of measurement noise: A switched-gain approach," *Automatica*, vol. 45, no. 4, pp. 936–943, 2009.

[70] S. Thenozhi, U. M. Cárdenas, and A. C. Sánchez, "Observer design for a duffing-holmes system with uncertainties," in *2022 19th International Conference on Electrical Engineering, Computing Science and Automatic Control (CCE)*, pp. 1–4, IEEE, 2022.

[71] S. Li, J. Yang, W.-H. Chen, and X. Chen, "Generalized extended state observer based control for systems with mismatched uncertainties," *IEEE Transactions on Industrial Electronics*, vol. 59, no. 12, pp. 4792–4802, 2011.

[72] S. Xiong, W. Wang, X. Liu, Z. Chen, and S. Wang, "A novel extended state observer," *ISA transactions*, vol. 58, pp. 309–317, 2015.

[73] M. Ran, J. Li, and L. Xie, "A new extended state observer for uncertain nonlinear systems," *Automatica*, vol. 131, p. 109772, 2021.

[74] B.-Z. Guo and Z.-l. Zhao, "On the convergence of an extended state observer for nonlinear systems with uncertainty," *Systems & Control Letters*, vol. 60, no. 6, pp. 420–430, 2011.

[75] S. Thenozhi, A. C. Sánchez, and J. Rodríguez-Reséndiz, "A contraction theory-based tracking control design with friction identification and compensation," *IEEE Transactions on Industrial Electronics*, vol. 69, no. 6, pp. 6111–6120, 2021.

[76] M. Ran, Q. Wang, and C. Dong, "Active disturbance rejection control for uncertain nonaffine-in-control nonlinear systems," *IEEE Transactions on Automatic Control*, vol. 62, no. 11, pp. 5830–5836, 2016.

[77] C. H. González Obregón, *Análisis de complejidad de sistema respiratorio para la ayuda al diagnóstico de patologías*. Universitat Politècnica de Catalunya, 2002.

[78] Ö. Ahmet and A. Erhan, "Tools for detecting chaos," *Sakarya University Journal of Science*, vol. 9, no. 1, pp. 60–66, 2005.

[79] T. Kapitaniak, K.-E. Thylwe, I. Cohen, and J. Wojewoda, "Chaos-hyperchaos transition," *Chaos, Solitons & Fractals*, vol. 5, no. 10, pp. 2003–2011, 1995.

[80] M. Sifakis and S. Elliott, "Strategies for the control of chaos in a duffing–holmes oscillator," *Mechanical Systems and Signal Processing*, vol. 14, no. 6, pp. 987–1002, 2000.

[81] M. T. Cuairan, J. Gieseler, N. Meyer, and R. Quidant, "Precision calibration of the duffing oscillator with phase control," *Physical Review Letters*, vol. 128, no. 21, p. 213601, 2022.

[82] J. Huang and J. Ji, "Vibration control of coupled duffing oscillators in flexible single-link manipulators," *Journal of Vibration and control*, vol. 27, no. 17-18, pp. 2058–2068, 2021.

[83] A. Agrawal, J. Yang, and J. Wu, "Non-linear control strategies for duffing systems," *International Journal of Non-Linear Mechanics*, vol. 33, no. 5, pp. 829–841, 1998.

[84] C. Wu, Y. Lei, and T. Fang, "Stochastic chaos in a duffing oscillator and its control," *Chaos, Solitons & Fractals*, vol. 27, no. 2, pp. 459–469, 2006.

[85] J. Yao, Z. Jiao, and D. Ma, "Adaptive robust control of dc motors with extended state observer," *IEEE Transactions on Industrial Electronics*, vol. 61, no. 7, pp. 3630–3637, 2014.

[86] A. M. Harb, A. A. Zaher, A. A. Al-Qaisia, and M. A. Zohdy, "Recursive backstepping control of chaotic duffing oscillators," *Chaos, Solitons & Fractals*, vol. 34, no. 2, pp. 639–645, 2007.

[87] B. Bahtiyar, "Real-time analysis of adaptive fuzzy predictive controller for chaotification under varying payload and noise conditions," *Neural Computing and Applications*, vol. 33, no. 20, pp. 13449–13465, 2021.

[88] V. Piccirillo, "Suppression of chaos in nonlinear oscillators using a linear vibration absorber," *Meccanica*, vol. 56, no. 2, pp. 255–273, 2021.

[89] S. Vaidyanathan and A. T. Azar, "An introduction to backstepping control," in *Backstepping Control of Nonlinear Dynamical Systems*, pp. 1–32, Elsevier, 2021.

[90] F. Ikhouane and M. Krstic, "Robustness of the tuning functions adaptive backstepping design for linear systems," *IEEE transactions on Automatic Control*, vol. 43, no. 3, pp. 431–437, 1998.

[91] G. Xu, Z. Wang, Y. Bao, G. Yang, and B. Wu, "Shaking table substructure testing based on three-variable control method with velocity positive feedback," *Applied Sciences*, vol. 10, no. 16, p. 5414, 2020.

[92] A. de Cheveigné and I. Nelken, "Filters: when, why, and how (not) to use them," *Neuron*, vol. 102, no. 2, pp. 280–293, 2019.

[93] J. Li, Z. Liu, Q. Geng, S. Yang, H. Chen, and M. Chen, "Method for suppressing the frequency drift of integrated microwave photonic filters," *Optics Express*, vol. 27, no. 23, pp. 33575–33585, 2019.

APPENDIX A

Prototype reference drawings

In this annex, you can find the schematic drawings of the parts designed for the construction of the experimental prototype developed for this thesis. All measurements are in millimeters [mm]. The manufacturing material is specified in each piece; to identify the parts, you can use the figures in Chapter 3 as a reference. The schematics are to scale; this is specified in the description of each drawing.

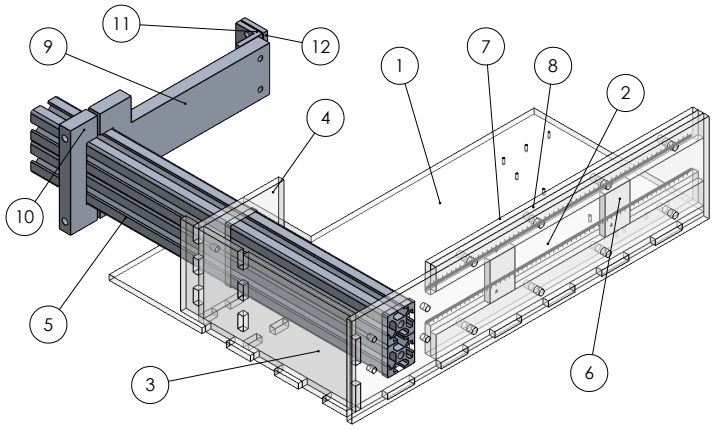

Figure A.1: CAD assembly of the designed parts of the experimental prototype.

The elements shown in Figure A.1 are listed below:

1. Main base: this part connects to the shake table plate.
2. Bottom base: this part is the base for rails and magnets bases.
3. Back wall: This is an structural part, it is used to hold the auxiliary support base for aluminium tubes.
4. Auxiliary support base: this base helps to hold the aluminium tubes.
5. Aluminium tubes: square shape with 30×30 [mm] dimensions.

6. Magnet bases: This bases moves all over the rail created by the structured formed by the Base rails and Milimetric rails.

7. Milimetric rail: This is the upper rail that has millimeter marks to correctly locate the magnets base in a desired position.

8. Base rail: this rail helps to create an space where the magnets base can move.

9. Beam holder base: This aluminium structure is mobile, it travels on the aluminium tubes.

10. Beam holder base auxiliary: helps to hold the Beam holder base in the desired place using screws.

11. Beam holder: This part and its auxiliary holds the experimental beam using screws.

12. Beam holder auxiliary.

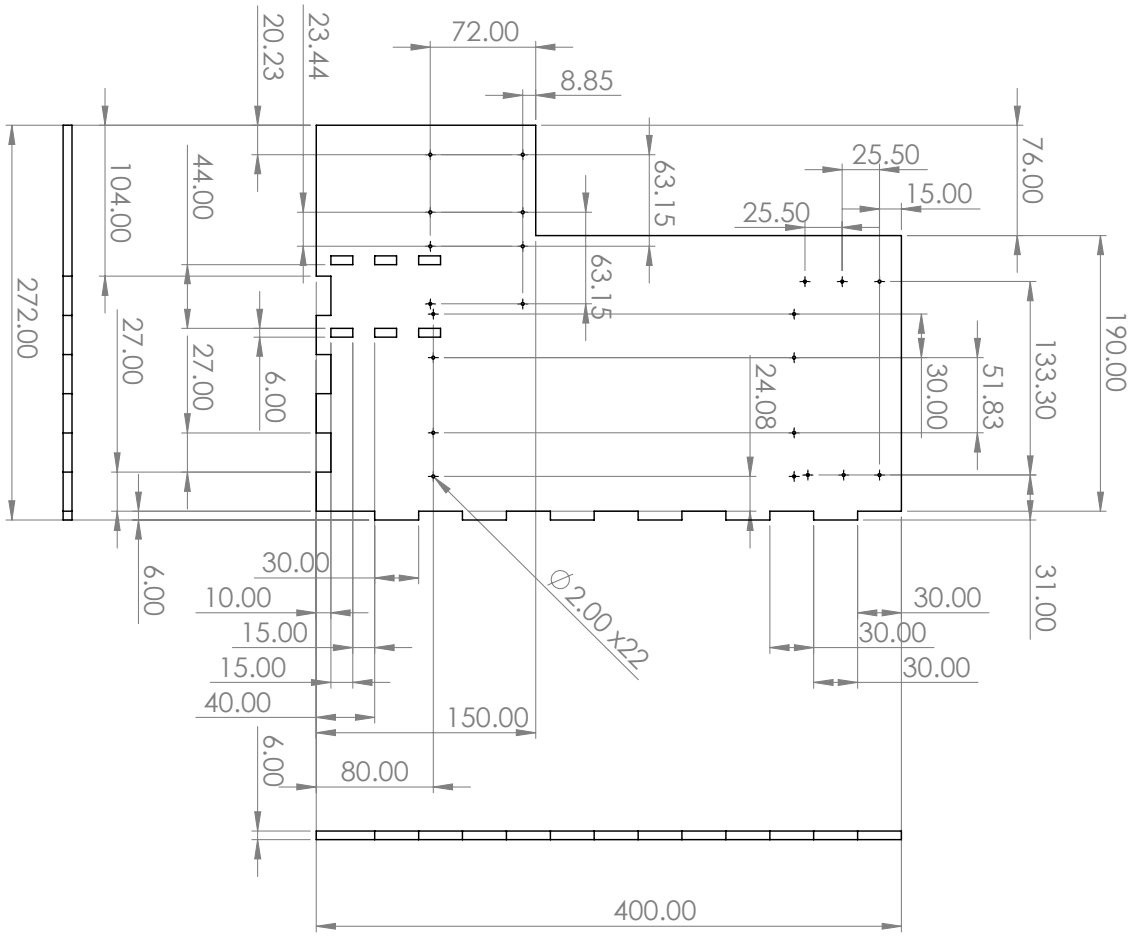

Figure A.2: 1. Main base: 1:4 scale, transparent acrylic.

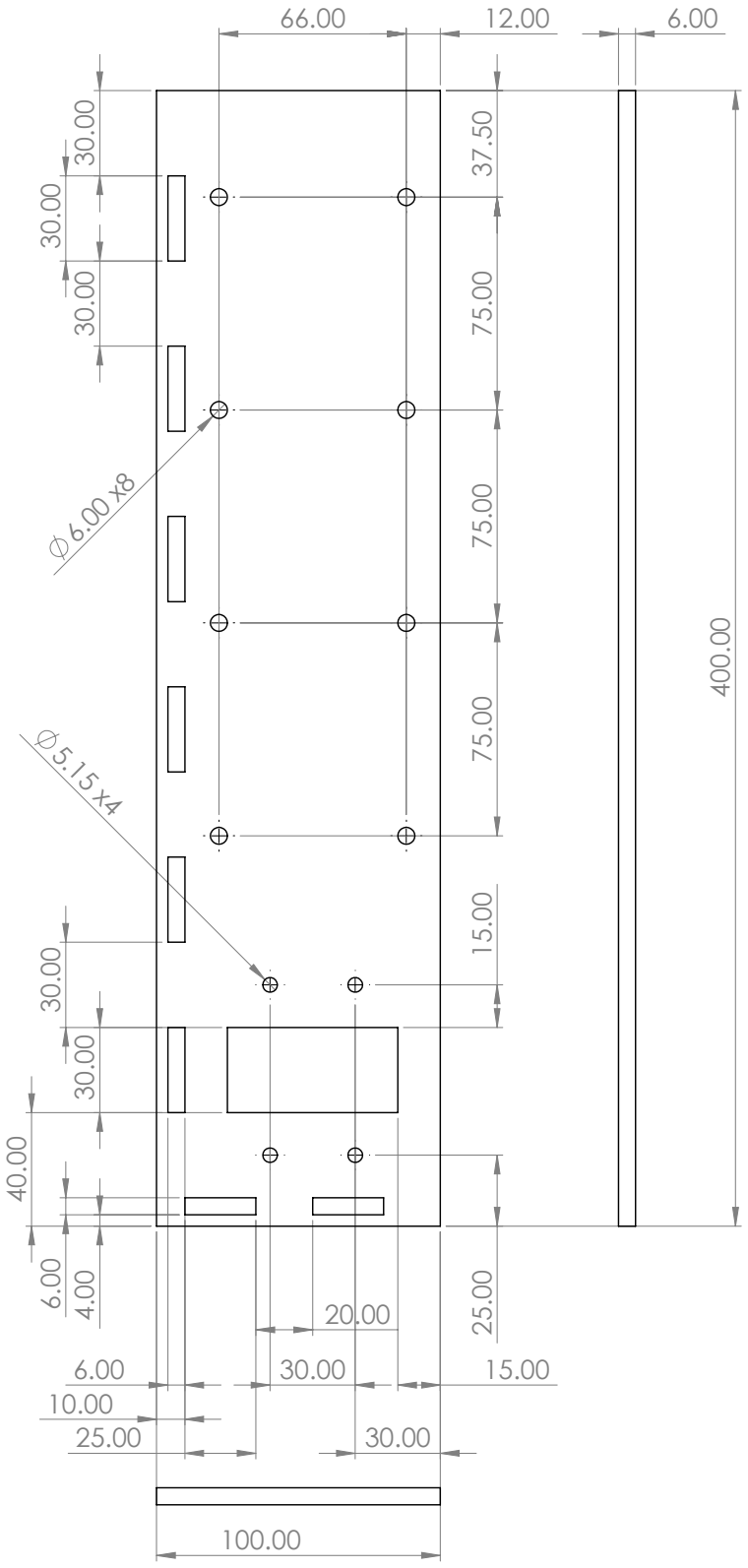

Figure A.3: 2. Bottom base: 1:2 scale, transparent acrylic.

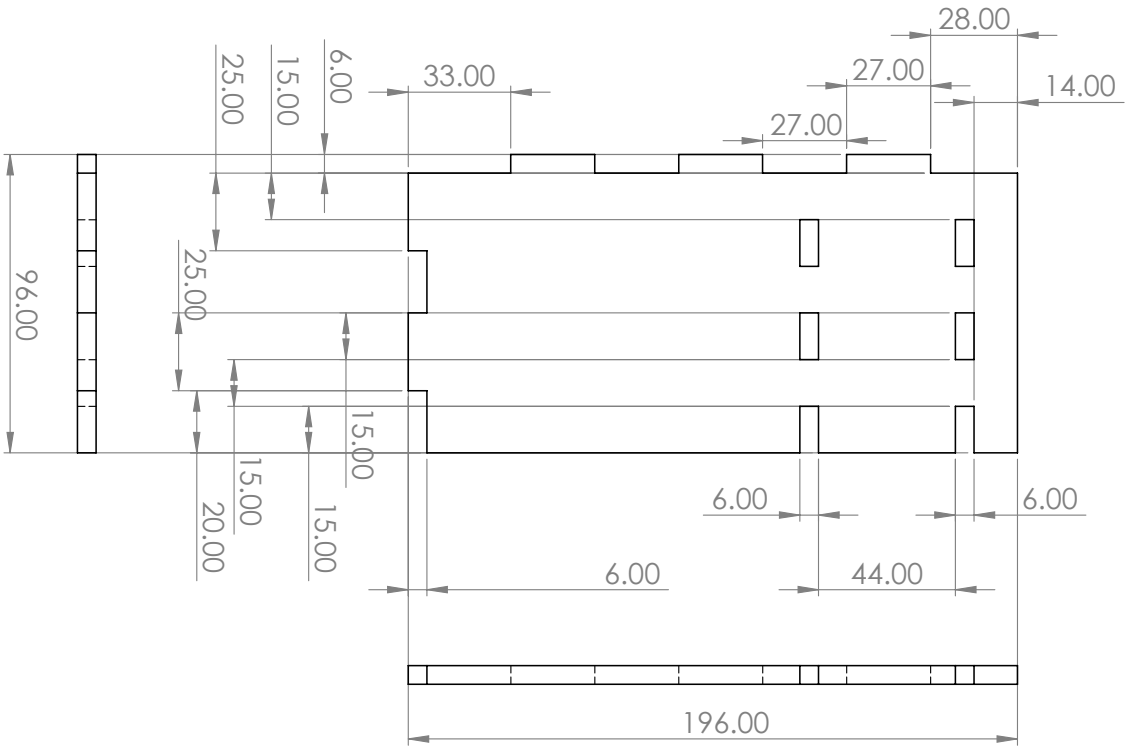

Figure A.4: 3. Back wall: 1:2 scale, transparent acrylic.

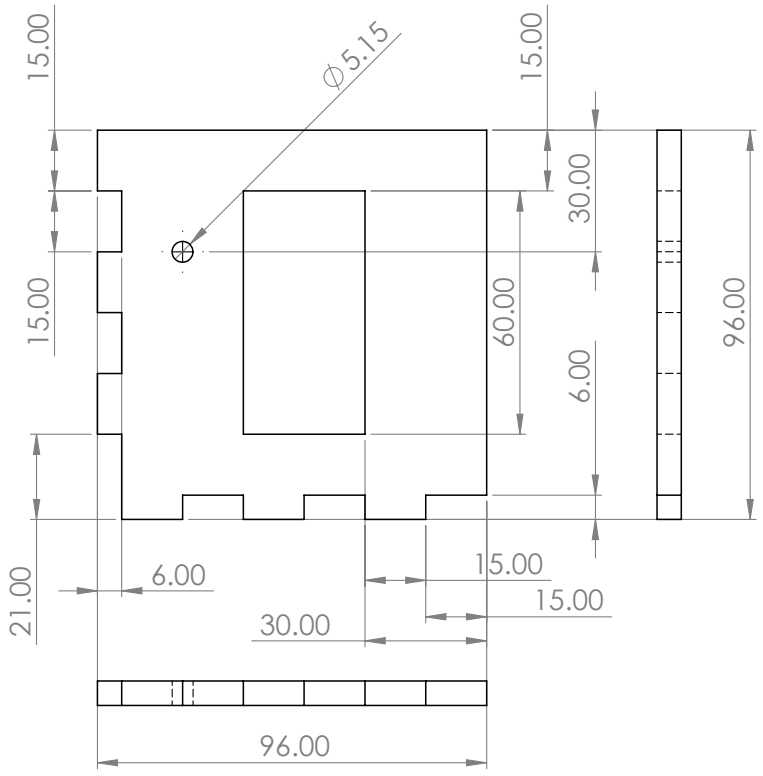

Figure A.5: 4. Auxiliary support base: 1:1.5 scale, transparent acrylic.

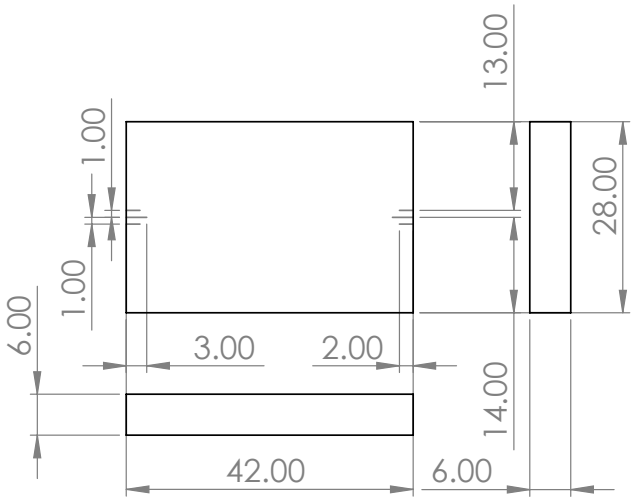

Figure A.6: 6. Magnet base: 1:1 scale, transparent acrylic.

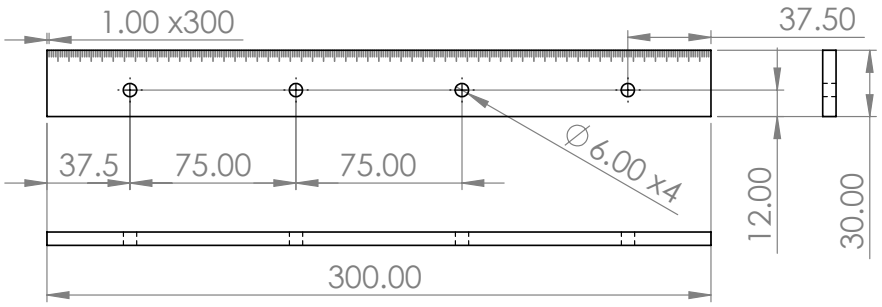

Figure A.7: 7-8. Milimetric and base rail 1:3 scale, transparent acrylic.

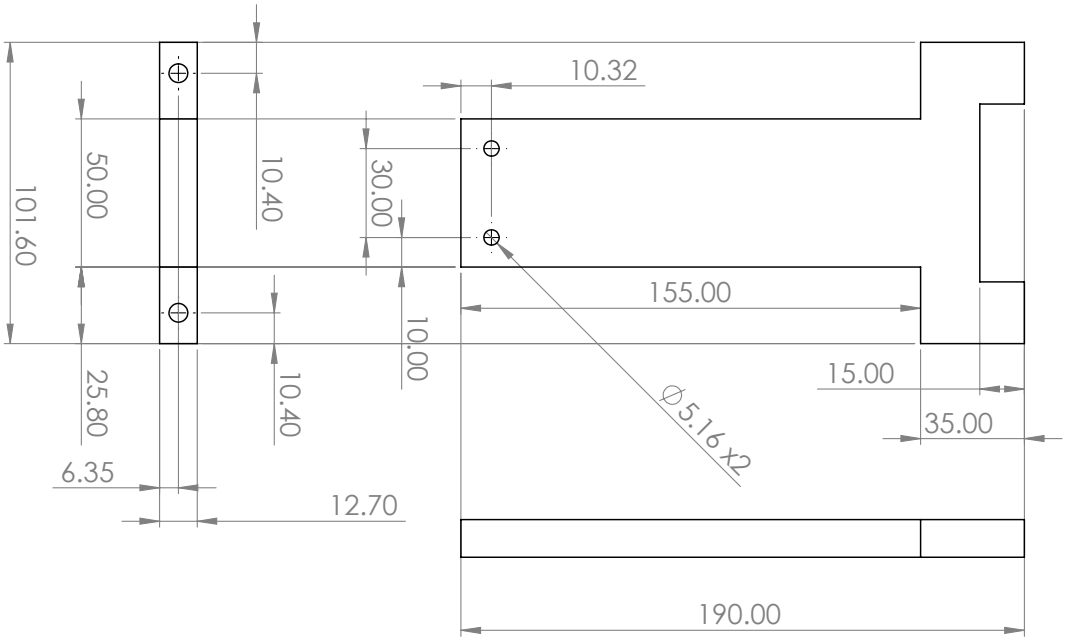

Figure A.8: 9. Beam holder base: 1:2 scale, aluminium.

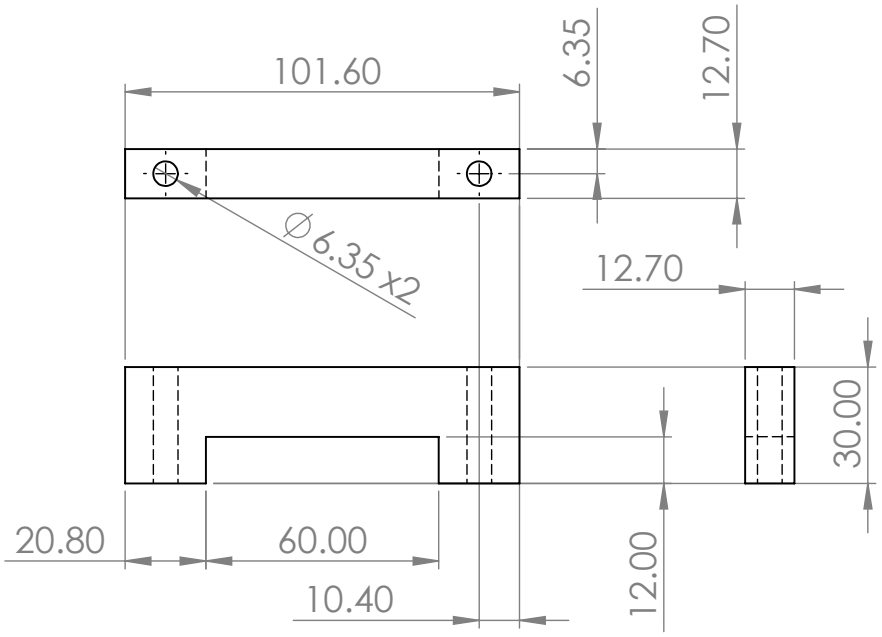

Figure A.9: 10. Beam holder base auxiliary: 1:2 scale, aluminium.

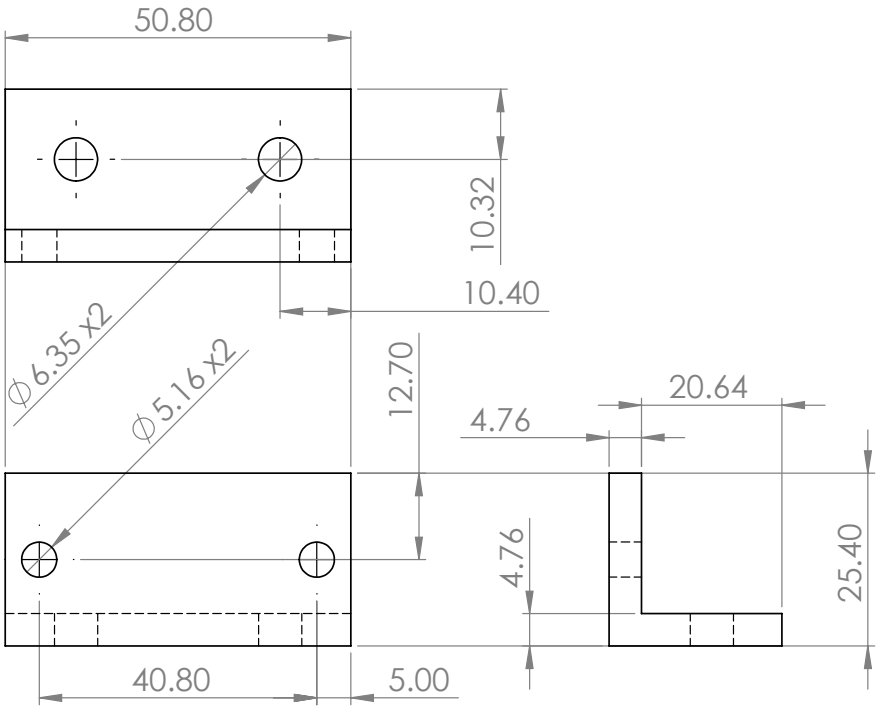

Figure A.10: 11. Beam holder: 1:1 scale, aluminium.

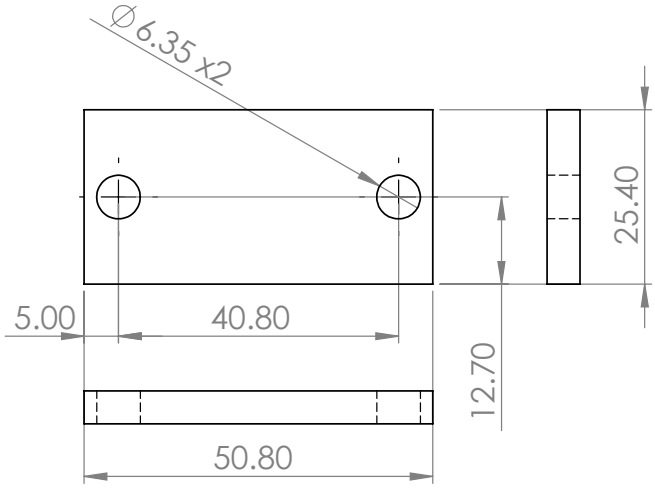

Figure A.11: 12. Beam holder auxiliary: 1:1 scale, aluminium.